MACROPHAGES, OSCILLATORS AND FISH: USING DYNAMICAL SYSTEMS TO EXAMINE BIOLOGICAL PROBLEMS

A Dissertation

Presented to the Faculty of the Graduate School

of Cornell University

in Partial Fulfillment of the Requirements for the Degree of

Doctor of Philosophy

by

Lauren Maressa Childs

May 2010

MACROPHAGES, OSCILLATORS AND FISH:

USING DYNAMICAL SYSTEMS TO EXAMINE BIOLOGICAL PROBLEMS

Lauren Maressa Childs, Ph.D.

Cornell University 2010

Dynamical systems techniques are used to examines three biological questions including macrophage activation, coupled oscillators and decision making in fish schools.

Macrophages are fundamental cells of the innate immune system. Their activation is essential for such distinct immune functions as inflammation (pathogen-killing) and tissue repair (wound-healing). An open question has been the functional stability of an individual macrophage cell: whether it can change its functional profile between different immune responses such as between the repair pathway and the inflammatory pathway. We studied this question theoretically by constructing a rate equation model for the key substrate, enzymes and products of the pathways; we then tested the model experimentally. Both our model and experiments show that individual macrophages can switch from the repair pathway to the inflammation pathway but that the reverse switch does not occur.

We analyzed the periodically forced Kuramoto model. This system consists of an infinite population of phase oscillators with random intrinsic frequencies, global sinusoidal coupling, and external sinusoidal forcing. It represents an idealization of many phenomena in physics, chemistry and biology in which mutual synchronization competes with forced synchronization. In other words, the oscillators in the population try to synchronize with one another while also

trying to lock onto an external drive. Previous work on the forced Kuramoto model uncovered two main types of attractors, called forced entrainment and mutual entrainment, but the details of the bifurcations between them were unclear. Here we present a complete bifurcation analysis of the model for a special case in which the infinite-dimensional dynamics collapse to a two-dimensional system. Exact results are obtained for the locations of Hopf, saddle-node, and Takens-Bogdanov bifurcations. The resulting stability diagram bears a striking resemblance to that for the weakly nonlinear forced van der Pol oscillator.

Many types of fish travel in schools where they cooperate on activities such as foraging for food and avoiding predators. In the past, it was believed that such group actions were dictated by a small number of informed leaders but recent evidence has shown that strictly local interactions can be responsible for cohesive group dynamics. Using an ODE model, we investigated the ability of a group of fish to make an accurate decision when portions of the group have conflicting information. Beyond the disparity of information, it is not known which individuals have which information. We modeled fish schools where a portion of the school believed food was in one location and another equal-sized portion of the school believed the food was in another location. We found that the ability to make an accurate decision (locate food) required that some individuals "forget" or ignore their information. Without the loss of information by some individuals there was no ability to make a consensus decision.

BIOGRAPHICAL SKETCH

Lauren Maressa Childs was born in Evanston, Illinois to parents Nancy Maressa and Michael Edward and an older brother, Lete Michael. She was soon whisked back to the East Cost to be raised in Medford, New Jersey. From an early age, Lauren was interested in numbers and mathematics and it was foretold by her kindergarten teachers that she would one day pursue mathematics. She attended elementary and middle school in Medford, New Jersey culminating at Lenape High School where she graduated as valedictorian in June 2000. Following high school and the path taken by her parents Lauren attended Duke University in Durham, North Carolina. As a junior she received the Barry M. Goldwater Scholarship, and she graduated in May 2004 as Magna Cum Laude with a Bachelors of Science in Mathematics,a Bachelors of Arts in Chemistry, and a Minor in Comparative Area Studies. In August 2004, Lauren started the Ph.D. program at the Center for Applied Mathematics at Cornell University in Ithaca, New York working with Dr. Steven Strogatz. She received her Masters in Applied Mathematics in April 2007. Following her Masters, Lauren took a semester leave of absence to volunteer in Moshi, Tanzania, East Africa on health care and education issues. It was there she realized her passion for using mathematics on real world problems. Upon return to graduate work, she turned towards more applied aspects of mathematics. She will receive her Ph.D. in Applied Mathematics with Minors in Mathematics and Immunology in May 2010 and will start a postdoctoral fellowship at Georgia Institute of Technology with Dr. Joshua Weitz in September 2010. Beyond mathematics Lauren is interested in sports, particularly ultimate, running and basketball, as well as music, travel and languages.

for my brother Lete

ACKNOWLEDGEMENTS

First, I would like to thank my advisor Dr. Steven H. Strogatz, for his continual support and encouragement throughout my graduate career. I especially appreciate the freedom he gave me to pursue my non-traditional path into academics.

I also thank my committee members: Dr. Richard H. Rand, for his guidance and direction, and Dr. Matthias Hesse, for his enthusiasm for interdisciplinary work and for allowing a mathematician into his laboratory.

I am grateful to Dr. Thomas B. Kepler, Dr. Michael Reed, Dr. Mary Lou Zeeman and Dr. Chad Topaz for giving me confidence and guidance throughout my academic career as well as Dolores Pendell for ensuring a smooth path through graduate school. Finally, I thank all those I have worked for and with, especially Dr. Iain Couzin and Dr. James Collins, for their collaboration and friendship.

I thank my parents, Nancy and Michael, for their love and support, and my brother, Lete, for his unquestioning belief in my ability to succeed. As well, I thank my grandparents, especially Frank and Eleanor, who have always taught me that anything is possible. Further, my entire family has always been understanding of my preoccupations. I also thank good friends Jeffrey and Alice Morris and Michele and Larry Radcliffe for their encouragement and support.

I also thank the many friends who have been there for me: Yasho, for being there for me whenever I needed her, whether for coffee or sanity; Mimi, who knows me better than I know myself; and Ben, who has taught me to value and appreciate the arts as well as the sciences; Marie and Robin, who can always make me smile and remind me that eccentricity is appropriate; Megan, for all her help and understanding; Angie, for always commiserating on the trials of graduate school; all my house-mates and officemates for making my time in

Ithaca so enjoyable, particularly Chris, Stephen, Stefan, Andrew, Anthony, Peter, Sam, David and Zory, for always including me in all your fun; Carley and Hagar for getting me to realize there is much more to life than school and the members of the Cornell Roses and Brute Squad for always providing me with an often needed distraction from my research. Finally, I thank Eyvindur Ari for his complete understanding of me and his ability to know what is best for both of us.

As with any acknowledgments there are always more to thank and I apologize for omitting anyone here.

I gratefully acknowledge the support of my work by an NSF-IGERT Fellowship and an NSF Graduate Fellowship.

TABLE OF CONTENTS

LIST OF TABLES

LIST OF FIGURES

CHAPTER 1

INTRODUCTION

Macrophages, oscillators and fish, the main title of this work, references the three projects I have worked on throughout my graduate career. These are macrophage cell functional pathway activation, the forced Kuramoto model of coupled oscillators, and consensus decision making among fish. Each of these projects has allowed me to work with and learn from different scientists, explore different biological applications and each originated for a different reason.

Using dynamical systems to examine biological problems, the subtitle of this work, may seem too general to many readers, and it is general, but my research has been a series of at first seemingly unrelated questions. The binding thread is the use of the mathematics of dynamical systems to understand applied questions in biology. The nature of the applications to biology have ranged from a data driven problem about immune cell activation to an abstract problem on oscillators and finally to an examination of information transfer in populations of fish.

1.1 Immune Cell Activation

The immune system and, in particular, inflammation appears in popular news articles almost daily. In an effort to perform research on a practically applied biological question, I turned to immunology to find a problem as it is a field rich with many open questions and a plethora of data. Principally, I was interested in a project where I could involve experimental data with a model. With the guidance of Dr. Matthias Hesse, I began work on the question of activation in

macrophages, an innate immune cell. Part of this work involved performing actual biological experiments in Dr. Hesse's lab.

Chapter 2 is my paper *From inflammation to wound healing: using a simple model to understand the functional versatility of murine macrophages*, in preparation for publication. This paper presents a mathematical and experimental examination of macrophage activation along inflammation and repair pathways.

1.2 Forced Kuramoto Model

Coupled oscillators are a quintessential example used in the study of dynamical and the Kuramoto oscillator formulation of coupled oscillators is one many great scientists have examined in a variety of forms. Until recently there remained several interesting problems where little forward progress was being made.

In 2008, Dr. Edward Ott and Dr. Thomas Antonsen of Maryland University presented a breakthrough in the field of coupled oscillators, by proving the existence of an inertial manifold of order parameter dynamics under particular analytical conditions. This work renewed interest in many questions in the field of coupled oscillators. Dr. Ott and Dr. Antonsen were generous enough to share their pre-print with Dr. Strogatz and myself. From this paper I became interested in previous work by Dr. Ott and Dr. Antonsen on the forced Kuramoto oscillator that had attempted to analytically determine the complete bifurcation diagram of this model.

Chapter 3 is my paper *Stability Diagram of the Forced Kuramoto Model*, pub-

lished in Chaos in December 2008. This paper presents a complete bifurcation analysis of the forced Kuramoto model for a special case when the dynamics collapse to two-dimensions.

1.3 Consensus Decision Making in Fish Schools

The coordinated motion of organisms such as flocks of birds and schools of fish has long fascinated many. After hearing a lecture by Dr. Iain Couzin, describing the mathematics he used to study information in fish schools, I contemplated the potential of dynamical systems to such studies. After speaking with Dr. Couzin I began exploring the use of coupled oscillator models and dynamical systems analysis in collaboration with the ongoing mathematical and experimental research in the Couzin lab at Princeton University.

Chapter 4 discusses my ongoing research into consensus decision making in schools of fish. This chapter presents a mathematical exploration of the essential aspects of consensus decision making in the presence of conflicting information in fish schools.

CHAPTER 2

FROM INFLAMMATION TO WOUND HEALING: USING A SIMPLE MODEL TO UNDERSTAND THE FUNCTIONAL VERSATILITY OF MURINE MACROPHAGES

2.1 Introduction

The mammalian immune system is responsible for maintaining homeostatic conditions within the body and survival of the host. A tightly controlled synergism between the two branches - innate and adaptive - of the mammalian immune system protects the host, while failure to establish or maintain homeostasis causes disease. Every successful immune response includes the detection of potential threats to the host, such as invading pathogenic organisms, induction of a sufficient inflammatory response to control or eliminate the threat, subsequent down regulation of the inflammatory response and finally repair of tissue damaged by the pathogen and the immune response.

Recent data demonstrate that populations of murine macrophages follow different activation pathways which elicit different physiological functions [1]. However, the central questions of how individual macrophages initiate along these different pathways remains unanswered. Can individual cells switch from a pathway that involves inflammation – killing invading pathogens and protecting the host – to a repair pathway – aiding wound healing [1], [2], [3]? Additionally, are there distinct macrophages within the population that are activated uniquely along one pathway or the other? Or does a change in functional direction require the exchange of local macrophage populations? In other words, the functional stability of individual macrophages is still largely unknown.

In this paper, we investigate through a simple mathematical model and biological experimentation the flexibility of individual macrophages activated under inflammatory and repair conditions.

2.1.1 Inflammation

Activation of the immune system initiates an inflammatory response, characterized by redness, swelling, heat and pain [4], [5]. Any inflammatory response has to be flexible. While it is necessary to eradicate or control the invading pathogen, excessive damage to host tissue must be avoided. The immune response has to adapt to changing conditions in the inflamed tissue; failure to do so will cause severe disease [6], [7]. The regulatory mechanisms, which control and adjust immune responses, are still not well understood and are the object of intensive research efforts.

While most activated adaptive immune cells such as T-cells develop a relative stable functional profile, which leads to the generation of immunological memory [8], the stability or flexibility of activated macrophages has not been sufficiently investigated. The fact that macrophages do not generate an immunological memory response in contrast to T-cells suggests that these cells are rather flexible in their functional determination upon activation.

Macrophages are intimately involved in inflammation. They are essential for detecting invading pathogens and tissue destruction. They attract and activate other immune cells, both innate and adaptive, by releasing small circulating proteins, cytokines and chemokines, and by presenting pathogen-derived antigens. They also actively destroy pathogens by phagocytosis. Even without

pathogens, macrophages clear tissue debris and dying immune cells. In addition to their role in the initial inflammatory response, they actively participate in the clearance of inflammation through repair. They heal wounds with the aid of collagen production [9].

2.1.2 Macrophage Biological Background

Two main types of macrophages, tissue-residing and circulating, exist. Before macrophages can perform any of their functions, they must be activated. Activation is induced by a variety of receptor-derived signals. Some of these receptors recognize commonly found signature molecules derived from pathogens (PAMP) or from tissue damage (DAMP), while others bind to specific cytokines, small circulating signaling proteins. Although there is a variety of types of macrophage activation, the two functional patterns of macrophages which have received the most extensive study and which we will consider in this paper are microbial-pathogen induced inflammation, known as classical activation (caMa), and helminth-induced inflammation or tissue repair, known as alternative activation (aaMa). These two functional patterns have traditionally been thought to be mutually exclusive: a macrophage is either activated along the classical pathway or the alternative pathway, but not both [10], similar to the dichotomy in the profiles of T-helper-1 and T-helper-2 effector T cells.

The proper course of macrophage activation is essential for host survival. Dramatic changes in the outcome of an immune response due to macrophage activation were demonstrated in murine models of Schistosomiasis, a chronic inflammatory disease of humans in the tropics and subtropics, caused be persis-

tent infections with trematode parasites. The invading parasite causes a moderate cytotoxic (T-helper-1 cytokine) dominated immune response. When the mature female worm lays eggs there is a dramatic switch to humoral (T-helper-2 cytokine) inflammation in the infected host. Disease progression into the chronic stage is characterized by reduction of the inflammatory response [11]. These changes are reflected in the activation pattern of macrophages. While initially most macrophages are activated along the inflammatory pathway, the ensuing change in cytokine response causes a dominant repair phenotype in the macrophage population at the site of original inflammation [12], [13]. Failure to change the functional phenotype of macrophages in the tissue from inflammatory to repair leads to massive tissue damage and subsequent death of the host [14]. A change in macrophage activation has also been reported during the inflammatory response against other parasites and in wound healing models [15].

The dichotomy of L-arginine metabolism is one of the hallmarks of classical versus alternative macrophage activation [16], [10]. Both pathways involve competition for the same substrate, L-arginine (Figure 2.1). Inducible Nitric Oxide Synthase (NOS-2) is the enzyme of the classical pathway and Arginase-1 is the enzyme of the alternative pathway. The propensity towards either classical activation or alternative activation depends not only on the amount of each enzyme present in the cell but also on each enzyme's ability to bind sufficient substrate and the presence of inhibitors.

Classical Activation

Classical activation was discovered first, and for many years thereafter, was thought to be the only functional phenotype of macrophages during inflamma-

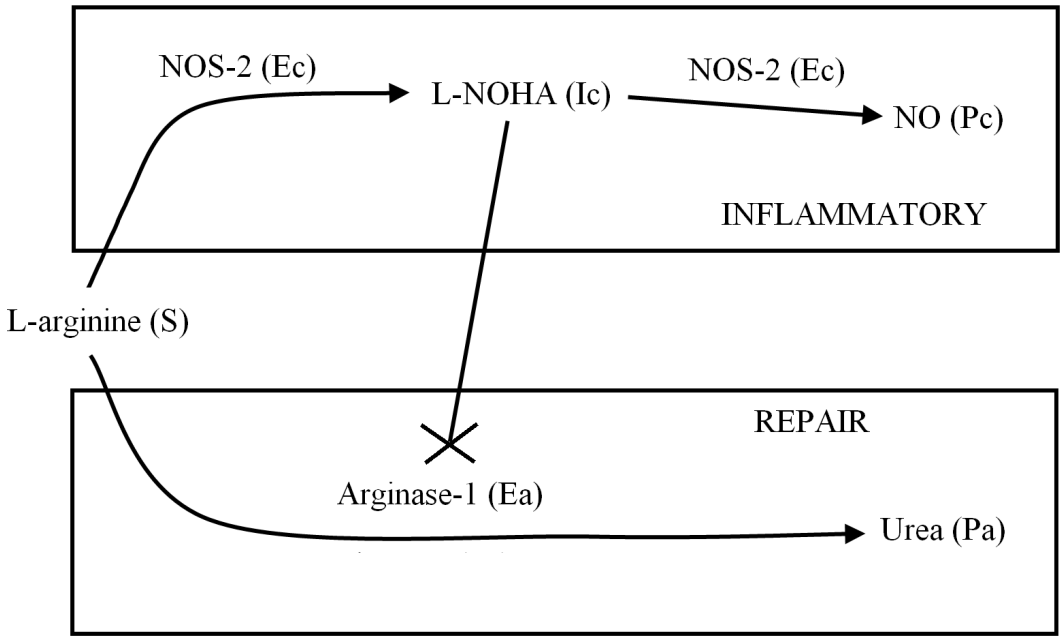

Figure 2.1: Diagram of Biological Interactions of Macrophage Activation

The top box represents the Inflammatory or Classical Activation pathway. The bottom box represents the Repair or Alternative Activation pathway. The substrate, L-arginine, is used by both pathways. NOS-2 (E_C) is the enzyme of the inflammatory pathway. Arginase-1 (E_A) is the enzyme of the repair pathway. The product of the inflammatory pathway is Nitric Oxide (P_C) while the product of the repair pathway is Urea (P_A).

tion [17]. Classical activation is induced by exposure to the cytokines Interferon-γ (IFN-γ) and Tumor Necrosis Factor-α (TNF-α) [18]. Recognition of PAMPs, such as Lipopolysaccharide (LPS) or unmethylated cytosine and guanine (CpG) rich oligonucleotides, also induces classical activation of macrophages [19], [20], [21]. Ligation of IFN-γ activates the Signal Transducers and Activation of Transcription (STAT) -1 signal transduction pathway [20] and thereby induces the expression of NOS-2. Substrate binding of L-arginine stabilizes the NOS-2 complex [22] and subsequently leads to the production of an intermediate, N-omegahydroxy-L-arginine (L-NOHA). This intermediate is ultimately metabolized into Nitric Oxide (NO) and L-citrulline [18]. NO is a free radical that has high toxicity to pathogens but also to host cells. Although most NO is utilized for the intracellular destruction of phagocytized microbes, caMa can release NO into the extracellular environment where it can harm not only pathogens but also neighboring cells. When it damages self cells this is known as immune-mediated pathology [23].

Interaction between classical and alternative activation occurs with the intermediate, L-NOHA, formed during the production of NO [24]. L-NOHA preferentially binds the enzyme of the alternative pathway, Arginase-1, and prevents the binding of Arginase-1 to the substrate, L-arginine [25], [15], [26]. This interaction establishes a relative dominance of the classical pathway over the alternative pathway because the intermediate of the classical pathway actively inhibits the enzyme of the alternative pathway (Figure 2.1). We expect that once the classical pathway has been initiated it is difficult to alter the activation state of a macrophage.

Alternative Activation

Although alternative activation of macrophages was discovered 15 years ago [28], its importance was not immediately recognized. Today there is no doubt that aaMa have a central role in many aspects of inflammatory responses, such as chronic inflammation, atopies, fibrosis, maternal tolerance and immunity against infections, among others [29]. Alternative activation is induced by exposure to cytokines Interleukin-4 (IL-4), Interleukin-13 (IL-13) and a small messenger molecule, cyclic adenosine monophosphate (cAMP) [16]. The cytokines Interleukin-10 (IL-10) and Interleukin-21 (IL-21) enhance alternative activation induced by IL-4 or IL-13 [30]. IL-4 and IL-13 induce the STAT-6 signal transduction pathway leading to the upregulation of Arginase-1 expression. Once Arginase-1 is upregulated, it is a functionally stable molecule, regardless of the presence or absence of its substrate, L-arginine. Arginase-1 hydrolyzes L-arginine into L-ornithine and Urea. In hepatocytes Arginase-1 is an essential enzyme of the urea cycle, which detoxifies ammonia in mammals [26].

As mentioned previously, the presence of L-NOHA binds Arginase-1 and blocks the substrate accessibility of Arginase-1, effectively halting alternative activation. However, in the absence of L-NOHA, Arginase-1 can access L-arginine, even at very low concentrations, because of its functional stability. This is in contrast to NOS-2 which requires the presence of L-arginine for stability; there is a minimum level of L-arginine needed for NOS-2 to be effective [22]. We speculate that a strong induction of NOS-2 expression will be sufficient to induce some minimum production of L-NOHA, which will increasingly block the ability of Arginase-1 to bind and metabolize L-arginine. This will enable individual macrophages to change from alternative to classical activation.

As macrophages play an essential role in inflammation and tissue repair, understanding if individual macrophages can switch between the two pathways will significantly improve our understanding of immune responses and could help to design new therapeutic strategies for a number of immune-mediated diseases.

2.2 Model Formulation

We designed a model of the intracellular interactions of the substrate and enzymes involved with the L-arginine dichotomy within an individual macrophage. In the formulation of the model, an individual macrophage can enter both alternative and classical pathways, dependent on the presence or absence of particular cytokines.

2.2.1 Simplifying Assumptions

This model is not meant to be a completely accurate description of macrophage activation, but rather an incorporation of the key components of macrophage activation. There are five necessary simplifying assumptions we make during the formulation of the model, described below.

First, we assume that there is perfect signal transduction within the macrophage. In other words, given a particular cytokine signal, we assume that the corresponding enzymes are upregulated to the full extent. Thus, the concentration of IFN-γ directly determines the concentration of NOS-2 in the model and the concentration of IL-4 directly determines the concentration of

Arginase-1 in the model.

Second, we assume that Arginase-1 and NOS-2 act as standard enzymes in enzyme kinetics when they interact with L-arginine. That is, they reversibly form a substrate-enzyme complex before that complex irreversibly forms a product and releases the enzyme. This assumption allows us to write an ODE model of the system using Law of Mass Action kinetics.

Third, we assume none of the substances degrade appreciably on the time scale we are modeling. Thus, our equations do not include terms for degradation and all of the terms in our equations come directly from the Law of Mass Action description of our biological system.

Fourth, our model is completely deterministic. All of the substances considered appear in picomolar quantities or larger within an individual cell, so there are at least 10^{10} molecules per cell. This is a sufficient amount to assure that in a well-mixed environment, which we assume here, chance does not affect the level of interactions.

Fifth, we assume a large, fixed amount of substrate, L-arginine, is available within the cell initially. This amount of substrate is used during the reactions and is not replenished. Thus, we are not involving the cationic transporter system, which is responsible for transporting the store of L-arginine from the extracellular matrix into the cell.

2.2.2 Mathematical Formulation

The biology of the system can be written as four chemical kinetic equations as in Equation (2.1). The subscripts C and A refer to molecules associated with the classical and alternative pathways, respectively. As the first three equations follow standard enzyme kinetics, substrate-enzyme complexes (denoted with a colon between the substrate and the enzyme) are formed reversibly and are irreversibly turned into product, releasing the enzyme. The first equation, denoted $C1$, describes the formation of the classical intermediate, I_C, from the interaction of the substrate, S, with the classical enzyme, E_C. The second equation, denoted $C2$, describes the formation of the classical product, P_C, from the interaction of the classical intermediate, I_C, with the classical enzyme, E_C. $C1$ and $C2$ delineate the full classical pathway. The third equation, denoted $A1$, describes the formation of the alternative product, P_A, from the interaction of the substrate, S, with the alternative enzyme, E_A. The final equation, denoted $A2$, models the reversible inhibition of the alternative enzyme, E_A through interaction with the classical intermediate, I_C. The rate constants are denoted by the equation number and the direction: forward (F), reverse (R), or irreversible (IR). The biological name of the compounds described here are found in Table 2.1.

$$
\begin{aligned}
C1: &\quad S + E_C \underset{k_{C1-R}}{\overset{k_{C1-F}}{\rightleftarrows}} S : E_C \xrightarrow{k_{C1-IR}} E_C + I_C \\
C2: &\quad I_C + E_C \underset{k_{C2-R}}{\overset{k_{C2-F}}{\rightleftarrows}} I_C : E_C \xrightarrow{k_{C2-IR}} E_C + P_C \\
A1: &\quad S + E_A \underset{k_{A1-R}}{\overset{k_{A1-F}}{\rightleftarrows}} S : E_A \xrightarrow{k_{A1-IR}} E_A + P_A \\
A2: &\quad I_C + E_A \underset{k_{A2-R}}{\overset{k_{A2-F}}{\rightleftarrows}} I_C : E_A
\end{aligned}
\tag{2.1}
$$

Table 2.1: Molecular Components of Macrophage Activation

Type	Variable	Substance	Pathway
substrate	S	L-arginine	Both
enzyme	E_C	NOS-2	Classical
intermediate	$S : E_C$	L-arginine:NOS-2 Complex	Classical
intermediate	I_C	L-NOHA	Classical
intermediate	$I_C : E_C$	L-NOHA:NOS-2 Complex	Classical
product	P_C	NO	Classical
enzyme	E_A	Arginase-1	Alternative
intermediate	$S : E_A$	L-arginine:NOS-2 Complex	Alternative
product	P_A	L-ornithine	Alternative
inhibited enzyme	$I_C : E_A$	Inhibited Arginase-1	Both
cytokine	N/A	IFN-γ	Classical
danger signal	N/A	CpG	Classical
cytokine	N/A	IL-4	Alternative
adjuvant	N/A	cAMP	Alternative

Classical activation indicates the presence of the enzyme, E_C, the complexes, $S : E_C$ and $I_C : E_C$, the intermediate I_C, and the product P_C. Alternative activation indicates the presence of the enzymes, E_A and $I_C : E_A$, the complex $S : E_A$, and the product P_A. These chemical equations were then written as a system of ten ODEs using Law of Mass Action kinetics.

Substrate:

$$\frac{d}{dt} S = -k_{C1-F}\, S E_C + k_{C1-R}\, S : E_C - k_{A1-F}\, S E_A + k_{A1-R}\, S : E_A \tag{2.2}$$

Classical:

$$\frac{d}{dt} E_C = -k_{C1-F}\, S E_C + (k_{C2-R} + k_{C2-IR})\, I_C : E_C + (k_{C1-R} + k_{C1-IR})\, S : E_C - k_{C2-F}\, E_C I_C \tag{2.3}$$

$$\frac{d}{dt} S : E_C = k_{C1-F}\, S E_C - (k_{C1-R} + k_{C1-IR})\, S : E_C \tag{2.4}$$

$$\frac{d}{dt} I_C = k_{C1-IR}\, S : E_C - k_{C2-F}\, E_C\, I_C + k_{C2-R}\, I_C : E_C - k_{A2-F}\, I_C\, E_A + k_{A2-R}\, I_C : E_A \tag{2.5}$$

$$\frac{d}{dt} I_C : E_C = k_{C2-F}\, E_C I_C - (k_{C2-R} + k_{C2-IR})\, I_C : E_C \tag{2.6}$$

$$\frac{d}{dt} P_C = k_{C2_IR}\, I_C : E_C \tag{2.7}$$

Alternative:

$$\frac{d}{dt} E_A = -k_{A1-F}\, S E_A + (k_{A1-R} + k_{A1-IR})\, S : E_A - k_{A2-F}\, I_C\, E_A + k_{A2-R}\, I_C : E_A \tag{2.8}$$

$$\frac{d}{dt} S : E_A = k_{A1-F}\, S E_A - (k_{A1-R} + k_{A1-IR})\, S : E_A \tag{2.9}$$

$$\frac{d}{dt} P_A = k_{A1-IR}\, S : E_A \tag{2.10}$$

$$\frac{d}{dt} I_C : E_A = k_{A2-F}\, I_C E_A - k_{A2-R}\, I_C : E_A \tag{2.11}$$

2.2.3 Reducing the System

After examining the equations, it was clear that the full ten equations were not needed to describe our system. Equations (2.3), (2.4), and (2.6) sum to zero, as

well as Equations (2.8), (2.9), and (2.11) also sum to zero:

$$\frac{d}{dt} E_C + \frac{d}{dt} S : E_C + \frac{d}{dt} I_C : E_C = 0 \tag{2.12}$$

$$\frac{d}{dt} E_A + \frac{d}{dt} S : E_A + \frac{d}{dt} I_C : E_A = 0 \tag{2.13}$$

Considering only biologically relevant parameter sets, we know that all intermediates and products have initial values of zero and both enzymes have initial values related to the level of cytokines introduced to the system. Thus, $E_C(0) = \text{constant}$, $S : E_C(0) = 0$, $IC : E_C(0) = 0$, $E_A(0) = \text{constant}$, $S : E_A(0) = 0$, and $I_C : E_A(0) = 0$. Thus, we integrate the above Equations (2.12) and (2.13) using our known initial conditions to get the following equalities:

$$E_C + S : E_C + I_C : E_C = E_C(0) \tag{2.14}$$

$$E_A + S : E_A + I_C : E_A = E_A(0) \tag{2.15}$$

By substituting for $I_C : E_C = E_C(0) - E_C - S : E_C$ and $I_C : E_A = E_A(0) - E_A - S : E_A$ into our original system of equations the number of equations is reduced by two. For the remainder of our analysis, we will work with the reduced eight-equation system.

A more careful examination of our equations allows us to temporarily ignore the rate equations (2.7) and (2.10), for P_C and P_A respectively, because the rest of the system of does not depend on P_C or P_A. Once we determine the time course of $I_C : E_C$, $S : E_A$, and $I_C : E_A$ we can then determine the behavior of P_C and P_A, respectively.

2.2.4 Rate Constants

There are 11 rate constants in the model. Unfortunately, none of these constants are precisely measurable through experimentation. There exists, however, information from the literature (calculated through experimentation by others) about ratios of various rate constants [31], [32]. More information is known about the ratio of Michaelis-Menten constants, which are constants that denote particular relationships between rate constants based on an assumption of quasi-steady state of the intermediate. Michaelis-Menten constants have the standard form $\frac{k_R+k_{IR}}{k_F}$. Through the literature we know that the Michaelis-Menten constant of classical activation for the formation of NO from L-arginine via NOS-2 is much smaller than the Michaelis-Menten constant of alternative activation for the formation of L-ornithine from L-arginine via Arginase-1 [32], [33]. Since the formation of NO (P_C) is a two step process and has a smaller Michaelis-Menten constant than the formation of L-ornithine (P_A), then the Michaelis-Menten constant of both steps to form NO (P_C), multiplied together, is less than the Michaelis-Menten constant of the formation of Urea (P_A):

$$\frac{k_{A1-R} + k_{A1-IR}}{k_{A1-F}} >> \left(\frac{k_{C1-R} + k_{C1-IR}}{k_{C1-F}}\right)\left(\frac{k_{C2-R} + k_{C2-IR}}{k_{C2-F}}\right)$$

Information on the relative size of rate constants can be inferred by the stability of compounds. For example, it is inferred that $k_{A1-F} > k_{C1-F}$ because Arginase-1 (E_A)does not require auxiliary molecules for stable formation while NOS-2 (E_C) does require the presence of L-arginine to become fully functional and avoid rapid degradation [34]. Furthermore, we know that L-NOHA binds preferentially to Arginase-1 over NOS-2 so $k_{A2-F} > k_{C2-F}$ [27].

Using these constraints and approximate values from the literature, initial guesses of the parameters were determined. The parameters were then optimized using *SloppyCell*, a program that selects parameters by comparison to experimental time series data [35]. The idea behind the program is that the eigendirections where a wide range of parameter values are consistent with data are called sloppy while the eigendirections which are considerably more restricted are called stiff. The goal is set the stiff parameters in the center of their appropriate regimes by altering the sloppy parameters still within their valid regimes. This is possible because the sloppy parameters can be moved over a large range. The time series data from our most basic experiments was used as the experimental time series data. The precise values of rate constants used are in Table 2.2.

2.3 Simulations

Using the optimized rate constants, we tested our mathematical model with simulations. We varied the initial level of enzyme to determine how the level of product depends on the level of enzyme in the system.

In our basic simulations, we introduced varying initial levels of one enzyme, either NOS-2 (E_C)or Arginase-1 (E_A), and allowed the simulation to run for the equivalent of fifty hours. These results (data not shown) were analogous to our single stimulation experimental results. An increased level of NOS-2 (E_C) produced NO (P_C) but no Urea (P_A), while an increased level of Arginase-1 (E_A) produced Urea (P_A) but no NO (P_C).

Table 2.2: Rate Constants of Macrophage Activation

Equation	Rate	Symbol	Value
C1	synthesis of $S : E_C$	k_{C1-F}	10^6 $\text{sec}^{-1}\text{mol}^{-1}$
C1	decomposition of $S : E_C$	k_{C1-R}	10 sec^{-1}
C1	synthesis of I_C	k_{C1-IR}	10^4 sec^{-1}
C2	synthesis of $I_C : E_C$	k_{C2-F}	10^8 $\text{sec}^{-1}\text{mol}^{-1}$
C2	decomposition of $I_C : E_C$	k_{C2-R}	10 sec^{-1}
C2	synthesis of P_C	k_{C2-IR}	10^3 sec^{-1}
A1	synthesis of $S : E_A$	k_{A1-F}	10^8 $\text{sec}^{-1}\text{mol}^{-1}$
A1	decomposition of $S : E_A$	k_{A1-R}	10^4 sec^{-1}
A1	synthesis of P_A	k_{A1-IR}	10^4 sec^{-1}
A2	synthesis of $I_C : E_A$	k_{A2-F}	10^9 $\text{sec}^{-1}\text{mol}^{-1}$
A2	decomposition of $I_C : E_A$	k_{A2-R}	10^2 sec^{-1}

In subsequent simulations, we introduced both enzymes simultaneously. When both enzymes were introduced together, only a substantial level of NO (P_C) and not of Urea (P_A), was produced (data not shown) as the classical activation overpowered alternative activation. This is analogous to data from the literature [37, 38].

In our final simulations, we introduced both enzymes at separate time points during the fifty hour time course to examine how the products change in response to changes in the environment. In the first simulation, we initially introduced only Arginase-1 (E_A) indicative of alternative activation. After 25 hours, we reset the level of Arginase-1 (E_A) and all associated intermediates to zero and elevated the level of NOS-2 (E_C), indicative of classical activation. We let

the simulation continue to run for another 25 hours (total of 50 hours). During the first 25 hours, the level of Urea (P_A) become elevated. However, the amount of NO (P_C) produced in the final 25 hours after the introduction of NOS-2 (E_C) eclipsed the level of Urea (P_A) (Figure 2.2(a)).

In the second simulation, we first introduced only NOS-2 (E_C). After 25 hours we reset the level of NOS-2 (E_C) and all associated intermediates to zero and elevated the level of Arginase-1 (E_A). We then let the simulation continue to run for another 25 hours (total of 50 hours). During the first 25 hours, the level of NO (P_C) was significantly elevated. Although the level of Urea (P_A) became elevated during the final 25 hours, it was negligible compared to the level of NO (P_C) already created (Figure 2.2(b)).

Our simulations indicated that it was possible to switch from alternative activation to classical activation (Figure 2.2(a)). However, the opposite switch, from classical activation to alternative activation, was not possible (Figure 2.2(b)).

2.4 Analysis of the Mathematical Model

Although we saw consistent results with our simulations, we wanted to examine the model analytically to fully understand the dynamics. We examined the asymptotic behavior of the system under a biologically relevant choices of parameters.

Figure 2.2: Mathematical Simulations of 10 ODE System

Simulation results of our 10 ODE system run in Matlab using ode45 with a variable step-size.

(a) At the onset of the simulation the alternative enzyme (E_A) was upregulated, analogous to the addition of IL-4 and cAMP in an experimental system. After 25 hours, the alternative enzyme is removed along with the associated alternative intermediates. Then, the classical enzyme (E_C), analogous to the addition of IFN-γ and CpG experimentally, was upregulated. The level of Nitric Oxide (P_C) is shown in a dashed line and the level of Urea (P_A) is shown in a solid line.

(b) At the onset of the simulation the classical enzyme (E_C) was upregulated, analogous to the addition of IFN-γ and CpG in an experimental system. After 25 hours, the classical enzyme is removed along with the associated classical intermediates. Then, the alternative enzyme (E_A), analogous to the addition of IL-4 and cAMP, was upregulated. The level of Nitric Oxide (P_C) is shown in a dashed line and the level of Urea (P_A) is shown in a solid line.

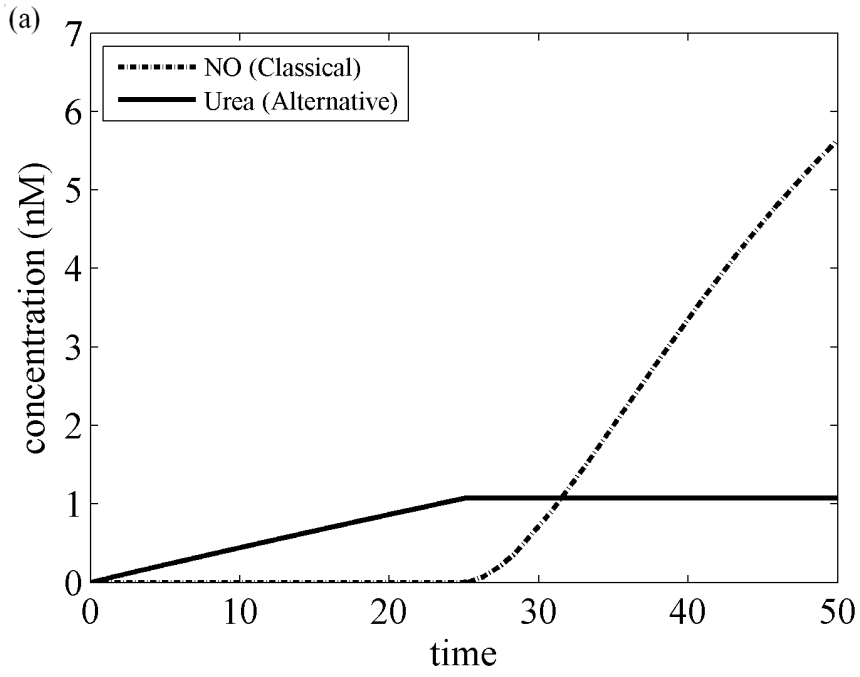
(a)
NO (Classical)
Urea (Alternative)
concentration (nM)
time
0
1
2
3
4
5
6
7
0
10
20
30
40
50

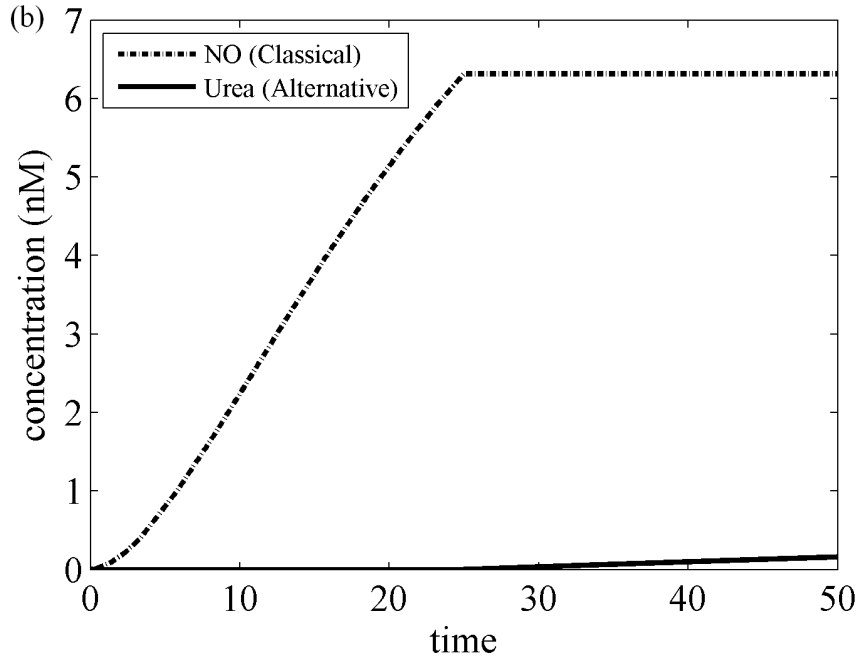
(b)
NO (Classical)
Urea (Alternative)
concentration (nM)
time
0
1
2
3
4
5
6
7
0
10
20
30
40
50

2.4.1 Fixed Points of the 8 ODE System

We began by looking for long term solution or fixed point of our equations. To solve for fixed points, we look for solutions when all eight ODEs are equal to zero. To determine the stability of the fixed points we examine the eigenvalues of the Jacobian evaluated at our fixed point. Solving for the fixed points of the system, we find there is only one:

$$\begin{array}{ll} S = 0 & P_C = \text{unconstrained} \\ E_C = E_C(0) & E_A = E_A(0) \\ S : E_C = 0 & P_A = \text{unconstrained} \\ I_C = 0 & I_C : E_A = 0 \end{array}$$

The equilibrium value of the products P_C and P_A depends on the time course of intermediates, I_C and $S : E_A$, $I_C : E_A$, respectively.

This fixed point is stable because the eigenvalues all have negative real parts except two which are zero. These two zero eigenvalues corresponding to the P_C and P_A directions we can ignore, because they do not affect the system. The remaining six eigenvalues are roots of cubic polynomials with positive coefficients, which satisfy the Routh-Hurwitz criterion. This indicates all roots have negative real parts. Thus the eigenvalues of the Jacobian lie in the left half plane indicating stability of our fixed point. The coefficients examined under the Routh-Hurwitz criterion stay negative for all positive values of the rate constants, which constitutes the biologically relevant regime of parameters.

2.4.2 Analysis within Particular Parameter Regimes

No further analysis can be performed on the full system because of the quadratic non-linearities. Thus, we examine the particular case of solely alternative activation.

Alternative Activation

If we assume that we only stimulate with the cytokine IL-4 and the associated messenger cAMP, then only Arginase-1 (E_A) is upregulated. Thus, we assume there is no initial NOS-2 ($E_C(0) = 0$) and there never is NOS-2 (E_C) in the system. Since there is no NOS-2 (E_C), or any other classically associated intermediates or products initially and no E_C appears, then $E_C = 0$ remains for all time. For the same reasons, all of the classically associated intermediates and products are zero for all time: $S : E_C = 0$, $I_C = 0$, $I_C : E_C = 0$, $P_C = 0$. Since the classical intermediate (I_C) is zero for all time and as well as inhibited Arginase ($I_C : E_A$) is zero, the Equation (2.11) for $\frac{d}{dt}\, I_C : E_A$, also equals zero for all time. The amount of inhibited Arginase-1 ($I_C : E_A$) always remains zero. Arginase-1 ($I_C : E_A$) is never inhibited, because the intermediate of the classical pathway ($I_C : E_C$) is never present.

With these restrictions, the system reduces to:

$$\frac{d}{dt}\, S = -k_{A1-F} S\ E_A + k_{A1-R}(E_A(0) - E_A) \tag{2.16}$$

$$\frac{d}{dt}\, E_A = -k_{A1-F} S\ E_A + (k_{A1-R} + k_{A1-IR})(E_A(0) - E_A) \tag{2.17}$$

$$\frac{d}{dt}\, P_A = k_{A1-IR}(E_A(0) - E_A) \tag{2.18}$$

We notice that S and E_A do not depend on P_A, so we can study the two-

dimensional $S - E_A$ system.

We begin by non-dimensionalizing the alternative activation sub-system by making the following substitutions:

$$\begin{aligned} \tau &= tk_{A1-IR} & \beta &= \frac{k_{A1-R}}{k_{A1-IR}} & \sim 1 \\ \hat{S} &= \frac{S}{S(0)} & \epsilon_1 &= \frac{k_{A1-F}S(0)}{k_{A1-IR}} & \sim \frac{1}{10000} \\ \hat{E_A} &= \frac{E_A}{E_A(0)} & \epsilon_2 &= \frac{E_A(0)}{S(0)} & \sim \frac{1}{100} \end{aligned}$$

Note that β is $O(1)$ but ϵ_1 and ϵ_2 are very small, in fact, $\epsilon_1 \ll \epsilon_2 \ll 1$. Our two-dimensional system becomes:

$$\frac{d}{d\tau}\hat{S} = \epsilon_2(-\epsilon_1 \hat{S}\,\hat{E_A} + \beta(1 - \hat{E_A})) \tag{2.19}$$

$$\frac{d}{d\tau}\hat{E_A} = -\epsilon_1 \hat{S}\,\hat{E_A} + (1+\beta)(1 - \hat{E_A}) \tag{2.20}$$

Since $\epsilon_1 \ll 1$, we use matched asymptotics to follow the behavior of the system. Matched asymptotics is a useful method when there are multiple time scales, as we have here. There exists a small parameter, ϵ_1, which cannot be assumed to be zero. We break the problem into two regions, one where we can ignore ϵ_1, our outer layer, and one where we must consider it, our inner layer. We then strive to make the solutions "match" at the boundary between the two layers.

We begin by finding the long time or outer solution when $\epsilon_1 << \tau$. We let $\epsilon_1 = 0$ in this region. Then, we solve Equation (2.20) explicitly. The long time solution for $\hat{E_A}(\tau)$ is:

$$\hat{E_A}(\tau) = 1 - e^{-(1+\beta)\tau}$$

Plugging this into Equation (2.19), we find our complete long-time or outer so-

lution:

$$\begin{aligned}\hat{S}(\tau) &= e^{-(1+\beta)\tau} \\ \hat{E_A}(\tau) &= 1 - e^{-(1+\beta)\tau}\end{aligned}$$

Next we want to consider the region were ϵ_1 is important. To find this short-time or inner solution, we assume the slowly evolving equation (2.19) is fixed: $\frac{d}{d\tau}\hat{S} = 0$. Thus with $\hat{S}(\tau) = S(0)$ we can solve for $\hat{E_A}(\tau)$:

$$\begin{aligned}\hat{S}(\tau) &= S(0) \\ \hat{E_A}(\tau) &= \frac{1+\beta-(\epsilon_1 a_0 + 2(1+\beta))e^{-(\epsilon_1 a_0 + 1+\beta)\tau}}{-(\epsilon_1 a_0 + 1 + \beta)}\end{aligned}$$

We combine the inner and outer solutions to find the complete or composite solution.

$$\begin{aligned}\hat{S}(0) &= 1 \\ \hat{E_A}(0) &= 1 \\ \hat{S}(\tau) &= e^{\frac{-\epsilon_1\tau}{1+\beta}} \\ \hat{E_A}(\tau) &= \frac{1+\beta+\epsilon_1\, e^{\frac{-(1+\beta+\epsilon_1)\tau}{\epsilon_2}}}{1+\beta+\epsilon_1} - \frac{\epsilon_1}{1+\beta+\epsilon_1}e^{\frac{-\epsilon_1\tau}{1+\beta}} + \frac{\epsilon_1}{1+\beta+\epsilon_1}\end{aligned}$$

This gives us a closed form solution to a particular subset of our full system. Under conditions corresponding to alternative activation we can fully follow all the dynamics of the system. Unfortunately, we are not able to repeat this for classical activation conditions or the full model.

2.5 Experimental Results

We tested our mathematical model in biological experiments at the population and single cell level using the RAW 264.7 murine macrophage-like cell line. We exposed these cells to various stimuli. See Appendix for protocol.

In our experiments, we considered the presence of the classical product, NO, in the supernatant to be representative of the activation of the classical pathway. To stimulate the classical pathway, we exposed the macrophages to the cytokine IFN-γ and enhanced the stimulation with an immunostimulatory CpG oligonucleotide [36]. Alternative activation was determined by Urea production after stimulation with IL-4 and cAMP.

This initial approach did not allow detection of the activation profile of single cells. Therefore we employed transfected RAW 264.7 cells with the gene for green fluorescing protein (GFP) under control of the Arginase-1 promotor. Whenever a signaling event activated the Arginase-1 promotor the cells upregulated the expression of Arginase-1 and GFP. Hence, aaMa became GFP+. The expression of GFP in individual cells could be detected by flow cytometry after excitation with laser light at 488 nm. By flow cytometry sorting we were able to isolate viable GFP+ and GFP- cells. Our approach allowed for the first time to investigate the activation profile of macrophages at the single cell level.

2.5.1 Functional stability at the cell population level

First, we investigated the functional stability of RAW 264.7 cells at the population level. Previous data indicated that caMa populations cannot be switched

into aaMa but the reverse switch might be possible [37]. Our mathematical model made similar predications.

Initially we only stimulated one pathway at a time. IFN-γ and CpG were used together as the classical stimulus. IL-4 and cAMP were used together as the alternative stimulus. As expected, IFN-γ and CpG induced only production of NO (Figure 2.3(a)), but no Urea (Figure 2.3 (b)). In contrast, stimulation with the IL-4 and cAMP generated Urea production (Figure 2.3 (b)), but no NO (Figure 2.3 (a)).

We then considered the stimulation of both pathways at the same time, including both cytokines, IFN-γ and IL-4, as well as CpG, and cAMP to enhance the signals. As predicted, the classical stimulus dominated, and only NO (Figure 2.4 (a)), not Urea (Figure 2.4 (b)) was detected.

Next, we investigated whether stimulation with one cytokine profile and the subsequent restimulation with the opposite cytokine profile could change the activation status of RAW 264.7 cells. We exposed cells to the classical stimulus, IFN-γ and CpG, and after twenty-four hours washed them and exposed them to the alternative stimulus, IL-4 and cAMP. These cells produced the classical product, NO, within the first twenty-four hours but only produced low amounts of NO (Figure 2.5 (a)) and no Urea (Figure 2.5 (b)) upon restimulation along alternative activation. Additionally we performed the opposite switch and exposed cells to the alternative stimulus, IL-4 and cAMP, and after twenty-four hours washed them and exposed them to the classical stimulus, IFN-γ and CpG. After the initial twenty-four hours, neither NO nor Urea was detected (Figure 2.5 (a) and (b)), similar to the small amount of Urea seen after 24 hours with the single stimulus experiments (Figure 2.3(b)). However, after restimulation with the

Figure 2.3: Population Level Experimental Data, Single Stimulation

(a) Nitric Oxide concentration and (b) Urea concentration after exposure of RAW 264.7 murine macrophages at time 0 to only medium (far left) indicating no stimulus, IL-4 + cAMP (middle) indicating alternative stimulus and IFN-gamma + CpG (far right) indicating classical stimulus. Concentrations were determined from ELISA of the supernatant. Gray bars represent measurements at 24 hours. Black bars represent measurements at 48 hours. The values of p between bars represents the level of confidence at which the two means are different, using a t-test. The error bars show one standard deviation above the mean.

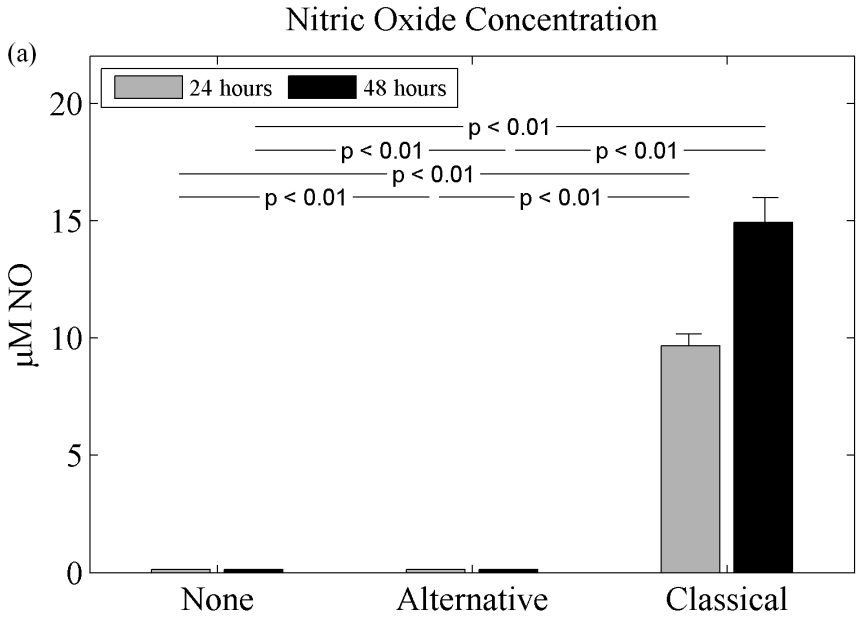
Nitric Oxide Concentration
(a)
24 hours
48 hours
p < 0.01
p < 0.01
p < 0.01
p < 0.01
p < 0.01
p < 0.01
μM NO
20
15
10
5
0
None
Alternative
Classical

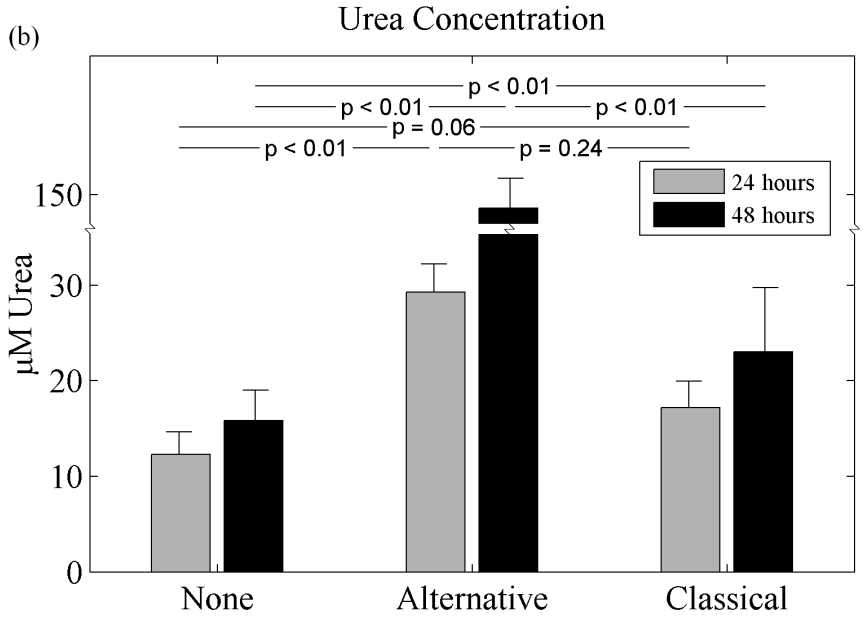
Urea Concentration
(b)
p < 0.01
p < 0.01
p < 0.01
p = 0.06
p < 0.01
p = 0.24
24 hours
48 hours
μM Urea
150
30
20
10
0
None
Alternative
Classical

Figure 2.4: Population Level Experimental Data, Double Stimulation

(a) Nitric Oxide concentration and (b) Urea concentration after exposure of RAW 264.7 murine macrophages at time 0 to only medium (left) indicating no stimulus, IL-4 + cAMP + IFN-gamma + CpG (right) indicating alternative stimulus and classical stimulus together. Concentrations were determined from ELISA of the supernatant. Gray bars represent measurements at 24 hours. Black bars represent measurements at 48 hours. The values of p between bars represents the level of confidence at which the two means are different, using a t-test. The error bars show one standard deviation above the mean.

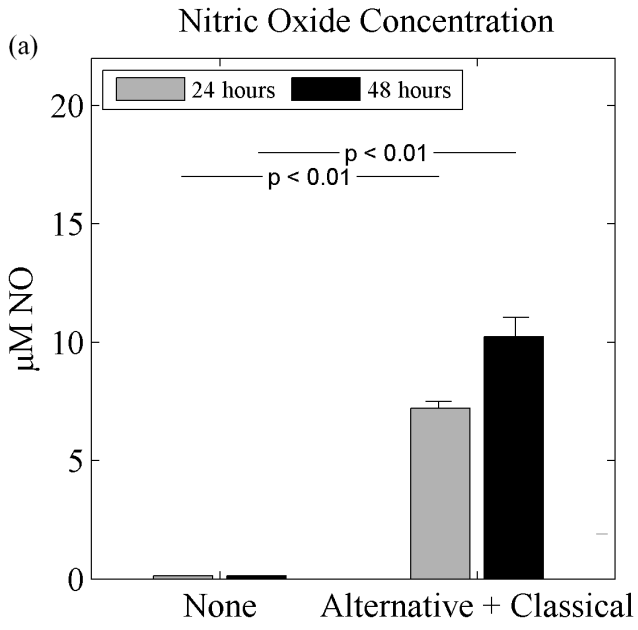
(a)
Nitric Oxide Concentration
24 hours
48 hours
p < 0.01
p < 0.01
μM NO
20
15
10
5
0
None
Alternative + Classical

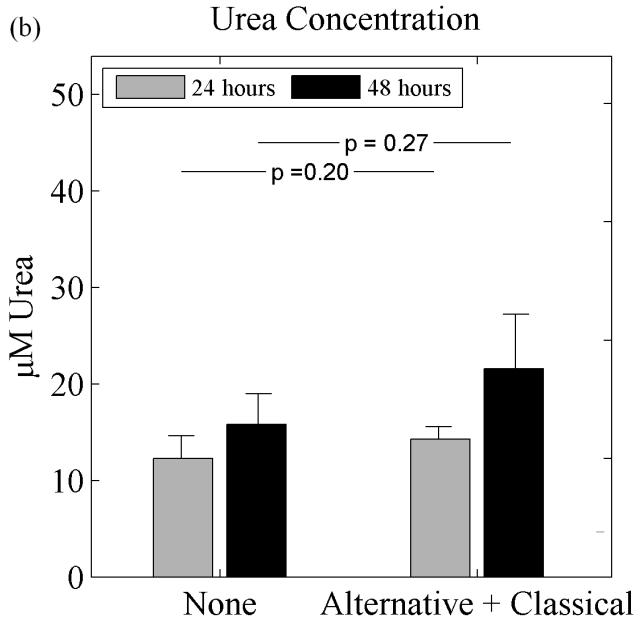
(b)
Urea Concentration
24 hours
48 hours
p = 0.27
p =0.20
μM Urea
50
40
30
20
10
0
None
Alternative + Classical

classical stimulus, the cells produced NO (Figure 2.5(a)). These results indicate the ability of the population to switch from alternative activation to classical activation but not the reverse.

2.5.2 Functional stability at the single cell level

Although our previous results appear to support our mathematical model, the experimental approach could not exclude that the change in functionality resulted from the stimulation of different subpopulations rather than the switch of individual cells, as predicted in our model. We employed Arginase-1-GFP reporter macrophages to investigate the functional flexibility of single cells.

As Arginase-1 expression is associated with the alternative pathway of macrophage activation, we expected a significant upregulation of GFP with the alternative stimulus, IL-4 and cAMP. As expected, there was a clear population-wide increase of GFP-mediated fluorescence (Figure 2.6), concomitant with increased Urea production (data not shown). Next, we sorted the cells 24 hours after the stimulation with IL-4 and cAMP into GFP-low and GFP-high expressing cells (Figure 2.6(b)). Both populations were restimulated with IFN-g and CpG for 24 hours. Subsequently, both populations released NO into the supernatant, with a higher production by the GFP+ cells (Figure 2.7). The NO production by GFP+ cells demonstrates that individual macrophages can change from alternative to classical activation.

Figure 2.5: Population Level Experimental Data, Sequential Stimulation

(a) Nitric Oxide concentration and (b) Urea concentration after exposure of RAW 264.7 murine macrophages to medium (far left) indicating no stimulus, IL-4 + CAMP (middle) indicating alternative stimulus at 0 hours followed by IFN-γ + CpG indicating classical stimulus at 24 hours, and IFN-γ + CpG (far right) indicating classical stimulus at 0 hours followed by IL-4 + cAMP indicating alternative stimulus at 24 hours. Cells were washed after 24 hours and before restimulation. Concentrations were determined from ELISA of the supernatant. Gray bars represent measurements at 24 hours. Black bars represent measurements at 48 hours. The values of p between bars represents the level of confidence at which the two means are different, using a t-test. The error bars show one standard deviation above the mean.

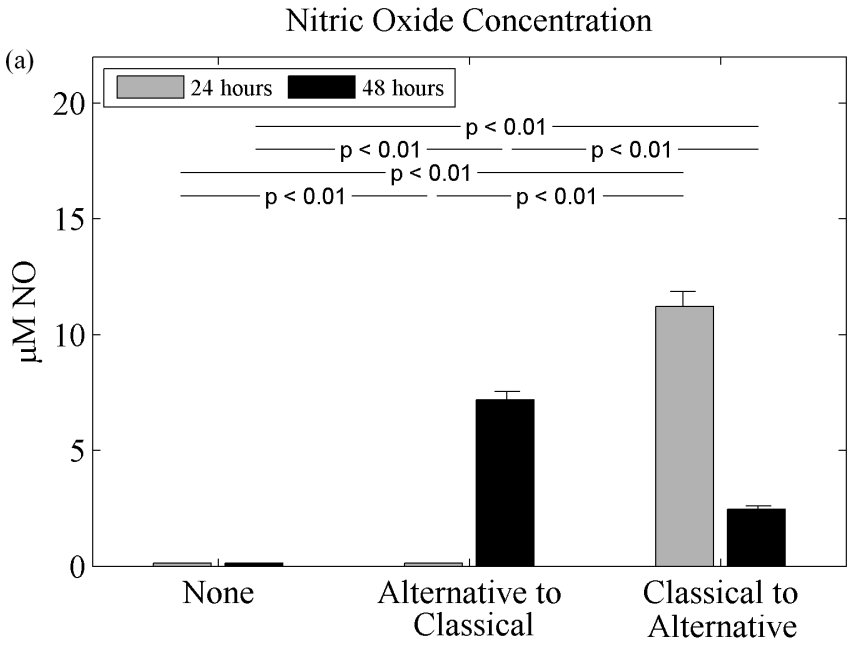
Nitric Oxide Concentration
(a)
24 hours
48 hours
p < 0.01
p < 0.01
p < 0.01
p < 0.01
p < 0.01
p < 0.01
μM NO
0
5
10
15
20
None
Alternative to Classical
Classical to Alternative

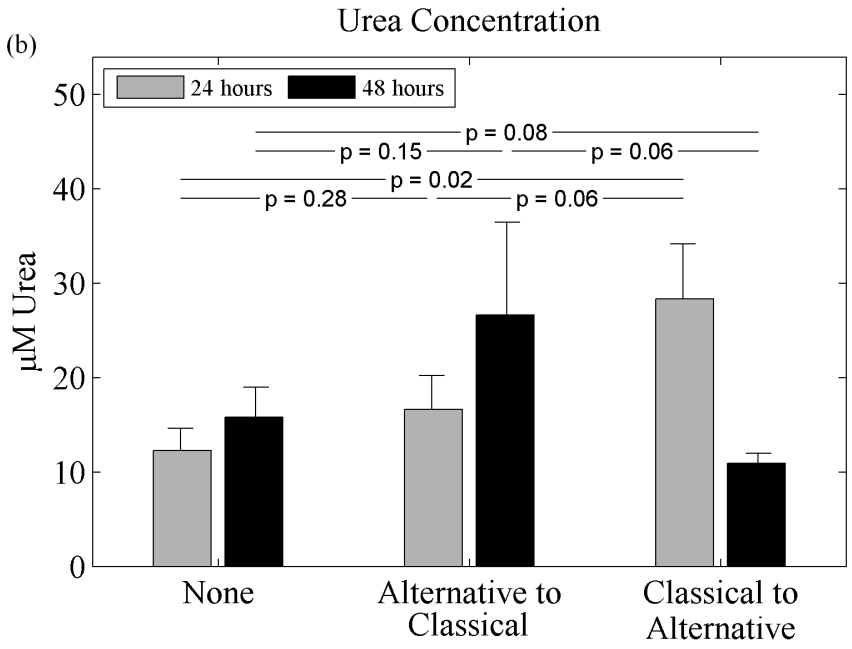
Urea Concentration
(b)
24 hours
48 hours
p = 0.08
p = 0.15
p = 0.06
p = 0.02
p = 0.28
p = 0.06
μM Urea
0
10
20
30
40
50
None
Alternative to Classical
Classical to Alternative

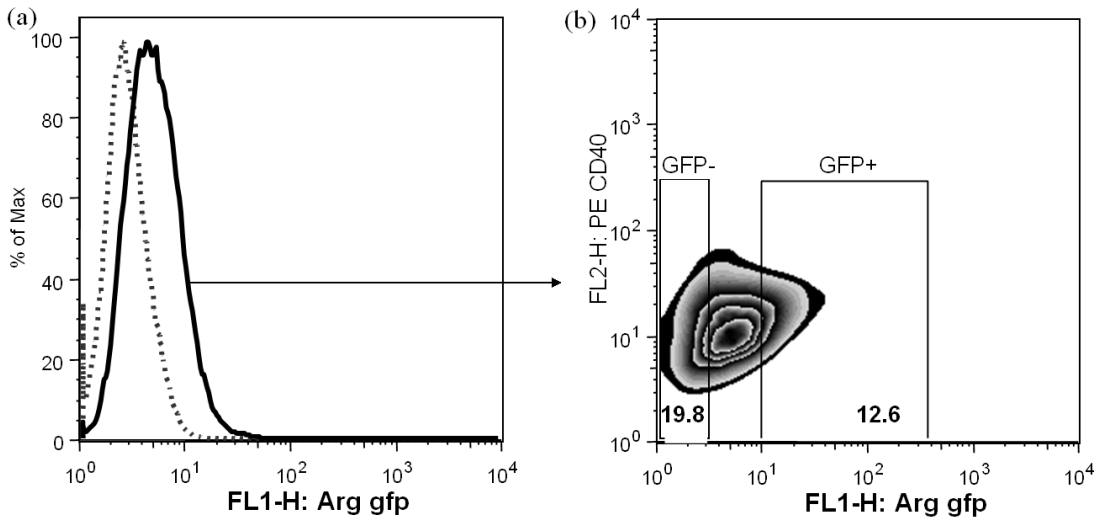

Figure 2.6: Upregulation of Arginase-1 GFP After Alternative Stimulation

RAW 264.7 macrophages were stimulated alternatively with IL-4 + cAMP. After 24 hours their fluorescence was measured on a FACS machine.

(a) The x-axis represents GFP fluorescence from activation of the Arginase-1 promotor and the y-axis represents the percentage of maximum fluorescence.

(b) The x-axis represents GFP fluorescence from activation of the Arginase-1 promotor and the y-axis measures PE CD40, a marker of inflammation. The boxes how how we gated for GFP+ and GFP- populations.

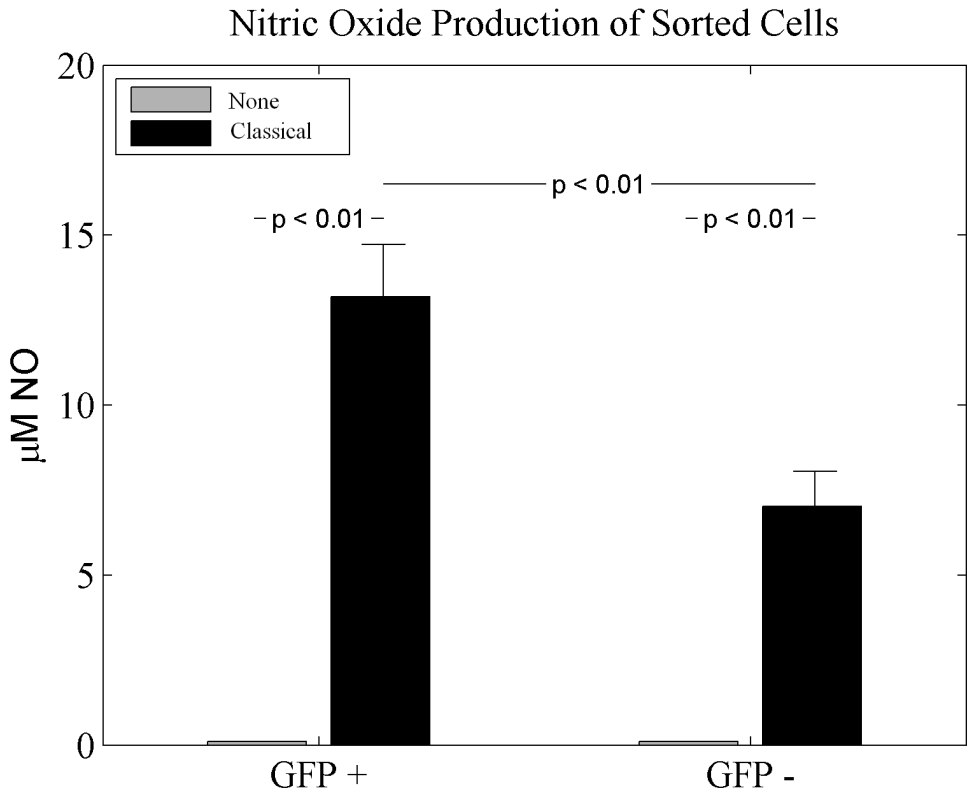

Figure 2.7: Single Cell Level Experimental Data, GFP + vs. GFP -

RAW 264.7 macrophages were stimulated alternatively with IL-4 + cAMP. After 24 hours they were sorted using a FACS machine based upon their expression of GFP, a marker for Arginase-1 promotor, as GFP + (left) or GFP - (right). The sorted cells were washed and restimulated with medium or IFN-γ + CpG. The level of Nitric Oxide in the supernatant was measured after an additional 24 hours. White bars represent restimulation with medium. Black bars represent restimulation with IFN-γ + CPG. The values of p between bars represents the level of confidence at which the two means are different, using a t-test. The error bars show one standard deviation above the mean.

2.6 Discussion

Macrophages are highly versatile cells of the innate immune system [15, 39]. Yet we still do not know how they adapt to different functional demands. Whether individual macrophages can change their functional profile or whether the exchange of cells in tissue leads to functional changes at the population level has not been understood. In the past, populations of cells were shown to change their functional phenotypes, both in vivo and in vitro [39]. It was never unequivocally determined whether individual cells were able to perform this switch.

We developed a 10 ODE mathematical model to make predictions regarding the functional flexibility of individual macrophages based on the L-arginine metabolism in classically versus alternatively activated macrophages.

Due to the non-linearities of the model, we were only able to find a closed-form solution for a subset of conditions involving only alternative activation. However, analysis of our mathematical model revealed one stable fixed point for all biologically relevant parameter values. The exact value of this fixed point is dependent upon the particular values of the initial conditions.

As we were interested in the short term dynamics of the model, on the same time scale as experiments, we examined simulations of our mathematical model. Our simulations predicted the ability of an individual macrophage to switch from alternative activation to classical activation when the environmental conditions switched from alternative to classical. The reverse switch from classical activation to alternative activation was not observed.

Then we tested our mathematical predictions using RAW 264.7 cells. These cells were stimulated in vitro to induce classical or alternative activation of macrophages. We used the metabolic products of NO from NOS-2 and Urea from Arginase as indication of each activation pathway. We found that classical activation was dominant over alternative activation at the population level. Simultaneous or consecutive stimulation caused NO production but did not result in significant Urea production. These data are in accordance with previous results [37, 38] and they are consistent with our mathematical predictions.

Next, we investigated the functional flexibility of individual aaMA using our GFP-reporter cell line. Our results demonstrate the ability of individual aaMa to develop a classical phenotype and to produce NO. It argues against a model where the phenotypic switch at the population level is mediated by a response of different subpopulations to the various stimuli. In support of this finding, a recent study in an atherosclerosis model concluded that a local switch from alternative to classical macrophage activation in the inflammatory lesions is due to the conversion of cells already present and does not require the infiltration of new macrophages [40]. However, this report did not exclude the possibility of switching local macrophages with different phenotypes.

2.6.1 Pathway Priming

To ensure an in-vivo-like model, a danger signal, CpG, was included in classical activation. When macrophages were stimulated with both IFN-γ and CpG, the classical stimulus, the cells upregulated NO production as expected, but surprisingly, many also started to express GFP an indication of the presence of

Arginase-1 (data not shown), the enzyme of the alternative pathway.

It seems the co-stimulation of cells by the classical stimulus, IFN-γ and CpG, changes the phenotype of these macrophages. The upregulation of the alternative enzyme, Arginase-1, in these cells, a process we refer to as "priming" the alternative pathway, may prove important. The presence of Arginase-1, involved with wound healing, may be a control mechanism that limits the inflammatory response exhibited by classically activated macrophages. The initial upregulation of Arginase-1 may allow the cells to be restimulated and converted to alternatively activated macrophages, which are less harmful to the body.

The finding that the classical stimulus upregulates the alternative *enzyme* but not the alternative *product* was not consistent with our mathematical model. This is expected however because the stimulus was not explicitly included in the model. Instead the stimulus was directly linked to the amount of enzyme in the model. In future work we plan to explore the model without this enforced link between cytokines and enzymes by including the signaling pathways between exposure to cytokines and the upregulation of the enzyme.

This novel finding of the "priming" of the alternative pathway by the classical pathway leads to many questions. What signaling pathway causes the unexpected upregulation of Arginase-1 in classical activation? Does this upregulation of Arginase-1 occur in the same manner as in alternative activation? What is the functional significance of the upregulation of Arginase-1 by the classical pathway?

CHAPTER 3

STABILITY DIAGRAM FOR THE FORCED KURAMOTO MODEL

The study of synchronization is a classic topic in nonlinear science. Sometimes the concern is with mutual synchronization, as in Huygens's 1665 discovery of the sympathy of pendulum clocks. In other situations, one is more interested in forced synchronization, as in the injection locking of a laser or the entrainment of circadian rhythms by the daily light-dark cycle. Here we consider a simple mathematical model in which both types of synchronization are present simultaneously, creating a conflict between them. What happens when a network of dissimilar but mutually coupled oscillators is also driven by an external periodic force? For a natural generalization of the Kuramoto model, the interaction of forcing, coupling, and randomness leads to a rich set of collective states and bifurcations. We explain all of these phenomena analytically, using an ansatz recently introduced by Ott and Antonsen.

3.1 Introduction

In 1975 Kuramoto proposed an elegant model for an enormous population of coupled biological oscillators [41, 42]. Each oscillator was described solely by its phase, with amplitude variations neglected; the oscillators were coupled all-to-all, with equal strength; the interaction between them was purely sinusoidal, with no higher harmonics; and their intrinsic frequencies were randomly distributed across the population according to a symmetric bell-shaped distribution. All of these simplifying assumptions helped Kuramoto make headway on what would otherwise have been a hopelessly intractable many-body, nonlin-

ear dynamical system. By means of an ingenious self-consistency argument, he was able to show analytically that the system could undergo a phase transition to mutual synchronization, once the coupling between the oscillators exceeded a certain threshold.

Over the past three decades, many researchers have shed light on the mathematical aspects of collective synchronization by studying Kuramoto's model and its close relatives [43, 44]. And, somewhat surprisingly in view of its simplicity, the model has also been shown to be relevant to a variety of physical systems [45, 46]. Examples range from electrochemical oscillators [47, 48] and Josephson junction arrays [49] to coupled metronomes [50], collective atomic recoil lasing [51], and neutrino flavor oscillations [52].

One way to extend the model is to allow for the effects of external forcing. This generalization is theoretically natural, but it is also motivated in part by experimentally observed phenomena [48]. For example, consider the way that the daily cycle of light and darkness helps to entrain our sleep, body temperature, and other circadian rhythms to the world around us [53, 54, 55] . Like all mammals, each of us has a circadian pacemaker, a network of thousands of specialized clock cells located in the region of the hypothalamus known as the suprachiasmatic nuclei, just above where the optic nerves criss-cross as they make their way back to the brain. These cells have been shown experimentally to be intrinsically oscillatory [56] and their distribution of natural frequencies has been measured [57]. The pacemaker cells are also known to be mutually coupled, though their precise connectivity remains unclear. Thus, qualitatively at least, one could try to model the pacemaker cell network with the Kuramoto model. Now consider how this network might respond to an imposed cycle of

light and dark (information of this sort is known to be conveyed from the eyes to the pacemaker through a specialized neural pathway). If the light-dark cycle is 24 hours long, we expect the electrical rhythms of many individual pacemaker cells to successfully entrain to it. But what if we alter the period or strength of the external forcing, as has been done in countless experiments on mice, hamsters, primates, and human volunteers [53]? Or what happens if the experiment is conducted on mutant organisms [58, 59] whose intrinsic periods are a few hours longer or shorter than normal, or which may be intrinsically arrhythmic, having almost no free-running circadian rhythm at all?

Questions like this can be addressed, in mathematically idealized form, within the framework of the periodically forced Kuramoto model [60, 61, 62]. Its governing equations are given by

$$\frac{d\vartheta_i}{dt} = \omega_i + \frac{K}{N}\sum_{j=1}^{N}\sin(\vartheta_j - \vartheta_i) + F\sin(\sigma t - \vartheta_i), \tag{3.1}$$

for $i = 1, \ldots, N$. Here ϑ_i is the phase of oscillator i, ω_i is its natural frequency, K is the coupling strength, F is the forcing strength, σ is the forcing frequency, and $N \gg 1$ is the number of oscillators. The natural frequencies are randomly distributed with a density $g(\omega)$, assumed unimodal and symmetric about its mean value ω_0.

This system is capable of rich dynamics because of its interplay among randomness, coupling, and forcing. The randomness comes from the variance of the natural frequencies. This effect tends to desynchronize the oscillators and scatter their phases. The coupling, on the other hand, tends to align the oscillators to the same phase, although it does not favor any particular frequency for

the collective oscillation. In contrast, the forcing does favor a specific frequency, namely that of the external drive. Depending on the relative magnitudes of these competing effects, we expect to see various kinds of cooperative behavior and transitions between them.

Before continuing, it proves useful to simplify the governing equations in two ways. First, if we view the dynamics in a frame co-rotating with the drive, the explicit time dependence in (3.1) disappears. To achieve this, let

$$\theta_i = \vartheta_i - \sigma t. \tag{3.2}$$

Then (3.1) yields

$$\frac{d\theta_i}{dt} = (\omega_i - \sigma) + \frac{K}{N}\sum_{j=1}^{N} \sin(\theta_j - \theta_i) - F\sin\theta_i, \tag{3.3}$$

for $i = 1, \ldots, N$. Second, as Kuramoto originally pointed out, it is helpful to introduce a complex order parameter z, given by

$$z(t) = \frac{1}{N}\sum_{j=1}^{N} e^{i\theta_j(t)}. \tag{3.4}$$

Then the sum in (3.3) reduces to $\mathrm{Im}(Kze^{-i\theta_i})$, an identity which will prove useful later.

The order parameter also has a nice physical interpretation. Its amplitude $|z|$ quantifies the phase coherence of the population: an incoherent state has $z = 0$; a perfectly coherent state has $|z| = 1$. Furthermore, the argument of z can be interpreted as the average phase of all the oscillators. So in a sense, the single complex number $z(t)$ serves as a proxy for the state of the population as a whole.

Sakaguchi [60] was the first to study the periodically forced Kuramoto model. He derived a self-consistent equation for steady-state values of $|z|$, under

the assumption that $z(t)$ was entrained by the external force (meaning that $z(t)$ appeared motionless in the rotating frame). In numerical simulations of Equation (3.3), however, Sakaguchi found that this state of "forced entrainment" was not always attained. For some values of the parameters, the system could settle instead into a state of "mutual entrainment." In this case a macroscopic fraction of the system self-synchronized at a different frequency from that of the drive, indicating that this sub-population had broken away and established its own collective rhythm. (For circadian rhythms, this would mean that the animal's internal clock was drifting relative to the outside world.) Sakaguchi's numerics further indicated how forced entrainment could be lost and give way to mutual entrainment. Such transitions were found to occur via two different mechanisms, corresponding to a pair of distinct bifurcation curves in parameter space. These curves appeared to join at a point, but Sakaguchi was unable to resolve the details of the cross-over region numerically.

More recently, Antonsen et al. [61] gave an improved analytical treatment of the model. Their linear stability analysis and numerical simulations also revealed an intriguing set of bifurcation curves, but the way the various curves join together still remained unclear. The overall layout of the stability diagram suggested that an underlying two-dimensional system was controlling the dynamics—a remarkable finding, given that the model (3.3) is essentially infinite-dimensional (recall $N \gg 1$).

This tantalizing clue led Ott and Antonsen to an important discovery [62]. They found that the Kuramoto model possesses an invariant manifold, a special family of states for which the macroscopic dynamics becomes *low*-dimensional. In particular they showed that on this invariant manifold, the order param-

eter for the forced Kuramoto model (3.3) exactly satisfies a *two*-dimensional dynamical system, for the special case where the frequency distribution $g(\omega)$ is Lorentzian and the initial state satisfies certain strong analyticity properties with respect to ω.

In this paper we analyze the two-dimensional system derived from the analysis of Ott and Antonsen [62]. Our results give the first complete picture of the bifurcation structure for the forced Kuramoto model. We obtain explicit formulas for the system's saddle-node and Hopf bifurcation curves, as well as the codimension-2 Takens-Bogdanov point from which they emanate. Bifurcation theory predicts that a curve of homoclinic bifurcations should also emerge from the Takens-Bogdanov point; we compute this homoclinic curve numerically.

The rest of the paper is organized as follows. Section 2 reviews the approach of Ott and Antonsen [62], leading up to their derivation of the reduced equations for the order parameter dynamics. Section 3 presents new results about the bifurcations in this system and resolves the issue of how all the transition curves fit together. The final section discusses the implications of the results, their relation to prior work, the limitations of the approach used here, and some of the questions that remain.

3.2 Derivation of the reduced equations

The analysis of (3.3) is carried out in the continuum limit $N \to \infty$. Then the state of the system is described by a density function $f(\theta, \omega, t)$. Here f is defined such that at time t, the fraction of oscillators with phases between θ and $\theta + d\theta$ and

natural frequencies between ω and $\omega + d\omega$ is given by $f(\theta, \omega, t)\, d\theta\, d\omega$. Thus

$$\int_{-\infty}^{\infty} \int_{0}^{2\pi} f(\theta, \omega, t)\, d\theta\, d\omega = 1 \tag{3.5}$$

and

$$\int_{0}^{2\pi} f(\omega, \theta, t)\, d\theta = g(\omega), \tag{3.6}$$

by definition of $g(\omega)$.

The evolution of f is given by the continuity equation

$$\frac{\partial f}{\partial t} + \frac{\partial}{\partial \theta}(fv) = 0, \tag{3.7}$$

which expresses the conservation of oscillators of frequency ω. Here $v(\theta, \omega, t)$ is the velocity field on the circle corresponding to (3.3) as $N \to \infty$:

$$v(\theta, \omega, t) = (\omega - \sigma) + K \int_{-\infty}^{\infty} \int_{0}^{2\pi} \sin(\theta' - \theta)\, f(\theta', \omega', t)\, d\theta'\, d\omega' - F \sin\theta. \tag{3.8}$$

This expression can be written more compactly in terms of the complex order parameter z, which in the continuum limit becomes

$$z(t) = \int_{-\infty}^{\infty} \int_{0}^{2\pi} e^{i\theta} f(\theta, \omega, t)\, d\theta\, d\omega. \tag{3.9}$$

Using the identity mentioned in the Introduction (Section 3.1), we note that the double integral in (3.8) simplifies to $\mathrm{Im}(Kze^{-i\theta})$. Hence the continuity equation becomes

$$\frac{\partial f}{\partial t} + \frac{\partial}{\partial \theta}\left(f \left[(\omega - \sigma) + \frac{1}{2i} \left\{ (Kz + F)e^{-i\theta} - (Kz + F)^* e^{i\theta} \right\} \right] \right) = 0, \tag{3.10}$$

where the asterisk denotes complex conjugation.

Normally one would try to solve (3.10) by expanding f as a Fourier series in θ:

$$f(\theta, \omega, t) = \frac{g(\omega)}{2\pi} \left[1 + \sum_{n=1}^{\infty} f_n(\omega, t) e^{in\theta} + \text{c.c.} \right], \tag{3.11}$$

where c.c. denotes complex conjugate. Substitution of (3.11) into (3.9) and (3.10) would generate an infinite set of coupled nonlinear ordinary differential equations for the amplitudes $f_n(\omega, t)$. Unfortunately the dynamics of this infinite-dimensional system would likely be difficult to analyze further.

It was at this point that Ott and Antonsen [62] noticed something wonderful. They restricted attention to the special family of densities f for which

$$f_n(\omega, t) = [\alpha(\omega, t)]^n , \tag{3.12}$$

for all $n \geq 1$. In other words, they assumed that all the amplitudes f_n are n^{th} powers of the *same* function $\alpha(\omega, t)$. Amazingly, this ansatz satisfies the amplitude equations for all n, so long as α evolves according to

$$\frac{d\alpha}{dt} = \frac{1}{2}(Kz + F)^* - i(\omega - \sigma)\alpha - \frac{1}{2}(Kz + F)\alpha^2 \tag{3.13}$$

and z satisfies

$$z(t) = \int_{-\infty}^{\infty} \alpha^*(\omega, t)\, g(\omega)\, d\omega. \tag{3.14}$$

Then, by further assuming that $g(\omega)$ is a Lorentzian,

$$g(\omega) = \frac{\Delta}{\pi\{(\omega - \omega_0)^2 + \Delta^2\}}, \tag{3.15}$$

and that $\alpha(\omega, t)$ satisfies certain analyticity conditions in the complex ω-plane, Ott and Antonsen [62] evaluated (3.14) by contour integration and thereby derived the following exact evolution equation for the order parameter z:

$$\frac{dz}{dt} = \frac{1}{2}\left[(Kz + F) - (Kz + F)^* z^2\right] - [\Delta + i(\sigma - \omega_0)]\, z. \tag{3.16}$$

The conditions required were that $\alpha(\omega, t)$ can be analytically continued from the real ω-axis into the lower half of the complex ω-plane for all $t \geq 0$; that $|\alpha(\omega, t)| \to 0$ as $\text{Im}(\omega) \to -\infty$; and that $|\alpha(\omega, 0)| \leq 1$ for real ω.

3.3 Analysis of the reduced equations

3.3.1 Scaling the equations

We turn now to the analysis of the two-dimensional system (3.16). The first step is to reduce the number of parameters by nondimensionalizing the system. Let $\hat{t} = \Delta t, \hat{F} = F/\Delta, \hat{K} = K/\Delta, \hat{\sigma} = \sigma/\Delta$ and $\hat{\omega}_0 = \omega_0/\Delta$. Then the form of (3.16) stays the same except that Δ no longer appears (in effect, Δ has been set to 1 without loss of generality) and all the other parameters now have hats over them. For ease of notation we drop the hats in what follows, remembering that all the parameters are now dimensionless. Also, let

$$\Omega = \sigma - \omega_0 \tag{3.17}$$

denote the (dimensionless) detuning between the drive frequency and the population's mean natural frequency. Then if we introduce polar coordinates

$$z = \rho e^{i\phi} \tag{3.18}$$

and separate (3.16) into real and imaginary parts, we obtain the dimensionless evolution equations for ρ and ϕ:

$$\rho' = \frac{K}{2}\rho(1-\rho^2) - \rho + \frac{F}{2}(1-\rho^2)\cos\phi \tag{3.19}$$

$$\phi' = -\left[\Omega + \frac{F}{2}\left(\rho + \frac{1}{\rho}\right)\sin\phi\right] \tag{3.20}$$

where the prime denotes differentiation with respect to dimensionless time.

3.3.2 Stability diagram and phase portraits

Our next goal is to obtain the stability diagram for Equations (3.19)-(3.20). Before delving into the details, which can become intricate at times, we jump to the final result. Figure 3.1 shows the stability diagram for the representative case where $K = 5$. Here the various stability regions labeled A-E correspond to the phase portraits shown in Figure 3.2.

We realize that these figures appear complicated at first glance, so let us begin by offering a few general remarks about them. Figure 3.1 is divided into five regions, A-E, by the bifurcation curves labeled saddle-node, Hopf, homoclinic, and SNIPER. In the places where two or more of these curves nearly coincide, Figure 3.1(a) becomes especially confusing. To clarify what is going on in such regions, Figures 3.1(b) and 3.1(c) zoom in near two codimension-2 points of interest (to be discussed in detail later). Since even these figures can be hard to interpret, we have tried to make everything as clear as possible by presenting a schematic Figure 3.1(d). Unlike Figures 3.1(a)-(c), which are numerically accurate, Figure 3.1(d) is only topologically correct. We have distorted some of stability regions and pulled certain curves apart to make the layout of the diagram transparent, and to highlight the three different codimension-2 points that will later be seen to organize the entire diagram.

A similar but incomplete version of Figure 3.1 was obtained previously by Antonsen et al. [61]; see Figure 3 in their paper. Those authors generated their results based on direct simulations of Equation (3.3) for $N = 1000$ oscillators. They also compared their numerics to analytical results they derived for the existence and stability of equilibrium points for (3.3), which correspond to entrained states in the original frame. Our approach, in contrast, is to analyze the

reduced system Equations (3.19)-(3.20). We do not present numerical results for the full system (3.3) because in every case we have checked, our results match those reported already by Antonsen et al. [61], except in cases where the previous methods were inconclusive.

3.3.3 Saddle-node and SNIPER bifurcations

It is algebraically awkward to solve for the fixed points of Equations (3.19)-(3.20) in terms of the parameters. Fortunately, we do not need to solve for them. Since we are mainly interested in the bifurcation curves, we can make headway more easily by imposing an appropriate bifurcation condition and then solving for the parameters in terms of the fixed point, rather than the other way around. This is a standard trick in bifurcation theory, and it allows us to derive the bifurcation curves in closed form, either explicitly or as parametric equations.

For example, at a saddle-node bifurcation, one of the eigenvalues equals 0 and hence the determinant of the Jacobian vanishes there. (The same would be true at transcritical or pitchfork bifurcations, but given the absence of the constraints or symmetries associated with these types of bifurcations, there's no reason to expect either of them to occur here.)

Hence to find the locus of saddle-node bifurcations, we solve $\rho' = 0$, $\phi' = 0$ and $\delta = 0$ simultaneously, where δ denotes the determinant of the Jacobian. The trick is to regard the unknown values of the variables ρ and ϕ on equal footing with the parameters K, Ω and F. Then the resulting system of 3 equations in 5 unknowns can be solved explicitly to yield a parametrization of the saddle-node bifurcation surface. Various parameterizations are possible. One convenient

Figure 3.1: Bifurcation Diagram of Forced Kuramoto Model

Stability diagram for the forced Kuramoto model. Bifurcation curves are shown with respect to the strength F and detuning Ω of the external forcing, both of which have been non-dimensionalized by the width Δ of the distribution of the oscillators' natural frequencies. The dimensionless coupling strength is fixed at $K = 5$.

(a) Regions A-E correspond to qualitatively different phase portraits; see text and Figure 3.2 for explanations. Four types of bifurcations occur: supercritical Hopf bifurcation; homoclinic bifurcation; and two types of saddle-node bifurcations. The saddle-node bifurcations on the upper branch, and also those on the lower branch between the cusp and the saddle-node-loop point, are purely local. In contrast, those on the portion of the lower branch extending from the origin to the saddle-node-loop point have global consequences; they are saddle-node infinite-period bifurcations, or SNIPERs, which create or destroy limit cycles. The filled circle marks a codimension-2 Takens-Bogdanov point, at which the Hopf, homoclinic, and upper saddle-node curve intersect tangentially.

(b) Enlargement of the cross-over region, just to the right of the Takens-Bogdanov point, where all four bifurcation curves run nearly parallel to one another. Three of them (Hopf, SNIPER, and the lower branch of saddle-node bifurcations) meet at a codimension-2 saddle-node-loop point, marked by a filled diamond.

(c) Enlargement of the region near the codimension-2 cusp point (filled square), where the upper and lower branches of saddle-node bifurcations meet tangentially. The two branches are almost indistinguishable in this image.

(d) Schematic version of the stability diagram, intended to show how the bifurcation curves connect in the confusing cross-over region. Tangential intersections have been opened up for clarity.

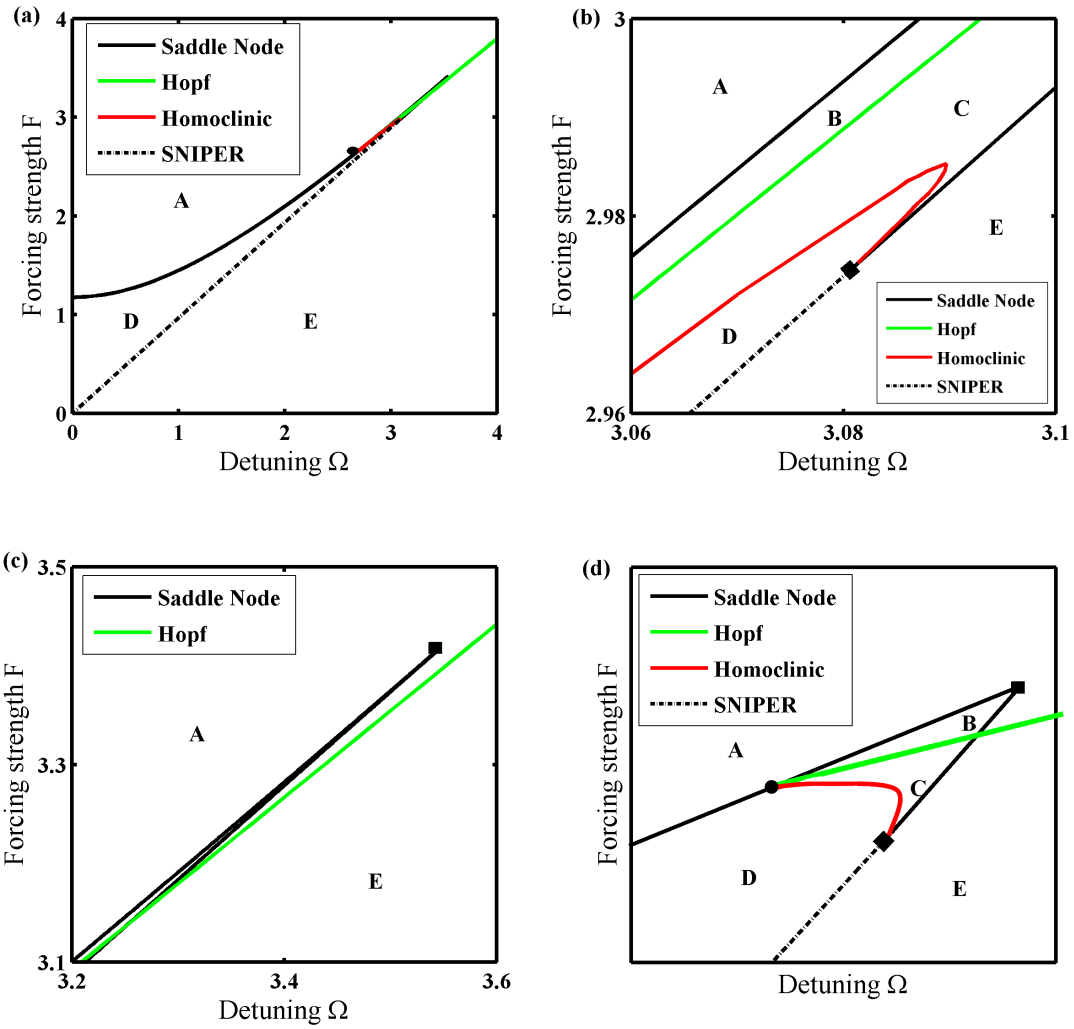
(a)
Saddle Node
Hopf
Homoclinic
SNIPER
A
D
E
Forcing strength F
Detuning Ω
0
1
2
3
4
(b)
A
B
C
D
E
2.96
2.98
3
3.06
3.08
3.1
(c)
3.1
3.3
3.5
3.2
3.4
3.6
(d)

Figure 3.2: Phase Portraits

Phase portraits for the two-dimensional dynamics of the complex order parameter z, or equivalently, for the variables ρ, ϕ regarded as polar coordinates. Open dots, unstable fixed points. Closed dots, stable fixed points. Asterisk, origin of the z-plane. Dashed curves, stable and unstable manifolds of the saddle point. The panels are not all shown at the same scale; the regions shown in (b) and (c) are small and have been blown up here for clarity.

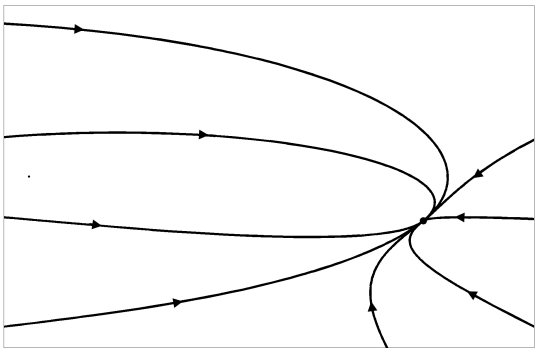

(a) Region A

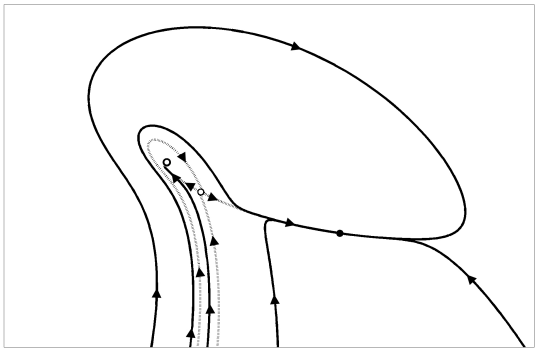

(b) Region B

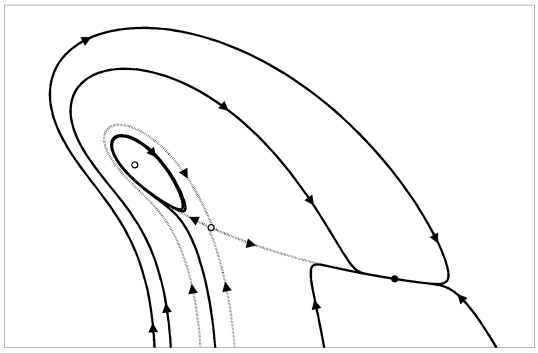

(c) Region C

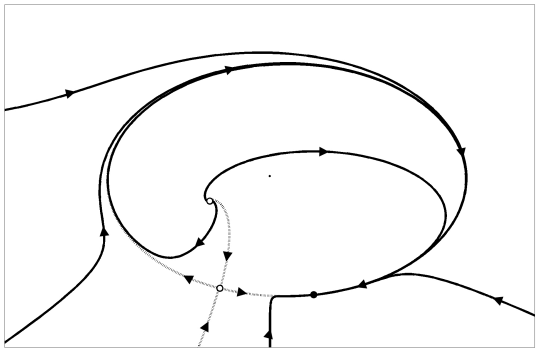

(d) Region D

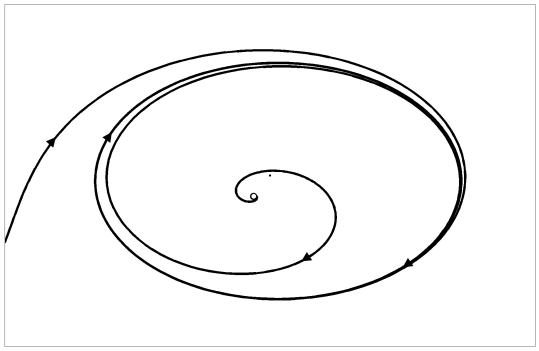

(e) Region E

choice is to express the parameters in terms of the fixed-point values of ρ and ϕ. We find that the saddle-node surface is then given by

$$K = \frac{2\left(\rho^4 + 2\rho^2 \cos 2\phi + 1\right)}{(1-\rho^2)^2 (1+\rho^2 \cos 2\phi)} \tag{3.21}$$

$$\Omega = \frac{\left(\rho^3 + \rho\right)^2 \sin 2\phi}{(1-\rho^2)^2 (1+\rho^2 \cos 2\phi)} \tag{3.22}$$

$$F = -\frac{4\rho^3\left(\rho^2+1\right)\cos\phi}{(1-\rho^2)^2 (1+\rho^2 \cos 2\phi)} \tag{3.23}$$

where we allow ρ and ϕ to sweep over their full ranges $0 \le \rho \le 1$, $-\pi \le \phi \le \pi$.

This parametrization provides some interesting information. For instance, it shows that K increases monotonically with ρ, for each fixed value of ϕ. Hence $K \ge 2$ everywhere on the saddle-node surface, with the minimum value $K = 2$ being attained when $\rho = 0$ and hence $F = 0$, or in other words, when there is no forcing. This result makes sense. In the absence of forcing, the system is just the traditional Kuramoto model with a Lorentzian $g(\omega)$, and $K = 2\Delta$ (or in dimensionless terms, $K = 2$) is the well-known formula for the critical coupling at the onset of mutual synchronization [41, 42].

To compare our results with those obtained numerically by Antonsen et al. [61], it is more illuminating to slice through the saddle-node surface at a fixed value of $K > 2$ and then plot the resulting saddle-node curves in the (Ω, F) plane. To find these curves we solve $\rho' = 0$, $\phi' = 0$ and $\delta = 0$ for $\Omega, \sin\phi$ and $\cos\phi$, and then use $\sin^2\phi + \cos^2\phi = 1$ to solve for F, now regarding K and ρ as parameters. The result is the following parametrization of the saddle-node curve:

$$\Omega_{SN} = \frac{\left(\rho^2+1\right)^{3/2}\sqrt{K\left(\rho^2-1\right)\left(K\left(\rho^2-1\right)^2-4\right)-4\left(\rho^2+1\right)}}{2\left(\rho^2-1\right)^2} \tag{3.24}$$

$$F_{SN} = \frac{\sqrt{2}\rho^2\sqrt{K^2\left(\rho^2-1\right)^3+2K\left(\rho^4-4\rho^2+3\right)-8}}{\left(\rho^2-1\right)^2}. \tag{3.25}$$

Figure 3.1 plots this saddle-node curve for the case $K = 5$, as previously studied by Antonsen et al. [62]. We compute the curve for all values $0 < \rho < 1$, disregarding any values that yield non-real results for Ω or F.

The two branches of the saddle-node curve intersect tangentially at a codimension-2 cusp point, as highlighted in Figure 3.1(c) and marked schematically in Figure 3.1(d) by the solid square . For $K = 5$, the parameter values at the cusp are $\Omega \approx 3.5445$ and $F \approx 3.4164$.

Along with local saddle-node bifurcations, the lower branch of the saddle-node curve(where $F \approx \Omega$) also includes a large section consisting of saddle-node infinite-period (SNIPER) bifurcations. These have important global implications, because they create or destroy limit cycles in the phase portrait of Equations(3.19)-(3.20).

3.3.4 Hopf bifurcation

Next we calculate the locus of parameter values at which Hopf bifurcations occur. We impose the fixed point conditions $\phi' = 0$, $\rho' = 0$ as before, but now require that the Jacobian has zero trace and positive determinant—the latter two conditions are equivalent to requiring that the eigenvalues be pure imaginary.

Solving simultaneously for $\phi' = 0$, $\rho' = 0$ and trace = 0, we find

$$\sin\phi = -\frac{\left(K^2-4\right)\Omega}{F\sqrt{K-2}K\sqrt{K+2}} \tag{3.26}$$

$$\cos\phi = -\frac{(K-2)^{3/2}}{2F\sqrt{K+2}} \tag{3.27}$$

$$\rho = \sqrt{\frac{K-2}{K+2}}. \tag{3.28}$$

Because ρ depends only on K, we can go a bit further than we did in the saddle-node case. Using $\sin^2\phi + \cos^2\phi = 1$ as before, F can now be obtained *explicitly* in terms of K and Ω:

$$F_{\text{Hopf}} = \frac{1}{2K}\sqrt{\frac{(K-2)\left(K^4 - 4K^3 + 4\left(\Omega^2+1\right)K^2 + 16\Omega^2 K + 16\Omega^2\right)}{K+2}} \tag{3.29}$$

For the special case $K = 5$ studied by Antonsen et al. [62], Equation (3.29) becomes

$$F_{\text{Hopf}} = \frac{1}{10}\sqrt{\frac{3}{7}}\sqrt{225 + 196\Omega^2} \tag{3.30}$$

Figure 3.1 plots the graph of $F_{\text{Hopf}}(\Omega)$. Notice how straight it is, and that it nearly lines up with the lower branch of the saddle-node curve.

3.3.5 Takens-Bogdanov point

As mentioned above, for Equation (3.29) to truly signify a Hopf bifurcation, the Jacobian determinant must be positive at the corresponding parameter values (Ω, F) . This will be the case if Ω and F are sufficiently large. Specifically, their values must exceed those at the Takens-Bogdanov point

$$\Omega_{\text{TB}} = \frac{(K-2)K^2}{4(K+2)} \tag{3.31}$$

$$F_{\text{TB}} = \frac{1}{4}(K-2)\sqrt{\frac{K^3 - 2K^2 + 4K - 8}{K+2}} \tag{3.32}$$

obtained by solving four simultaneous equations: $\phi' = 0$, $\rho' = 0$, trace = 0, and determinant = 0.

The Takens-Bogdanov point is marked with a filled circle on Figures 3.1(a) and 3.1(d). In addition to serving as the endpoint of the Hopf curve, it splits the upper branch of the saddle-node curve into two sections of different dynamical

character. On the lower section (below the Takens-Bogartian point), an *unstable* node collides with a saddle along the saddle-node bifurcation curve; this can be seen by comparing regions D and A, as shown in Figures 3.2(d) and 3.2(a). The opposite situation occurs on the upper section of the saddle-node curve, above the Takens-Bogartian point. Here a *stable* node collides with a saddle, corresponding to the transition between regions B and A; see Figures 3.2(b) and 3.2(a).

3.3.6 Homoclinic bifurcation

The theory of the Takens-Bogdanov bifurcation implies that a curve of homoclinic bifurcations must also emerge from the codimension-2 point, tangential to the saddle-node and Hopf curves. For the case $K = 5$ shown in Figure 3.1, $\Omega_{\mathrm{TB}} = \frac{75}{28}$ and $F_{\mathrm{TB}} = \frac{3}{4}\sqrt{\frac{87}{7}}$. The curve shown in the diagram was computed numerically. It is almost indistinguishable from the Hopf curve and thus produces a very small region between them, as shown in Figure 3.1(b).

A striking feature of the homoclinic curve is that after moving parallel to the Hopf curve for a while, it makes a sharp backward turn and then joins onto the lower branch of the saddle-node/SNIPER curve, meeting that curve tangentially at a codimension-2 "saddle-node-loop" point [63, 64] marked by a filled diamond in Figures 3.1(b) and 3.1(d).

3.3.7 Phase portraits and bifurcation scenarios

As we have seen, the bifurcation curves in Figure 3.1 partition the stability diagram into five regions, labeled A-E. We now give a fuller treatment of the dynamics associated with each region and the transitions from one to another.

Region A: Forced entrainment

Here the order parameter z approaches a stable fixed point for all initial conditions, as shown in Figure 3.2(a). To interpret what this means, recall that all our analysis has assumed a frame co-rotating with the drive. Hence this stable fixed point represents a state in which the order parameter is moving periodically while staying phase-locked to the drive. Therefore, back in the original frame, a macroscopic fraction of the oscillator population must also be moving in rigid synchrony, locked to the same frequency as the drive signal.

Region B: Bistability between two states of forced entrainment

Now suppose we weaken the forcing. Imagine moving down along a vertical line in Figure 3.1(b), decreasing F while holding Ω fixed. As we do so, we first pass from region A into the extremely narrow region B by crossing through the upper branch of the saddle-node curve (3.24). At this bifurcation, a stable node is born out of the vacuum, along with a saddle point. Meanwhile, the stable fixed point that we encountered in Region A still exists; it lies in the lower right part of Figure 3.2(b).

Thus Region B depicts a form of bistability. Depending on the initial con-

ditions, the system chooses one of two possible states of forced entrainment, differing in their phase coherence (the magnitude of z) and their phase relationship to the drive signal (the argument of z).

Region C: Bistability between forced entrainment and phase trapping

Continuing our vertical descent through Figure 3.1(b), we next cross from B into C by passing through the curve of Hopf bifurcations, Equation (3.29). The stable fixed point created in Region B now loses stability and gives birth to a tiny attracting limit cycle (Figure 3.2(c)). On this cycle the order parameter still runs at the same average frequency as the drive but its relative phase and amplitude now wobble slightly. Because these variations remain trapped within tight limits, one says the system is phase trapped (as opposed to phase locked) to the drive. Back in the original non-rotating frame, the macroscopic dynamics for this state would be quasiperiodic with two frequencies. This is not the only attractor, of course; the state of forced entrainment seen earlier in A and B persists, so we still have bistability, but now between phase trapping and forced entrainment.

Region D: Forced entrainment

Passing from Region C to D carries us across a curve of homoclinic bifurcations. As we approach this curve from above, the tiny limit cycle in Figure 3.2(c) expands. At the bifurcation it touches the saddle point and forms a homoclinic orbit. Beyond the bifurcation the phase portrait looks like that shown in Figure 3.2(d). An invariant loop has been created, in which the saddle and the original

stable node are now connected by both branches of the saddle's unstable manifold. The stable node is the unique attractor. Hence the system again falls into a state of forced entrainment.

Region E: Mutual entrainment

Forced entrainment is finally lost when we pass from Region D to E. When crossing the lower branch of the saddle-node curve, we need to be careful to specify exactly where the crossing occurs. Specifically, do we cross to the left or right of the codimension-2 saddle-node-loop point (filled diamond in Figure 3.1(b)) at which the homoclinic curve meets the saddle-node curve?

Suppose first that we cross below and to the left of the saddle-node-loop point. Then in Figure 3.2(d) the saddle and node would slide toward each other along the invariant loop, coalesce, and disappear, leaving a stable limit cycle in their wake. Thus, this saddle-node bifurcation is actually a SNIPER (saddle-node infinite-period) bifurcation.

The limit cycle created by the bifurcation is globally attracting. Hence the order parameter always settles into periodic motion in the rotating frame. But unlike the limit cycle of Figure 3.2(b) this cycle winds around the origin of the z-plane, marked by an asterisk in Figure 3.2(d). This is an important distinction, because it implies that the phase of z now increases monotonically relative to that of the drive. Consequently the order parameter $z(t)$ oscillates at a different average frequency from the drive signal, implying that a macroscopic fraction of the oscillator population has broken loose from the drive. In other words, the system has spontaneously mutually entrained itself, at least in part. This is

therefore one mechanism by which forced entrainment can give way to mutual entrainment.

But there are other possible mechanisms as well. For example, consider Figure 3.1(b) again, and now direct your attention to the upper right corner. By moving down along the right side of the picture, we can cross directly from C to E, without ever going through D. This happens when we cross through the portion of the lower saddle-node curve lying above and to the right of the saddle-node-loop point. In this case the bifurcation is not a SNIPER; it's just an ordinary saddle-node bifurcation. To visualize this scenario, imagine sliding the saddle in the middle of Figure 3.2(c) to the right along its unstable manifold until it collides with the node and annihilates it. During this process the limit cycle in Figure 3.2(c) grows. And so the phase portrait now resembles the one shown in Figure 3.2(e).

A third scenario is much simpler. Suppose $\Omega > \Omega_{\text{cusp}}$, so that we're well to the right of the cusp in Figures 3.1(c) and 3.1(d). Then as we decrease F, we move directly from A to E. Forced entrainment gives way to mutual entrainment through a supercritical Hopf bifurcation.

3.4 Discussion

3.4.1 Stability diagram

The main result of the paper is the stability diagram shown in Figure 3.1. We have focused on the analytical derivation of several of the curves in this picture

and tried to clarify how they fit together and what they imply about the system's overall dynamics. Having immersed ourselves in the details, it is worthwhile to step back and try to understand the broader lessons that this picture holds.

Figure 3.1 essentially divides into two big regions. One represents forced entrainment, wherein a macroscopic fraction of the population is phase-locked to the drive. The rest of the population consists of oscillators belonging to the infinite tails of the frequency distribution; these remain unlocked. Thus it would be more accurate to speak of "partial forced entrainment," though we hope the intended meaning of the shorter name is clear.

The other main region represents (partial) mutual entrainment. Now there are three qualitatively different groups of oscillators: (1) the unlocked oscillators in the tails; (2) the oscillators entrained by the forcing; and (3) a self-organizing group of oscillators that entrain one another at a frequency different from that of the drive. The existence of this third group causes the order parameter to wobble or drift periodically relative to the drive, as manifested by a stable limit cycle in the phase portraits (Figures 3.2 (c) and 3.2(e)).

3.4.2 Comparison to Adler equation

The boundary between forced and mutual entrainment is complicated when viewed at a fine scale, as shown in Figure 3.1(b). But from a bird's-eye view, it looks very much like the straight line $F = \Omega$. Here's why: this is the result one would expect from the Adler equation

$$\phi' = -\Omega - F \sin \phi, \tag{3.33}$$

which has been used to model the entrainment dynamics of phase-locked loops [65], lasers [66, 67], and fireflies [68], among many other systems. The two-dimensional system (3.19)-(3.20) reduces to Adler's equation as $K \to \infty$, in the sense that ρ approaches 1 on a fast time scale, while ϕ obeys (3.33) on a slow time scale.

The intuitive explanation is that in this limit, the coupling between oscillators is so strong that the population acts like one giant oscillator, with nearly all the microscopic oscillators at the same phase. Hence the order parameter amplitude remains close to $\rho = 1$ at all times, so the system behaves as if it had a very strongly attracting limit cycle. This explains why the dynamics of the forced Kuramoto model mimic the Adler equation in this limit.

For a more analytical route to the same conclusion, look at the large-K behavior of the Takens-Bogdanov point, which essentially lies on the dividing line behind the two big regions. The formulas (3.31)-(3.32) imply that

$$\frac{F_{\mathrm{TB}}}{\Omega_{\mathrm{TB}}} \sim 1 - 8K^{-4} \tag{3.34}$$

as $K \to \infty$. Thus $F \approx \Omega$ for large and even moderate values of K.

3.4.3 Comparison to forced van der Pol equation

For weaker coupling, but still large enough that the system can partially self-synchronize ($2 < K < \infty$), the population again acts like a single limit cycle oscillator, but now with a limit cycle that is only weakly attracting. As before, the complex order parameter plays the role of this effective limit-cycle oscillator.

So when forcing is applied, we expect the overall dynamics to be like those

of a forced, weakly nonlinear oscillator. And indeed, the stability diagram bears a striking resemblance to that of a forced van der Pol oscillator, in the limit of weak nonlinearity, weak detuning, and weak forcing. As in the problem studied here, the stability diagram for this well-studied system [69] is also organized around a Takens-Bogdanov bifurcation and a saddle-node-loop bifurcation.

Likewise, some of the regions in the van der Pol diagram are unusually thin and small. This helps to explain why they were overlooked for decades, until the theory of the Takens-Bogdanov bifurcation was developed and guided later researchers to the missing transitions that, on topological grounds, had to be there.

One always expects small regions in systems with Takens-Bogdanov bifurcations because, according to normal form theory, the saddle-node, Hopf, and homoclinic curves have to intersect *tangentially* at the Takens-Bogdanov point. But here, as in the van der Pol problem, the regions are even smaller still, because they must also hug the line $F \approx \Omega$, for the reasons given above.

3.4.4 Caveats

It is important to understand what has—and has not—been shown by the analysis presented in this paper. Following Ott and Antonsen [62], we made a number of very particular choices in the course of reducing an infinite-dimensional problem to a two-dimensional one. We chose a special family of initial states (see Equation (3.12)) and showed that they formed an invariant manifold. In other words, if the condition (3.12) is satisfied initially, it is automatically satisfied for all time. Then we chose a special distribution of natural frequencies

(see Equation (3.15)), and required further that the initial state satisfies certain strong analyticity properties with respect to its dependence on these frequencies. Taken together, these choices then implied that the system's order parameter evolves according to the two-dimensional dynamical system (3.16).

If the conclusions that followed were sensitive to these choices, we would not have accomplished much. But there is reason to believe that the results are robust, and largely independent of these choices. The strongest evidence is numerical. Every time we have run simulations of the forced Kuramoto model (3.1) for hundreds or thousands of oscillators, we have seen all the attractors and bifurcations predicted by the analysis, where they are supposed to be. Ott and Antonsen [62] found similar agreement when they studied other variants of the Kuramoto model.

This suggests that the flow on the invariant manifold faithfully captures the macroscopic dynamics of the full system, at least in some sense. Unfortunately, we do not know how to make this statement precise. The issue is probably subtle. We do not believe, for example, that the invariant manifold is everywhere transversely attracting—it certainly isn't in other problems we have studied. For example, applying the method of Ott and Antonsen [62] to the Kuramoto model with a bimodal frequency distribution, we found that the invariant manifold in that case could be transversely *repelling* at certain points [70].

Nor are we sure whether all the attractors for the full system lie within the invariant manifold. If they did, that would explain why this manifold controls the system's long-term macroscopic dynamics. But we have no proof of this weaker statement either.

Now regarding the choice of a Lorentzian frequency distribution: this was crucial to the analysis, but not, we suspect, to the results. Sakaguchi [60] used a Gaussian $g(\omega)$ and found the same attractors and bifurcations as we did. Our own simulations for the Gaussian case (unpublished) show that the stability diagram is different in numerical details, of course, but its topology is unaffected.

On the other hand, the algebraic form of the forced Kuramoto model, with its purely sinusoidal coupling and driving, probably *is* crucial. The ansatz (3.12) no longer works if the model contains higher harmonics. Indeed, the bifurcation behavior of the classical (unforced) Kuramoto model is known to be altered when generic periodic functions are used in place of a pure sine function in the coupling [71, 72]. So we expect new phenomena to arise in the forced Kuramoto model as well, when one departs from pure sinusoids in the driving and coupling terms.

CHAPTER 4

UNDERSTANDING CONSENSUS DECISION MAKING IN ANIMAL GROUPS

4.1 Introduction

Collective behavior is seen all around us – from flocks of birds flying in the sky, to herds of wildebeests migrating across the plains of Africa to ants trailing food from picnics. For many years it was thought that coherent motion exhibited by these groups was the result of individuals following a knowledgeable leader. Recent computational and experimental studies, however, have shown that collective behavior can emerge from purely local interactions among individuals [73, 74, 75].

4.1.1 Collective Behavior in Animal Groups

There are many benefits for individuals to be associated with a group including avoidance of predation, increased access to food, increased efficiency of movement and increased social interaction [75, 76].

Association with a group allows individuals to avoid predation. For animals in large groups, the movement of many individuals can make it difficult for the predator to focus on any particular individual. Often such animals are covered with patterns. For example the stripes on zebras make it difficult for a lion to identify and attack an individual zebra. Additionally, being part of a group creates more ways for an individual to avoid an approaching predator. Individ-

uals in fish schools escape from predators simply by following the movement of neighbors and not because they know of the existence of a predator [77, 78].

Groups are better able to find food sources because many individuals can contribute to searching. Thus, even if some individuals fail to find food, the group does not starve. Ant colonies send out many individuals to search for food and the ones that are successful start pheromone trails to lead other ants to the same food source [73, 74, 78, 76].

Being part of a group can make movement easier, particularly in times when the fluid through which the group is moving creates significant resistance. Geese flying in V formation is a common sight and one that allows a drafting of sorts for the animals behind. Similarly fish in the back of schools feel less resistance moving through the water [75, 76].

Finally, there are social benefits to individuals in groups. With a large collection of individuals together, finding a mate is easier. Additionally, it has been shown that being part of a group can reduce the load of stress on any one individual [75, 76].

Although animals clearly get some benefit to being part of a group, the evolution of collective behaviors through natural selection is puzzling. It is generally accepted that evolutionarily speaking individuals maximize their fitness at the expense of other individuals. This is in direct contradiction to their involvement in groups which often lowers their individual fitness [75, 76].

4.1.2 Modeling Collective Animal Behavior

The modeling of collective behavior in animal groups has been approached with a variety of mathematical techniques including PDEs, equation-free models and self-propelled particle models.

PDEs

In PDE models of swarms, the group is typically described by a continuum density $\rho(\vec{x}, t)$ where x refers to the "individuals". The PDE takes the form $\rho_t + (\rho v)_x = 0$ where v refers to the convolution term [79, 80, 81]. A common assumption is the interactions between individuals take place in a pairwise fashion. In groups, individuals are interacting with many individuals, and the assumption is that the pairwise interactions can be combined by a superposition. With such assumptions social forces can be modeled as:

$$v = \int f_s(\vec{x} - \vec{y})\rho(\vec{y}, t)d\vec{y}$$

where f_s is a kernel describing the social influence on $\vec{x}$ from $\vec{y}$. The dynamics of the model are determined not only by social forces included but also by the form of the kernel [82].

Self-propelled Particle Models

Many existing models of collective behavior consist of a group of individuals governed by rules of interaction [83, 84, 85, 86, 87, 88]. In such models, individuals move towards the perception of where the group is (attraction) but move

away from other individuals whom are too close (repulsion) to avoid collision. More sophisticated models incorporate alignment of individuals with the orientation of nearby individuals [89].

One seminal model of this type was proposed by Couzin, Krause, Franks and Levin [90]. In this model, each individual was surrounded by three circular zones of different radii. The zone with the smallest radius corresponded to repulsion where individuals moved away to avoid collision. The intermediate zone corresponded to a zone of alignment where individuals attempted to display coordinated motion with nearby individuals. The largest zone corresponded to one of attraction to nearby individuals.

These rules were transcribed into a simple model as follows:

$$d_i(t + \Delta t) = \sum_{j \neq i} \frac{c_j(t + \Delta t) - c_i(t)}{|c_j(t + \Delta t) - c_i(t)|} + \sum_j \frac{v_j(t)}{|v_j(t)|} \tag{4.1}$$

where $c_i(t)$ denotes the individual's location in space, $v_i(t)$ denotes the individual's velocity and $\frac{d_i(t)}{|d_i(t)|}$ denotes the individual's desired direction. This model solely describes social interactions of repulsion, attraction and alignment amongst individuals. This simple mathematical model was shown to reproduce various behaviors of groups of individuals that have been observed in nature, such as polarized group motion (all individuals moving together in the same direction) and rotational group states (all individuals swirling in a torus) [91, 92].

Conflicting Information within Groups

The model described in Equation (4.1) assumes that all individuals have identical intrinsic properties and act identically to the same information. This is

not the case in the real world. Different individuals are privy to varying levels of information. For example, considering foraging strategies, some individuals may know the location of food, while others have no such knowledge. Within the group, however, it is not clear to individuals who has information and who does not.

An extension of the model described in Equation (4.1) added a preferred direction to a subset of individuals [90].

$$\begin{aligned} \hat{d}_i(t+\Delta t) &= \sum_{j\neq i} \frac{c_j(t+\Delta t) - c_i(t)}{|c_j(t+\Delta t) - c_i(t)|} + \sum_j \frac{v_j(t)}{|v_j(t)|} \\ d_i(t+\Delta t) &= \frac{\hat{d}_i(t+\Delta t) + \omega g_i}{|\hat{d}_i(t+\Delta t) + \omega g_i|} \end{aligned} \tag{4.2}$$

where $c_i(t)$ denotes the individual's location in space, $v_i(t)$ denotes the individual's velocity and $\frac{d_i(t)}{|d_i(t)|}$ denotes the individual's desired direction just as in Equation (4.1). In Equation (4.2), ω is a weighting term balancing the importance of social interactions with the influence of the preferred direction, $g_i(t)$. Only informed individuals have a non-zero preferred direction; uninformed individuals have a preferred direction vector equal to zero. We refer to these uninformed individuals as *naive*.

From the Couzin et al. [90] model, it was found that only a small proportion of individuals (5–10% depending on total group size) was needed to effectively move the population in a desired direction. Further, the group obtained directed collective motion without directly transferring information between individuals. Naive individuals did not gain any information.

This work was extended by Couzin et al. [90] by examining populations with multiple subpopulations exhibiting different and potentially conflicting information. Assuming the group preferred to stay together, as is often the case biologically, it was found that if the two informed subpopulations each comprised half the population, the group would go to the average of the two opinions and go to neither preferred direction [90, 93, 94]. Clearly this is unproductive for the group, as well as biologically unrealistic. For example, when two groups of fish know two different locations for food, in reality the group ends up going to one of those two location, not to neither location as the model predicts. This would be equivalent to everyone losing out.

If naive individuals with no desired direction of travel, however, are added to the group, the group no longer always goes to the average of the opinions of the informed individuals. Instead, if the difference of opinion between informed subpopulations is large enough, the population chooses to go to one of the desired directions with equal probability, assuming equally sized informed subpopulations. That is, with a large difference in preferred direction and in the presence of naives, the fish make it to one of the food locations. Further, it has been shown that an increased number of naive individuals makes this group "decision" occur earlier and with more accuracy up to some limit [90]. In other words, a group with a significant percentage of uninformed individuals is actually more effective, both in accuracy and expediency, at reaching the desired location.

Trap-lining

For certain values of ω the relation between attraction to the desired direction and attraction to the group yielded results where the groups oscillated between the two desired locations [95]. This phenomenon is known as trap-lining because the individuals continually revisit various locations of interest, just as trappers repeatedly check their traps. In this example the individuals are trapped on a line between two positions or food sources.

Trap-lining occurs when a group with a subset of individuals attracted to a particular location reach that location. Because they are at their desired location, the desire of that subset to move in any particular direction is zero. However, the other subset that is far from their desired location strongly wants to return there, overpowering the now complacent subset. Thus, the entire group begins to move towards the opposite desired location and the process is repeated.

As the dynamics of trap lining are occurring in one spatial dimension, we reduce the system from two to one spatial dimensions and examine the dynamics.

4.1.3 Organization

In this chapter, we investigate several models to describe a population of organisms with subgroups containing conflicting information. Biologically, the goal is for the group to make a productive consensus decision. A 'productive' decision is one that gets the individuals to one of the desired directions. Here

a desired direction can be thought to lead to a food source. A 'consensus' decision means the group does not split apart. Recall, we are assuming we are dealing with organisms that need to stay as a single large group to survive. Our results show the importance of flexible information, particularly by those who have information a priori, to achieve a helpful consensus decision by the group. We describe this through analysis of simple models and simulations of more complex models.

The rest of the chapter is organized as follows: We begin with a proposed coupled oscillator model based on the Couzin et al. [90] agent based model. Then we take a step backwards and consider a model with two groups in one spatial dimension that we model as a mass spring system. We look at the analysis and simulation of a variety of models in one spatial dimension with both linear and non-linear components that describe the conflict of two subgroups of differing information. Next we extend our one-spatial-dimension models to two spatial dimensions and repeat the analysis and simulations. Finally we conclude with a discussion of the importance of forgetfulness into the ability to make a productive consensus decision.

4.2 Coupled Oscillator Model

We begin by examining a continuous-time coupled oscillator model of collective behavior among individuals with conflicting information.

4.2.1 Nabet Model

A coupled oscillator model of such a scenario was introduced by Nabet et al. [96]:

$$\dot{\theta}_i = \sin(\theta_1 - \theta_i) + \frac{K}{N}\sum_{j=1}^{N}\sin(\theta_j - \theta_i) \tag{4.3}$$

$$\dot{\theta}_i = \sin(\theta_2 - \theta_i) + \frac{K}{N}\sum_{j=1}^{N}\sin(\theta_j - \theta_i) \tag{4.4}$$

$$\dot{\theta}_i = \frac{K}{N}\sum_{j=1}^{N}\sin(\theta_j - \theta_i) \tag{4.5}$$

where θ_i denotes the direction of an individual, K denotes the cohesiveness of the group, and N denotes the total number of individuals. Equation (4.3) represents informed individuals with desired direction θ_1. Equation (4.4) represents informed individuals with desired direction θ_2. Equation (4.5) represents naive individuals. Nabet et al. [96], however, immediately neglect the naive individuals and assume all individuals in a subgroup have identical dynamics. This reduces the system to two ODEs.

By examining the fixed points of the two ODE system, it is known that either the groups end precisely at the average of the two desired directions or the groups split apart and each approaches their desired direction. With the model in its current instantiation, there is no opportunity for the groups to reach a productive consensus decision; they can only average.

Nabet et al. [96] forced productive consensus decision making by including a "forgetfulness" term in the form of a Gaussian ($e^{\frac{-\sin(\theta_1-\theta_i)^2}{0.2}}$) multiplying their desired direction function. Due to the exponential in this term, at distances away from the desired direction the attraction to the desired direction decays

rapidly to zero. Under such conditions they find productive consensus decision making occurs for a sufficient separation of angles. This idea agrees with the simulation results obtained by Couzin et al. [90], who alter their value of ω, a parameter that adjusts the importance of the desired direction.

With the inclusion of only informed individuals with conflicting information, it is impossible to get productive consensus decision making without the aid of forgetting.

4.3 Modeling Two Populations in One Spatial Dimension

As the self-propelled particle models with two spatial dimension introduced by Couzin et al. [90] were impossible to analyze, and interesting behavior was exhibited in a one-dimensional space (i.e. during trap-lining), we decided to start by taking a step backward and considered a model with one spatial dimension. We considered a population of two informed groups moving along a line. As in the self-propelled particle models in two spatial dimensions, the movement of each group was determined by the interplay of desire to go to a certain location and desire to stay with the group. As in some of the models by Couzin et al. [95] we consider a desired location here rather than a desired direction.

4.3.1 Basic Mass-Spring Model

Our initial model involved considering the groups as masses and their interconnections as springs to apply the wealth of prior research that has been done into mass-spring systems.

Spring Background

Standard theory into mass-spring dynamics states that when a spring is moved from equilibrium there is a restoring force. This force is commonly applied linearly using Hooke's Law: $F = -kx$ where k is the spring constant with units $\frac{mass*distance}{time^2}$. Additionally, there can be a frictional damping force in such systems: $F = -cv$ where c is the damping constant with units $\frac{mass}{time}$ and v is the velocity. This elicits a traditional mass spring system with a single mass and spring:

$$F = -cv - kx$$

$$mx'' = -cx' - kx$$

This system can, of course, be modified to include multiple interconnected springs and masses, as we will do below.

As noted above, Hooke's Law implies a linear restoring force by springs. However, we find a non-linear restoring force to be more appropriate to describe the biology of fish schools. Instead of standard linear relations, we are interested in a model of the form:

$$mx'' + cp(x') + kq(x) = 0$$

where $p(x')$ and $q(x)$ may be non-linear functions.

4.3.2 Variations on the Function of Position

We begin by considering models with only two groups, both informed, but in opposite directions. This gives us the system of equations:

$$\begin{aligned} mx_1'' + cx_1' + kq_1(x_1, x_2) &= 0 \\ mx_2'' + cx_2' + kq_2(x_1, x_2) &= 0 \end{aligned} \tag{4.6}$$

Here we have chosen a linear function of the first derivatives and a non-linear function of the variables.

Position Function

We consider four cases of the function of the position, $q(x_1, x_2)$. See Figure 4.1. In all four cases, there are two parts to each function of the position: one part that determines the attraction to a certain location and the other part determines the attraction to the group. The first terms of each equation below determine the attraction to a particular location, either Ψ for x_1 or $-\Psi$ for x_2. The last terms of each equation determine the attraction to the centroid of the group. The constant, α, determines the relative strength of the attraction to a location in relation to attraction to the group. $\bar{x}$ is the average of x_1 and x_2

Increasing Attraction: Case A

In this, the simplest of cases, each group has linearly increasing attraction to return to a particular location or to return to the group (Figure 4.1). The further from the desired the location, the stronger the pull back to it. Similar with the

Figure 4.1: Functional Forms of Attraction

This graph shows the functional form governing attraction, either to a desired location or to the group centroid. Case A (solid black line) is linearly increasing attraction. Case B (dot-dash black line) is long-range decay of attraction where the function increases to a maximum and then decays to zero. Case C is long-range asymptote of attraction where the function increases to an asymptotic maximum. Case C is expressed by two functional forms: absolute value (dotted black line) and inverse tangent (red x markers). Case D is long-range decay of attraction to an asymptote where the function increases to a maximum and then decays to a non-zero constant. Case D is also expressed by two functional forms: absolute value (dashed gray line) and inverse tangent (red + markers). The exact functional form of each case is described in the text. The values of constants in these functions are the same as those used in simulations: $A = 1$, $B = \frac{1}{10}$, $C = \frac{1}{2}$, $D = \frac{1}{10}$, $F = 10$.

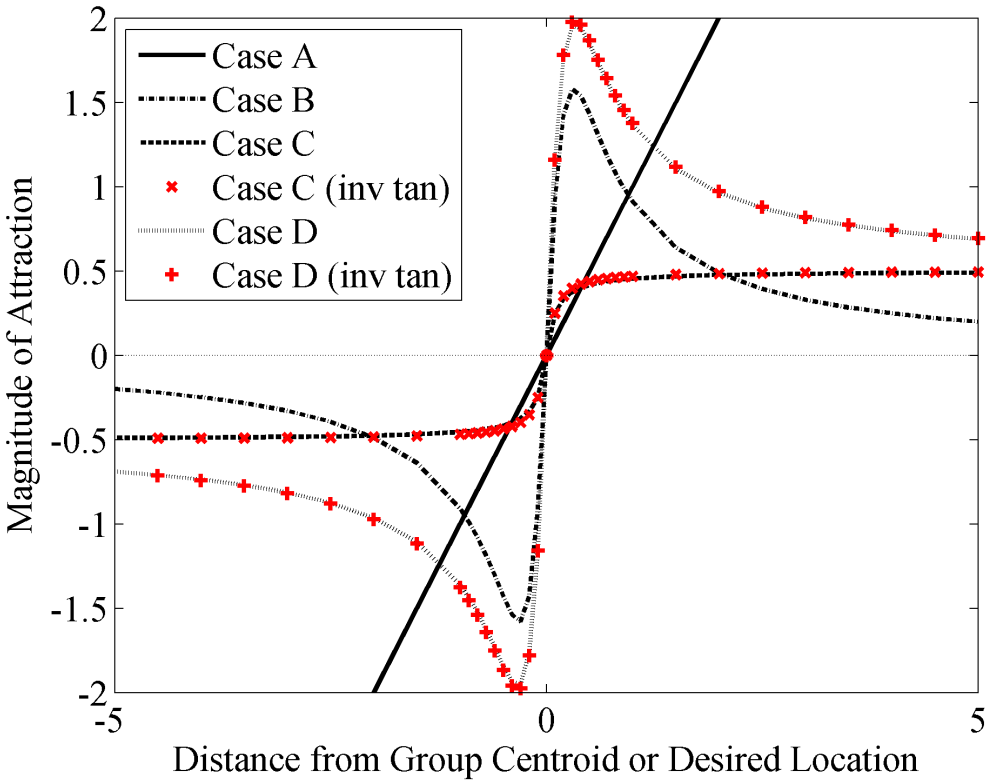
Case A
Case B
Case C
Case C (inv tan)
Case D
Case D (inv tan)
Magnitude of Attraction
Distance from Group Centroid or Desired Location
2
1.5
1
0.5
0
-0.5
-1
-1.5
-2
-5
0
5

group: the further from the group, the stronger the attraction.

$$q_{A_1}(x_1, x_2) = \alpha\left[(\Psi - x_1)\right] + (\bar{x} - x_1)$$
$$q_{A_2}(x_1, x_2) = \alpha\left[(-\Psi - x_2)\right] + (\bar{x} - x_2)$$

Long-range Decay of Attraction: Case B

In this case, the attraction to a particular location initially increases as an individual moves away from that location (Figure 4.1). As it increases further the attraction to return is maximized and ultimately, as the individual continues to move further from the location of interest, the attraction decays to zero. There is similar behavior regarding attraction to the group: at short distances from the group centroid the attraction to the group increases but at long distances the attraction decays to zero.

$$q_{B_1}(x_1, x_2) = \alpha\left[\frac{A(\Psi - x_1)}{B + (\Psi - x_1)^2}\right] + \frac{A(\bar{x} - x_1)}{B + (\bar{x} - x_1)^2}$$
$$q_{B_2}(x_1, x_2) = \alpha\left[\frac{A(-\Psi - x_2)}{B + (-\Psi - x_2)^2}\right] + \frac{A(\bar{x} - x_2)}{B + (\bar{x} - x_2)^2}$$

The specifics of the function governing the attraction of the individual to the location and the group are specified by the constants A and B, both of which have units of $distance^2$. With the above functional form, the individual will feel the maximum attraction ($\frac{A}{2\sqrt{B}}$) to return to the desired location (or group centroid) when $\sqrt{B}$ from the desired location (or group centroid).

Long-range Asymptote of Attraction: Case C

In this case, the attraction to a particular location increases as you move away from that location and ultimately plateaus at a constant value (Figure 4.1). There is similar behavior regarding attraction to the group: at short distances attraction increases until leveling off at a maximum value.

$$q_{C_1}(x_1, x_2) = \alpha \left[\frac{C(\Psi - x_1)}{D + |(\Psi - x_1)|} \right] + \frac{C(\bar{x} - x_1)}{D + |(\bar{x} - x_1)|}$$
$$q_{C_2}(x_1, x_2) = \alpha \left[\frac{C(-\Psi - x_2)}{D + |(-\Psi - x_2)|} \right] + \frac{C(\bar{x} - x_2)}{D + |(\bar{x} - x_2)|}$$

The specifics of the function governing the attraction of the individual to the location or the group are specified by the constants C and D, both of which have units *distance*. With such a functional form, the individual will feel a maximum attraction (C) to return when sufficiently far from the desired location (or group centroid). However, because of the presence of the absolute value, this is a piecewise continuous function which has the ability to create complicated dynamics at the boundaries, as described later (Section 4.3.3). We avoid this by using inverse tangent ($\tan^{-1}$) which is continuous.

$$q_{C_1}(x_1, x_2) = \frac{2C}{\pi} \left(\alpha \left[\tan^{-1}(F(\Psi - x_1)) \right] + \tan^{-1}(F(\bar{x} - x_1)) \right)$$
$$q_{C_2}(x_1, x_2) = \frac{2C}{\pi} \left(\alpha \left[\tan^{-1}(F(-\Psi - x_2)) \right] + \tan^{-1}(F(\bar{x} - x_2)) \right)$$

The specifics of the function governing the attraction of the individual to the location or the group are specified by the constants C and F. The constant C has units of *distance*, and the individual feels the maximum attraction C when sufficiently far from the desired location (or group centroid). Since $\tan^{-1}$ has the range $(\frac{-\pi}{2}, \frac{\pi}{2})$, we choose the constant to be $\frac{2C}{\pi}$ so the function asymptotes

at C which is analogous to the previous piecewise equations for Case C. The constant F has units *distance* and determines how steeply the $\tan^{-1}$ approaches its maximum. We choose $F = 10$ so that both functions for Case C are almost identical (Figure 4.1).

Long-range Partial Decay of Attraction: Case D

The final case incorporates the previous two cases (long-range decay and long-range asymptote of attraction) and involves an initial increase to a maximum followed by decay of attraction to a lower than maximum but non-zero value (Figure 4.1). At short distances from the desired location, the attraction initially increases until a maximum and then begins to decay but ultimately plateaus at a non-zero value. Analogous behavior is seen with the attraction to the group centroid.

$$q_{D_1}(x_1, x_2) = \alpha \left[\frac{A(\Psi - x_1)}{B + (\Psi - x_1)^2} + \frac{C(\Psi - x_1)}{D + |(\Psi - x_1)|} \right] + \frac{A(\bar{x} - x_1)}{B + (\bar{x} - x_1)^2} + \frac{C(\bar{x} - x_1)}{D + |(\bar{x} - x_1)|}$$

$$q_{D_2}(x_1, x_2) = \alpha \left[\frac{A(-\Psi - x_2)}{B + (-\Psi - x_2)^2} + \frac{C(-\Psi - x_2)}{D + |(-\Psi - x_2)|} \right] + \frac{A(\bar{x} - x_2)}{B + (\bar{x} - x_2)^2} + \frac{C(\bar{x} - x_2)}{D + |(\bar{x} - x_2)|}$$

The specifics of the function of the attraction of the individual are specified by the constants A and B with units $distance^2$ as well as C and D with units $distance$. The individual will feel a an attraction (C) to return when sufficiently far from the desired location (or group centroid). Again to avoid a piecewise

function, we replace the absolute value terms with inverse tangent.

$$
\begin{aligned}
q_{D_1}(x_1, x_2) = \alpha \Bigg[& \frac{A(\Psi - x_1)}{B + (\Psi - x_1)^2} + \frac{2C}{\pi} \tan^{-1}(F(\Psi - x_1)) \Bigg] \\
& + \frac{A(\bar{x} - x_1)}{B + (\bar{x} - x_1)^2} + \frac{2C}{\pi} \tan^{-1}(F(\bar{x} - x_1)) \\
q_{D_2}(x_1, x_2) = \alpha \Bigg[& \frac{A(-\Psi - x_2)}{B + (-\Psi - x_2)^2} + \frac{2C}{\pi} \tan^{-1}(F(-\Psi - x_2)) \Bigg] \\
& + \frac{A(\bar{x} - x_2)}{B + (\bar{x} - x_2)^2} + \frac{2C}{\pi} \tan^{-1}(F(\bar{x} - x_2)
\end{aligned}
$$

The constant C has units of *distance*, and the individual feels the attraction C when sufficiently far from the desired location (or group centroid). Since $\tan^{-1}$ has the range $(\frac{-\pi}{2}, \frac{\pi}{2})$, we choose the constant to be $\frac{2C}{\pi}$ so the function asymptotes at C which is analogous to the previous piecewise equations for Case D. The constant F has units *distance* and determines how steeply the $\tan^{-1}$ approaches its maximum. We choose $F = 10$ so that all functions for Case D are almost identical (Figure 4.1).

Non-dimensionalization

In order to continue, we needed to non-dimensionalize our equations. For illustrative purposes, let us focus on the Case B from above. By noting that the second derivative of position is the first derivative of velocity, we reformulate this into an four-dimensional ODE system:

$$
\begin{aligned}
x_1' &= v_1 \\
v_1' &= \frac{1}{\tau^2} \left\{ \alpha \left[\frac{A(\Psi - x_1)}{B + (\Psi - x_1)^2} \right] + \frac{A(\bar{x} - x_1)}{B + (\bar{x} - x_1)^2} \right\} - r v_1 \\
x_2' &= v_2 \\
v_2' &= \frac{1}{\tau^2} \left\{ \alpha \left[\frac{A(-\Psi - x_2)}{B + (-\Psi - x_2)^2} \right] + \frac{A(\bar{x} - x_2)}{B + (\bar{x} - x_2)^2} \right\} - r v_2
\end{aligned}
$$

Here $\frac{1}{\tau^2}$ is our spring constant corresponding to k in Equation (4.6) with units $\frac{1}{time^2}$ and r is our damping constant corresponding to c in Equation (4.6) with units $\frac{1}{time}$. We have removed mass from our equations by assuming that the mass of each group is one.

By letting $t = \tau T$, $x = \Psi X$, $v = \frac{\Psi}{\tau} V$, $A = \Psi^2 a$, and $B = \Psi^2 b$ where X, T, V, a and b are non-dimensional, we obtain a non-dimensionalized system:

$$\begin{aligned} X_1' &= V_1 \\ V_1' &= \alpha \left[\frac{a(1 - X_1)}{b + (1 - X_1)^2} \right] + \frac{a(\bar{X} - X_1)}{b + (\bar{X} - X_1)^2} - \sigma V_1 \\ X_2' &= V_2 \\ V_2' &= \alpha \left[\frac{a(-1 - X_2)}{b + (-1 - X_2)^2} \right] + \frac{a(\bar{X} - X_2)}{b + (\bar{X} - X_2)^2} - \sigma V_2 \end{aligned} \tag{4.7}$$

The constants a and b determine the shape of our functions. Additionally, α and $\sigma = r\tau$ are parameters in our system.

Following similar conventions, we can find the non-dimensionalization for Cases A, C and D as well.

For Case A we us $t = \tau T$, $x = \Psi X$, and $v = \frac{\Psi}{\tau} V$ where X, T, and V are non-dimensional, to obtain a non-dimensionalized system:

$$\begin{aligned} X_1' &= V_1 \\ V_1' &= \alpha(1 - X_1) + (\bar{X} - X_1) - \sigma V_1 \\ X_2' &= V_2 \\ V_2' &= \alpha(-1 - X_2) + (\bar{X} - X_2) - \sigma V_2 \end{aligned}$$

For Case C we us $t = \tau T$, $x = \Psi X$, $v = \frac{\Psi}{\tau} V$, $C = \Psi c$, and $F = \Psi f$ where X, T, V,

c and f are non-dimensional, to obtain a non-dimensionalized system:

$$
\begin{aligned}
X_1' &= V_1 \\
V_1' &= \frac{2c}{\pi}\left(\alpha\left[\tan^{-1}(f(1-X_1))\right] + \tan^{-1}(f(\bar{X}-X_1))\right) - \sigma V_1 \\
X_2' &= V_2 \\
V_2' &= \frac{2c}{\pi}\left(\alpha\left[\tan^{-1}(f(-1-X_2))\right] + \tan^{-1}(f(\bar{X}-X_2))\right) - \sigma V_2
\end{aligned}
$$

For Case D, we use $t = \tau T$, $x = \Psi X$, $v = \frac{\Psi}{\tau} V$, $A = \Psi^2 a$, $B = \Psi^2 b$ $C = \Psi c$, and $F = \Psi f$ where X, T, V, a, b, c and f are non-dimensional, to obtain a non-dimensionalized system:

$$
\begin{aligned}
X_1' &= V_1 \\
V_1' &= \alpha\left[\frac{a(1-X_1)}{b+(1-X_1)^2} + \frac{2c}{\pi}\tan^{-1}(f(1-X_1))\right] \\
&\quad + \left[\frac{a(\bar{X}-X_1)}{b+(\bar{X}-X_1)^2} + \frac{2c}{\pi}\tan^{-1}(f(\bar{X}-X_1))\right] - \sigma V_1 \\
X_2' &= V_2 \\
V_2' &= \alpha\left[\frac{a(-1-X_2)}{b+(-1-X_2)^2} + \frac{2c}{\pi}\tan^{-1}(f(-1-X_2))\right] \\
&\quad + \left[\frac{a(\bar{X}-X_2)}{b+(\bar{X}-X_2)^2} + \frac{2c}{\pi}\tan^{-1}(f(\bar{X}-X_2))\right] - \sigma V_2
\end{aligned}
$$

Fixed Point Analysis

To solve for fixed points, we look for solutions when all our four ODEs are equal to zero. Because of the form of our system, V_1 and V_2 are always zero for any fixed point. To determine the stability of our fixed points we examine the eigenvalues of the Jacobian evaluated at our fixed point. Although we have a four dimensional system the eigenvalues associated with the $X_1' = X_2' = 0$ directions always have negative real parts. Since for all fixed points, the velocity is zero

($V_1 = V_2 = 0$, the eigenvalues with associated eigendirections are always negative, indicating the dynamics in the $X_1 - X_2$ plane are attracting. Thus, we only need to consider the eigenvalues associated with the other two eigendirections to establish stability of our fixed points.

We can solve Case A analytically for all positive values of α and σ. There is one fixed point, $(\frac{\alpha}{1+\alpha}, \frac{-\alpha}{1+\alpha})$ which is stable for all parameter values. In other words, all parameters lead to splitting around the average of zero. This Case does not exhibit interesting dynamics.

We can solve Case B analytically for fixed points of the system when $\alpha = 1$. In that case there are seven fixed points, three of which are stable (Table 4.1). All the fixed points depend on the value of b which is always positive, by construction.

Table 4.1: Fixed points and Stability of One-Spatial-Dimension Model when $\alpha = 1$

X_1	X_2	V_1	V_2	Stability
$\frac{1}{2}$	$\frac{1}{2}$	0	0	Unstable
$\frac{1}{2}(1 - \sqrt{1-4b})$	$\frac{1}{2}(-1 + \sqrt{1-4b})$	0	0	Unstable
$\frac{1}{2}(1 + \sqrt{1-4b})$	$\frac{1}{2}(-1 - \sqrt{1-4b})$	0	0	Stable
$\frac{1}{3}(2 - \sqrt{1-3b})$	$-\sqrt{1-3b}$	0	0	Unstable
$\frac{1}{3}(2 + \sqrt{1-3b})$	$\sqrt{1-3b}$	0	0	Stable
$\frac{1}{3}(-2 - \sqrt{1-3b})$	$-\sqrt{1-3b}$	0	0	Stable
$\sqrt{1-3b}$	$\frac{1}{3}(-2 + \sqrt{1-3b})$	0	0	Unstable

Although we cannot analytically solve for the fixed points when $\alpha \neq 1$ we can numerically solve for the fixed points, as we will see in the next section.

We can also solve Case C analytically for fixed points of the system when $\alpha = 1$. To solve we must take the tangent of the simplified equations. Conveniently $\tan(a+b) = \frac{\tan(a)+\tan(b)}{1-\tan(a)\tan(b)}$. Thus, when $\alpha = 1$ all the inverse tangents fall out because of the tangents and there is a single stable fixed point $(\frac{1}{2}, -\frac{1}{2})$. Although this trick does not work unless $\alpha = 1$, we can still solve numerically for the fixed point for other values of α. We find that Case C always has one stable fixed point.

We can only solve for Case D numerically. Like Case B, there are multiple fixed points which we explore more in the next section.

Bifurcation Analysis

Here we again use Case B as an illustration. In Case B, there are four parameters in the non-dimensionalized model: a, b, α and σ. The parameters σ and a do not appear in the fixed point equations. σ does not affect the fixed point, because V_1 and V_2 always equal zero for our fixed points and σ only appears multiplying V_1 and V_2. Additionally, a is in all terms left after V_1 and V_2 are set to zero so it can be divided out without altering the fixed points. This leaves two possible parameters to consider: b and α. We fix b at the particular value of $\frac{1}{10}$ to have the shape of the function of position we desire.

This leaves α as the parameter to vary. Recall, α represents the relative strength of attraction to a fixed location over attraction to the centroid of the group. We consider varying α over positive numbers. We solve the equations for all positive α and find a varying number of fixed points, between one and seven.

For small, positive α, there are three fixed points, two stable sinks and one

unstable saddle. As alpha is increased, there are five saddle node bifurcations. The first saddle node, denoted A in Figure 4.2, is encountered at $\alpha \approx 0.735$ creating a stable sink and an unstable source, for a total of five fixed points: two unstable, three stable. The second saddle node, denoted B in Figure 4.2, is encountered at $\alpha \approx 0.762$ creating two unstable saddles, for a total of seven fixed points: three stable, four unstable. It is in this region where we encounter $\alpha = 1$. The third saddle node, denoted C in Figure 4.2, is encountered at $\alpha \approx 1.351$ where an unstable source and an unstable saddle collide, for a total of five fixed points: three stable and two unstable. The fourth and fifth saddle nodes, denoted D_+ and D_- in Figure 4.2, both occur at $\alpha \approx 2.32$ and both entail an unstable saddle colliding with a stable sink. The reason these two fixed points occur at the same point is described below. This results in one stable fixed point which exists and approaches 1 for X_1 and -1 for X_2 as α increases.

The set up of the equations of this model dictate the presence of a symmetry: $X_1 = -X_2$. This symmetry occurs because X_1 is attracted to 1 and X_2 is attracted to -1 and all other aspects of the equations are reciprocal. All of the fixed points in this system either lie on the $X_1 = -X_2$ line or are mirrored across the $X_1 = -X_2$ line. Initially of the three fixed points one is of the form $(X_1, -X_1)$, lying on the $X_1 = -X_2$ line, and two are $(X_1, X_2) = -(X_2, X_1)$, mirrored across the $X_1 = -X_2$ line. The latter two fixed points are stable. The first bifurcation encountered introduces two more fixed points, one stable and one unstable, both of the form $(X_1, -X_1)$, and both lying on the $X_1 = -X_2$ line. The next bifurcation introduces two unstable fixed points of the form $(X_1, X_2) = -(X_2, X_1)$ born from and mirrored across the $X_1 = -X_2$ line. The third bifurcation eliminates two unstable fixed points lying on the $X_1 = -X_2$ line. This leave five fixed points, only one of which is on the $X_1 = -X_2$ line of symmetry. The other four appear in pairs

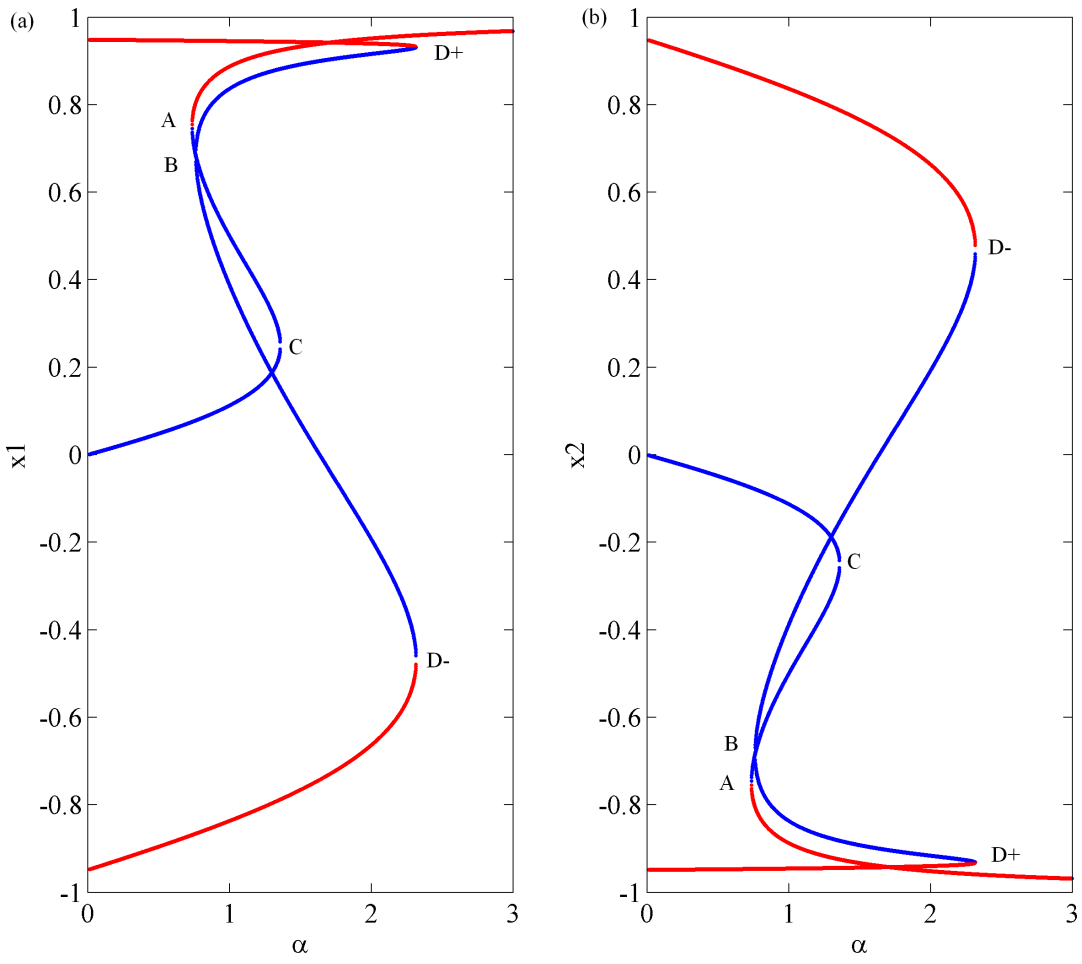

Figure 4.2: Bifurcation Diagram of Model in One Spatial Dimension

Bifurcation diagram for the long-range decay of attraction (Case B) model in one spatial dimension. Curves in red denote stable fixed points while curves in blue denote unstable fixed points. Each bifurcation is denoted by a letter, *A*-*D*, as described in the text.

(a) The left panel shows the bifurcation curves with x_1 as a function of α.

(b) The right panel shows the bifurcation curves with x_2 as a function of α.

moving towards each other as α increases. They are mirrored across the $X_1 = -X_2$ line. When two of the fixed points meet in a saddle node bifurcation, due to the symmetry, the other two must meet as well in a saddle node bifurcation. Thus, the final two bifurcations occur at the same value of α. Afterwards, there remains one stable fixed point lying on the $X_1 = -X_2$ line.

We chose to examine Case B because the bifurcations in Case B and Case D are similar in nature, they just occur at slightly different values for α (results not shown for Case D). Cases A and C only have a single stable fixed point and no bifurcations.

Simulation Results

Next we wanted to understand, how the system behaves over a variety of initial conditions when there are multiple stable fixed points as in Cases B and D. This will determine the basins of attraction for our stable fixed points. Again we use Case B as illustrative where multiple stable fixed points occur when $.735 < \alpha < 2.32$. We consider three values of α: $0.75, 1.2, 2.25$ (Figure 4.3). At these values of α, we examine the long time behavior over variety of initial conditions: $-5 \leq X_1 \leq 5$, $-5 \leq X_2 \leq 5$. Initial conditions were gridded over this region with a step-size of 0.05. X_1 is attracted to 1 and X_2 is attracted to -1 and they are both attracted to stay together as a group.

At $\alpha = 0.75$ there are five fixed points, three of which are stable. Since $\alpha < 1$ we expect the individuals to stay together preferentially over going to their desired location. This is exhibited in Figure 4.3(a). Immediately following the first bifurcation, most of the initial conditions go towards consensus decision

making at either of the two directions. The initial conditions where X_1 is near 1, go to positive consensus decision making and the initial conditions where X_2 is near -1 go to negative consensus decision making. The only area of splitting occurs along the $X_1 = -X_2$ line as both individuals are approximately equally far from their desired location.

As α increases, we have passed through a bifurcation that created two unstable fixed points, which does not affect the basins of attraction. However, as α grows the tendency to split around the average of zero increases and we see in Figure 4.3(b) where the splitting region has enlarged. However, along the $X_1 = 1$ line there remains overwhelming preference to go to positive consensus and along the $X_2 = -1$ line preference to go to negative consensus.

As α increases further we go through a third bifurcation that eliminates two unstable fixed points. Again this has no bearing on the basins of attractions. However, large α means significant bias to the preferred location over staying as a group. Thus, the majority of the initial conditions end in splitting of the population around the average of zero.

4.3.3 Piecewise Linear Model

Although the four cases above are illustrative, due to the non-linearities, we cannot generally find the fixed points to cases B, C and D. We attempted to reformulate the above models, extracting the essential aspects of the functions and representing them via piecewise linear functions, which are in some ways

Figure 4.3: Basins of Attraction of Stable Fixed Points

The long term behavior of the Case B (long-range decay of attraction) system over a variety of initial conditions where $-5 \leq X_1 \leq 5$, $-5 \leq X_2 \leq 5$. Initial conditions were gridded over this region with a step-size of 0.05. X_1 is attracted to 1 and X_2 is attracted to -1; they are both attracted to the group centroid.

(a) The top panel shows the basins of attraction of the three stable fixed point when $\alpha = 0.75$. Gray denotes splitting of the population around the average of 0 such that $x_1 = 0.792$ and $x_2 = -0.792$. Red denotes consensus decision making to the positive side with $x_1 = 0.946$ and $x_2 = 0.867$. Blue denotes consensus decision making to the negative side with $x_1 = -0.867$ and $x_2 = -0.946$.

(b) The middle panel shows the basins of attraction of the three stable fixed point when $\alpha = 1.2$. Gray denotes splitting of the population around the average of 0 such that $x_1 = 0.912$ and $x_2 = -0.912$. Red denotes consensus decision making to the positive side with $x_1 = 0.945$ and $x_2 = 0.810$. Blue denotes consensus decision making to the negative side with $x_1 = -0.810$ and $x_2 = -0.945$.

(c) The bottom panel shows the basins of attraction of the three stable fixed point when $\alpha = 2.3$. Gray denotes splitting of the population around the average of 0 such that $x_1 = 0.958$ and $x_2 = -0.958$. Red denotes consensus decision making to the positive side with $x_1 = 0.934$ and $x_2 = 0.518$. Blue denotes consensus decision making to the negative side with $x_1 = -0.518$ and $x_2 = -0.934$.

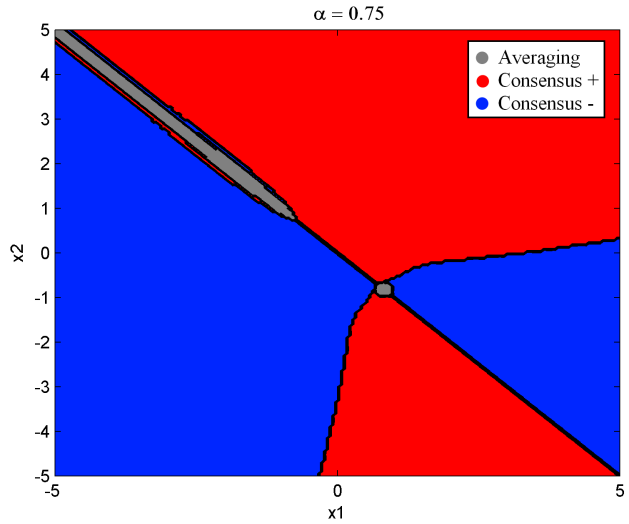
α = 0.75
Averaging
Consensus +
Consensus -
x2
x1
5
4
3
2
1
0
-1
-2
-3
-4
-5
-5
0
5

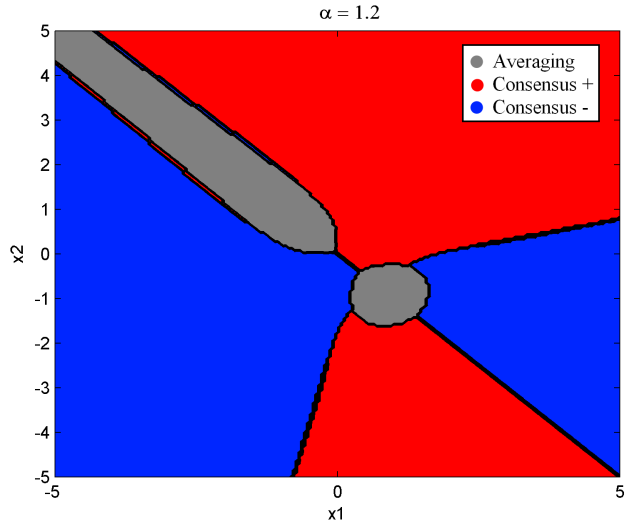
α = 1.2
Averaging
Consensus +
Consensus -
x2
x1
5
4
3
2
1
0
-1
-2
-3
-4
-5
-5
0
5

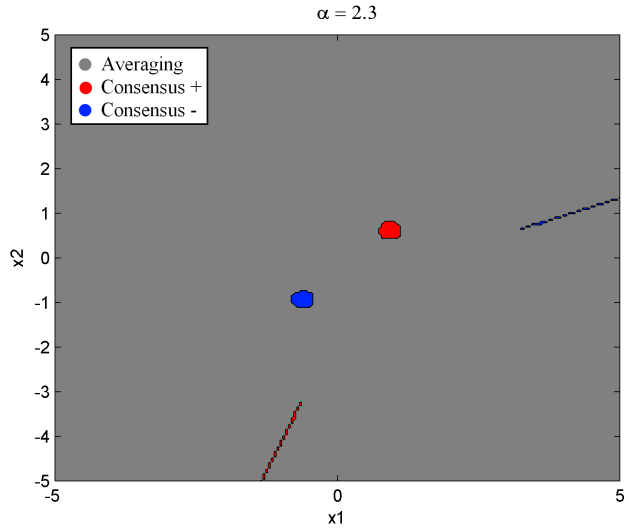
α = 2.3
Averaging
Consensus +
Consensus -
x2
x1
5
4
3
2
1
0
-1
-2
-3
-4
-5
-5
0
5

easier to analyze.

$$
\begin{aligned}
x_1' &= v_1 \\
v_1' &= -rv_1 + \frac{1}{\tau^2}\left[\alpha\begin{cases} -k_1 & \Psi - x_1 < -\kappa \\ \Psi - x_1 & -\kappa \le \Psi - x_1 \le \kappa \\ k_1 & \Psi - x_1 > \kappa \end{cases} + \begin{cases} -k_g & \bar{x} - x_1 < -\kappa \\ \bar{x} - x_1 & -\kappa \le \bar{x} - x_1 \le \kappa \\ k_g & \bar{x} - x_1 > \kappa \end{cases}\right] \\
x_2' &= v_2 \\
v_2' &= -rv_2 + \frac{1}{\tau^2}\left(\alpha\begin{cases} -k_2 & -\Psi - x_2 < -\kappa \\ -\Psi - x_2 & -\kappa \le -\Psi - x_2 \le \kappa \\ k_2 & -\Psi - x_2 > \kappa \end{cases} + \begin{cases} -k_g & \bar{x} - x_2 < -\kappa \\ \bar{x} - x_2 & -\kappa \le \bar{x} - x_2 \le \kappa \\ k_g & \bar{x} - x_2 > \kappa \end{cases}\right)
\end{aligned} \tag{4.8}
$$

Here $\frac{1}{\tau^2}$ is our spring constant corresponding to k with units $\frac{1}{time^2}$, r is our damping constant corresponding to c with units $\frac{1}{time}$, and Ψ ($-\Psi$) is the desired direction of x_1 (x_2). The constant k_1 (k_2) is the asymptotic value of the function describing the attraction of x_1 (x_2) to its desired location. The constant k_g is the asymptotic value of the function describing the attraction of the individual to the group centroid. The constant κ determines the size of the regions of each part of the piecewise functions. Further, it is important to notice that the second piecewise function in both v_i' equations is equal to the negative of the other.

Since there are three parts to each of three piecewise functions that compose are four ODE system, there are 27 separate functions to consider, each dependent on the relationship of x_1 and x_2. Although the boundaries of the regions are specified such that the boundary points lie in the middle function of each piecewise function, in terms of the analysis it does not matter which regions contain these boundary points.

Relationship of Piecewise Function to Cases in Section 4.3.2

All of the previous cases are illustrated with this piecewise model, depending on the choice of the k_i's and κ. Case A in its original formulation is already linear, but not terribly interesting. To associate Equation (4.8) with Case A, take $\kappa = \infty$ and the functions are no longer piecewise but always linear. For our piecewise system, Equation (4.8), to be analogous to Case B, we take $k_1 = k_2 = k_g = 0$. All functions immediately become zero after they reach their maximum. For Equation (4.8) to be analogous to Case C, we take $k_1 = k_2 = k_g = \kappa$. All functions rise linearly to a maximum of κ. Finally, for Equation (4.8) to be analogous to Case D, we take $k_1 = k_2 = k_g = \frac{\kappa}{constant}$ where the constant depends upon on how far down the function decays.

Non-dimensionalization of Piecewise System

As in our original model, we want to work with the non-dimensionalized system. By letting $t = \tau T$, $x = \Psi X$, and $v = \frac{\Psi}{\tau} V$ where X, T, and V are non-

dimensional, we obtain a non-dimensionalized system:

$$
\begin{aligned}
X_1' &= V_1 \\
V_1' &= -\sigma V_1 + \left[\alpha \begin{cases} -k_1 & 1 - X_1 < -\kappa \\ 1 - X_1 & -\kappa \le 1 - X_1 \le \kappa \\ k_1 & 1 - X_1 > \kappa \end{cases} + \begin{cases} -k_g & \bar{X} - X_1 < -\kappa \\ \bar{X} - X_1 & -\kappa \le \bar{X} - X_1 \le \kappa \\ k_g & \bar{X} - X_1 > \kappa \end{cases} \right] \\
X_2' &= V_2 \\
V_2' &= -\sigma V_2 + \left[\alpha \begin{cases} -k_2 & -1 - X_2 < -\kappa \\ -1 - X_2 & -\kappa \le -1 - X_2 \le \kappa \\ k_2 & -1 - X_2 > \kappa \end{cases} + \begin{cases} -k_g & \bar{X} - X_2 < -\kappa \\ \bar{X} - X_2 & -\kappa \le \bar{X} - X_2 \le \kappa \\ k_g & \bar{X} - X_2 > \kappa \end{cases} \right]
\end{aligned} \tag{4.9}
$$

The k_i's and κ remain exactly as in the non-dimensionalized system. As in the non-piecewise system, α and $\sigma = r\tau$ are parameters in our system.

Fixed Point Analysis

There is a large body of literature about the analysis of traditional dynamical systems. However, many physical systems are left out because they are characterized by a period of smooth dynamics separated by events that on the slow time scale appear instantaneous. These instantaneous events cause non-smooth jumps in the governing equations. The non-smoothness can be at several levels: discontinuities in the function itself, in the first derivative or in higher order derivatives. The dynamics of each of these types of systems have been analyzed but the non-smoothness leads to many unexpected dynamics [97]. It is not enough to only consider dynamics within each region, but boundary dynamics must be considered as well. The dynamics on the boundary can become quite complicated [97].

Most of our piecewise system falls under what is known as a Filippov flow [97]. Filippov flows are ones where there is a jump in the value of the derivative as is seen in Equation 4.9 when $k_i \neq \kappa$. Because the derivatives have jumps we generically do not find simple codimension one bifurcations [97]. There is the possibility of sliding motion and equilibria there. Unfortunately, a complete understanding of the dynamics when the system is more than two dimensions remains unknown [97].

Fixed Points

We first search for fixed points within our regions. This is done as in standard dynamical systems analysis by searching for places where the equations equal zero simultaneously. As we noted previously, the piecewise version of Case A is actually equivalent to Case A and has the same single stable fixed point, $(\frac{\alpha}{1+\alpha}, \frac{-\alpha}{1+\alpha})$.

The piecewise system, Equation 4.9, represents Cases B-D dependent upon the choice for the k_i's. For general values of our constants, there are seven fixed points within regions (Table 4.2). All of the seven fixed points are stable. However, not all seven fixed points exist for any given choices of α, k_i's and κ.

We examine the system when $\kappa = 1$. We do not yet pick values for the k_i's. For this particular choice of κ, only three of the fixed points listed in Table 4.2 fall within existent regions: $(1 - k_2, 1 - (1 + 2\alpha)k_2)$, $(\frac{\alpha}{1+\alpha}, \frac{-\alpha}{1+\alpha})$, $(-1 + (1 + 2\alpha)k_1, -1 + k_1)$. A fourth fixed point, $(\frac{\alpha-k_g}{\alpha}, \frac{-\alpha+k_g}{\alpha})$, lies on the boundary of two regions. The remaining three fixed points lie within regions which do not exist with our choice

Table 4.2: Fixed points and Stability of Piecewise Linear Model

X_1	X_2	V_1	V_2	Region	Stability
$-1-(1+2\alpha)k_1$	$-1-k_1$	0	0	$\begin{cases} 1-x_1 < -\kappa \\ -\kappa \le -1-x_2 \le -\kappa \\ -\kappa \le \frac{x_1-x_2}{2} \le \kappa \end{cases}$	Stable
$1-k_2$	$1-(1+2\alpha)k_2$	0	0	$\begin{cases} -\kappa \le 1-x_1 \le \kappa \\ -1-x_2 < -\kappa \\ -\kappa \le \frac{x_2-x_1}{2} \le \kappa \end{cases}$	Stable
$\frac{\alpha-k_g}{\alpha}$	$\frac{-\alpha+k_g}{\alpha}$	0	0	$\begin{cases} -\kappa \le 1-x_1 \le \kappa \\ -\kappa \le -1-x_2 \le \kappa \\ \frac{x_2-x_1}{2} < -\kappa \end{cases}$	Stable
$\frac{\alpha}{1+\alpha}$	$\frac{-\alpha}{1+\alpha}$	0	0	$\begin{cases} -\kappa \le 1-x_1 \le \kappa \\ -\kappa \le -1-x_2 \le \kappa \\ -\kappa \le \frac{x_2-x_1}{2} \le \kappa \end{cases}$	Stable
$\frac{\alpha+k_g}{\alpha}$	$\frac{-\alpha-k_g}{\alpha}$	0	0	$\begin{cases} -\kappa \le 1-x_1 \le \kappa \\ -\kappa \le -1-x_2 \le -\kappa \\ \frac{x_1-x_2}{2} < -\kappa \end{cases}$	Stable
$1+k_2$	$1+(1+2\alpha)k_2$	0	0	$\begin{cases} -\kappa \le 1-x_1 \le \kappa \\ -1-x_2 > \kappa \\ -\kappa \le \frac{x_2-x_1}{2} \le \kappa \end{cases}$	Stable
$-1+(1+2\alpha)k_1$	$-1+k_1$	0	0	$\begin{cases} 1-x_1 > \kappa \\ -\kappa \le -1-x_2 \le \kappa \\ -\kappa \le \frac{x_2-x_1}{2} \le \kappa \end{cases}$	Stable

of parameters.

Because our system is four dimensional, no complete understanding of the piecewise dynamics exists. We cannot confidently say anything more about the fixed points, analytically. However, we can examine our equilibrium points with simulation. We find that the three equilibrium points within valid regions but not the one in the boundary are stable in simulations (not shown).

4.4 Model in Two Spatial Dimensions

Next we extend our equations to two spatial dimensions by adding a y-component to each of the equations. Since Case A and Case C do not give interesting dynamics and Case B and Case D give similar dynamics (although Case B is much easier to deal with mathematically since it lacks an inverse tangent), we choose to use Case B as an illustrative example. Here, we skip straight to the non-dimensionalized version using the reduction ($t = \tau T$, $x = \Psi X$, $V = \frac{\Psi}{\tau} V$, $a = \Psi^2 A$, $b = \Psi^2 B$). Group X_1 is attracted to $(1, 1)$ and X_2 to $(-1-, 1)$. In order to relate the x- and y-components of each group, we take the Case B function applied to the distance to a point and multiple by the direction towards that point. For example, the term examining movement of X_1 towards its desired location $X_1 = 1$ is governed by the function of the distance to the desired location of $(1, 1)$ multiplied by the unit vector in the direction of $1 - X_1$: $\frac{a* \sqrt{(1-X_1)^2+(1-Y_1)^2}}{b+(\sqrt{(1-X_1)^2+(1-Y_1)^2})^2} \frac{1-X_1}{\sqrt{(1-X_1)^2+(1-Y_1)^2}}$. This simplifies to $\frac{a(1-X_1)}{b+(1-X_1)^2+(1-Y_1)^2}$ which includes the square of the distance in the denominator. Analogous terms are included

for X_2, Y_1, and Y_2 and this results in an eight equation system:

$$
\begin{aligned}
X_1' &= V_{x_1} \\
V_{x_1}' &= \alpha \left[\frac{a(1 - X_1)}{b + (1 - X_1)^2 + (1 - Y_1)^2} \right] + \frac{a(\bar{X} - X_1)}{b + (\bar{X} - X_1)^2 + (\bar{Y} - Y_1)^2} - \sigma V_{x_1} \\
Y_1' &= V_{y_1} \\
V_{y_1}' &= \alpha \left[\frac{a(1 - Y_1)}{b + (1 - X_1)^2 + (1 - Y_1)^2} \right] + \frac{a(\bar{Y} - Y_1)}{b + (\bar{X} - X_1)^2 + (\bar{Y} - Y_1)^2} - \sigma V_{y_1} \\
X_2' &= V_{x_2} \\
V_{x_2}' &= \alpha \left[\frac{a(-1 - X_2)}{b + (-1 - X_2)^2 + (-1 - Y_2)^2} \right] + \frac{a(\bar{X} - X_2)}{b + (\bar{X} - X_2)^2 + (\bar{Y} - Y_2)^2} - \sigma V_{x_2} \\
Y_2' &= V_{y_2} \\
V_{y_2}' &= \alpha \left[\frac{a(-1 - Y_2)}{b + (-1 - X_2)^2 + (-1 - Y_2)^2} \right] + \frac{a(\bar{Y} - Y_2)}{b + (\bar{X} - X_2)^2 + (\bar{Y} - Y_2)^2} - \sigma V_{y_2}
\end{aligned} \tag{4.10}
$$

4.4.1 Fixed Points and Bifurcations

To solve for the fixed points in our two-spatial-dimension model we search for solutions when all eight Equations (4.10) are equal to zero. For any fixed point, $V_{x_1} = V_{y_1} = V_{x_2} = V_{y_2} = 0$. We find that the system, similar to our models in one spatial dimension, can only be solved analytically under special conditions but we can easily solve for our fixed points numerically.

Again, we use α, representing the relative strength of attraction to a fixed location over attraction to the group centroid, as our bifurcation parameter. As we vary α over positive numbers there are between one and seven fixed points as in the model in one spatial dimension. In fact, the bifurcation diagrams for the model in two spatial dimensions are almost identical to those for the model in one spatial dimensions, except the bifurcations in two spatial dimensions

occur at slightly smaller values of α (Figure 4.4).

For small, positive α, there are three fixed points: two stable sinks and one unstable saddle. As alpha is increased, there are five saddle node bifurcations. The first saddle node bifurcation creates a stable sink and an unstable source, for a total of five fixed points: two unstable, three stable. The second saddle node bifurcation creates two unstable saddles, for a total of seven fixed points: three stable, four unstable. The third saddle node bifurcation is where an unstable source and an unstable saddle collide, for a total of five fixed points: three stable and two unstable. The fourth and fifth saddle node bifurcations both entail an unstable saddle colliding with a stable sink and occur for the same value of α. This occurs similarly to the model in one spatial dimension because of the $X_1 = -X_2$ ($Y_1 = -Y_2$) symmetry. This results in one stable fixed point which exists and approaches 1 for X_1 and Y_1 and -1 for X_2 and Y_2 as α increases.

4.4.2 Transient Oscillations

We do not see persistent oscillations in any of our systems either in one or two spatial dimensions. There are only stable and unstable fixed points, no limit cycles. However, there are damped oscillations exhibited in some cases prior to reaching a fixed point. The length of oscillations depends on value of our non-dimensionalized damping constant, σ, as well as the initial conditions. Smaller values of σ lead to longer oscillations.

In Figure 4.5, there are two examples of long-time transient oscillations. These appear to be trap-lining behavior. The groups, both positively and negatively informed, oscillate between the two target locations before settling to a

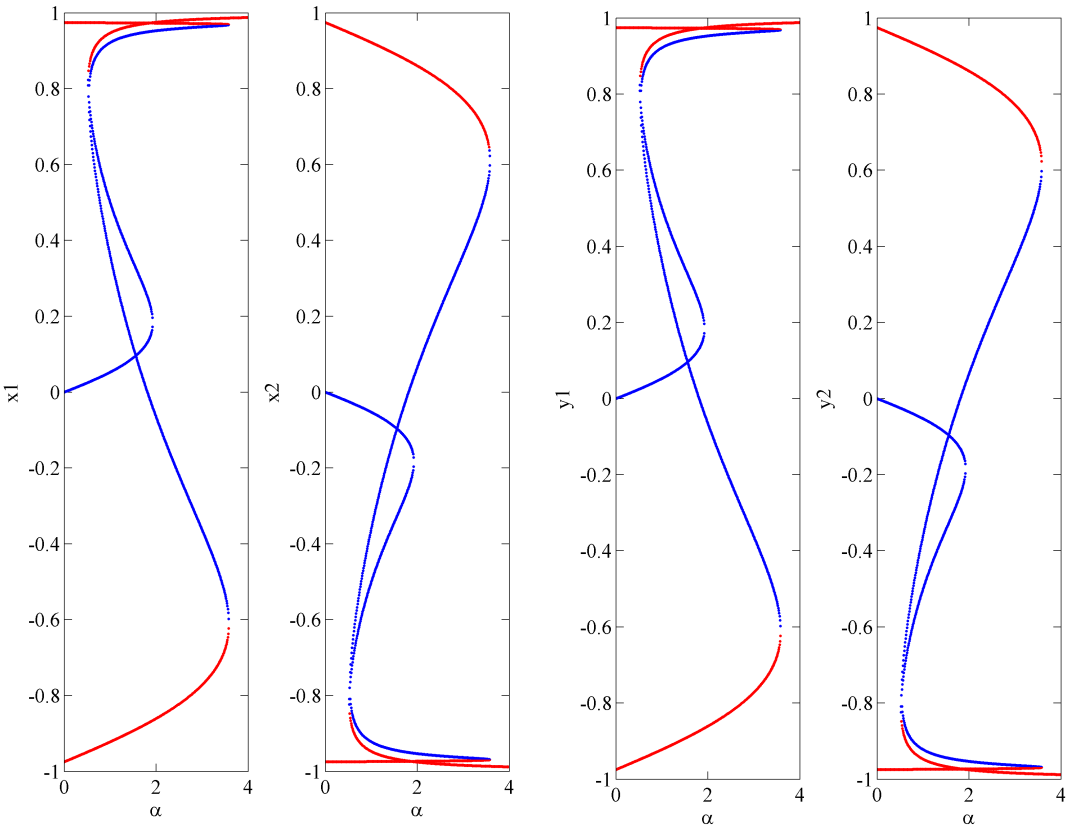

Figure 4.4: Bifurcation Diagram of Model in Two Spatial Dimensions

Bifurcation diagram for long-range decay of attraction (Case B) model in two spatial dimensions. Curves in red denote stable fixed points while curves in blue denote unstable fixed points.

(a) The far left panel shows the bifurcation curves with x_1 as a function of α.

(b) The central left panel shows the bifurcation curves with x_2 as a function of α.

(c) The central right panel shows the bifurcation curves with y_1 as a function of α.

(d) The far right panel shows the bifurcation curves with y_2 as a function of α.

Figure 4.5: Transient Trap-lining Behavior in Two Spatial Dimensions

Trajectories of the two populations in the x-y plane over 100 time intervals. Black x's mark the desired location of each informed population: $(1, 1)$ and $(-1, -1)$. The x-axis is the x-position, the y-axis is the y-position of the groups and σ is 0.01 for both simulations.

(a) Trajectories with initial conditions $x_1 = -0.4618$, $y_1 = -0.1543$, $x_2 = 0.0957$, $y_2 = 0.8855$, $v_{x_1} = v_{y_1} = v_{x_2} = v_{y_2} = 0$ lead after a long time to a consensus decision near $(1, 1)$.

(b) Trajectories with initial conditions $x_1 = -0.8624$, $y_1 = -0.3608$, $x_2 = 0.0617$, $y_2 = 0.3089$, $v_{x_1} = v_{y_1} = v_{x_2} = v_{y_2} = 0$ lead after a long time to a consensus decision near $(1, 1)$.

(a)

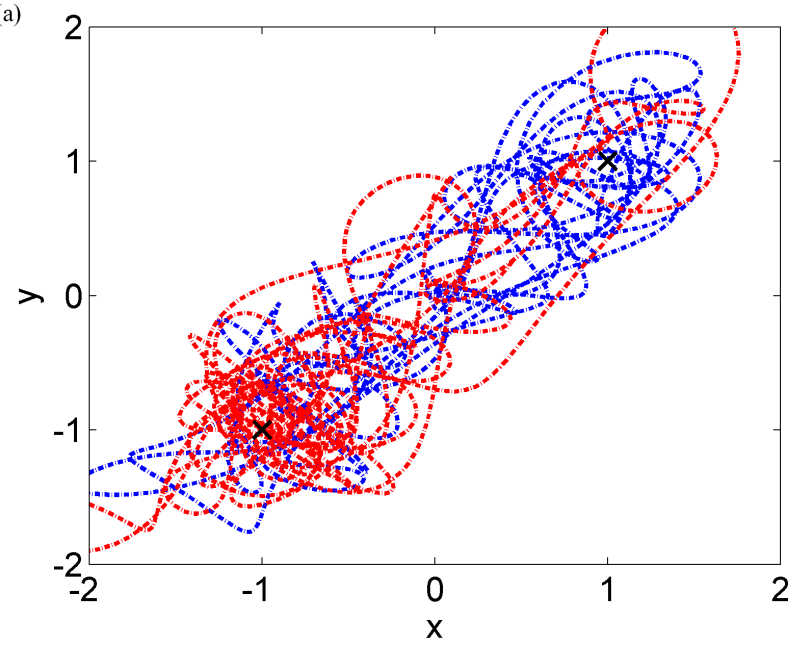

(b)

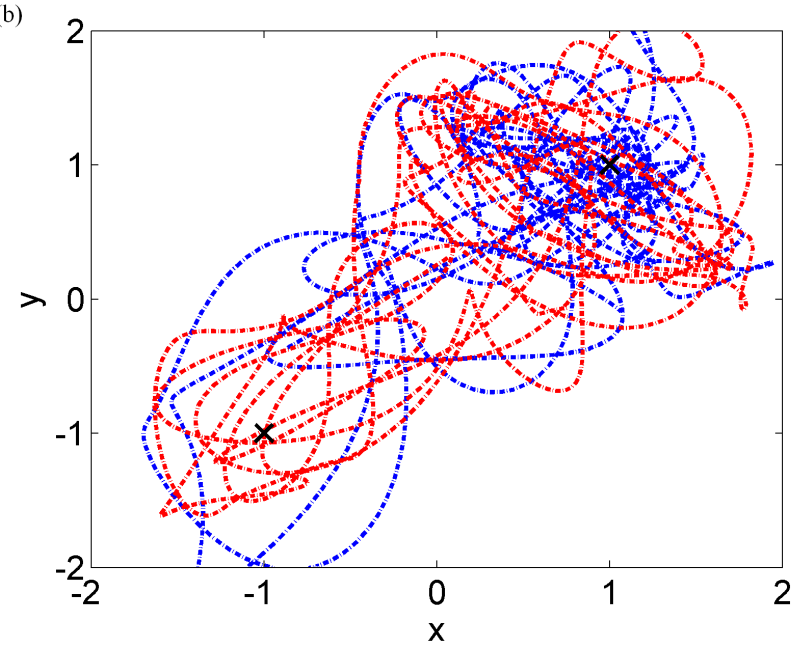

fixed point near one of the preferred locations. In both examples, the motion is restricted to a region near the line between $(1, 1)$ and $(-1, -1)$. As σ is increased the length of oscillations decreases.

4.5 Discussion

In this chapter, we have examined several mass-spring inspired models of groups composed of two equal-sized subgroups with conflicting information. The difference in the models involves the number of spatial dimensions as well as the functional forms governing how long the individual holds onto preferences. In all models we consider α, which governs the relative strength of attraction to the desired location versus the attraction to the group, to be our bifurcation parameter.

We obtain similar results in both one and two spatial dimensions. In both cases the number of stable fixed points depends on the particular functional form as well as the value of alpha. When there is only one fixed point, only averaging is observed. When there is more than one stable fixed point, both averaging and consensus decision making are observed.

The other parameter σ determines how quickly the population settles to its long term behavior. By reducing σ the population oscillates between the desired locations for a short amount of time before settling to either averaging or consensus decision making. This is considered to be transient trap-lining.

4.5.1 Role of forgetfulness

In this paper, we have shown that productive consensus decision making does not occur in globally coupled systems with two groups of equal size without the presence of forgetfulness. This was also observed by Nabet et al. [96].

We find for all models with functional forms that involve forgetfulness, the reduction of attraction to a particular location as one moves away from it, (Case B and Case D) there are multiple stable solutions for a wide range of the bifurcation parameter, α. Some of these stable fixed points equated to averaging and some to productive consensus decision making. When multiple stable points exist, the resultant fixed point reached is dependent upon the initial conditions. At large values of α there is only one fixed point for splitting around the average of zero which is expected since large α means a strong preference for the desired location over the group.

Further, it is not necessary for the animal to forget completely, analogous to a functional form that decays to zero (Case B). As long as there is some reduction from the maximum (Case D), which we term forgetfulness, there is the ability to have some level of consensus decision making. The closer the asymptotic value is to zero, the closer the two populations will be to each other in a consensus decision. Although, as long as the asymptotic value is less than the maximum value, multiple stable fixed points can occur.

For models which do not include forgetfulness there is only a single stable fixed point of averaging. Such Cases A and C do not allow for productive consensus decision making.

4.5.2 Role of naives

Couzin et al. [90] have shown that naive individuals are essential for productive consensus decision making even without forgetfulness. In addition, they have shown that naive individuals help the group make the decision faster and more accurately. Similar results showing the benefit of naive individuals are seen experimentally [95].

In this paper, we do not include naive populations in our models. With global coupling, a naive population merely averages the distance between the informed population, and thus does not contribute to the dynamics. With a naive population exact values of the fixed points would be altered but not the number and stability of the fixed points. Thus naives can not aid productive consensus decision making in this framework. It is our intention to further examine the role of naive individuals which may entail breaking the all-to-all coupling that has been included thus far.

APPENDIX A

MACROPHAGE ACTIVATION EXPERIMENTAL PROCEDURE

Stimulation experiments:

Using the RAW Arginase-1/GFP cell clone D8, a number of stimulation experiments were performed. IL-4 from Cell Sciences (Canton, MA) and cAMP from Sigma-Aldrich (St. Louis, MO) in concentrations of 5ng/mL and 0.5mM respectively were used to induce alternative activation. IFN-γ from Cell Sciences at 100units/mL or CpG ODN 1826 class B with the sequence 5' - TCCATGACGTTCCTGACGTT- 3' from Sigma-Genosys (The Woodlands, TX) at 1μg/mL, which is an immunostimulatory oligonucleotide (23) that activates TLR9, and a combination of CpG and IFN-γ were used to induce classical activation. Stimulations were performed either in 24-well culture plates containing 1mL of medium with 2 million cells per well or in 96-well culture plates containing 200μL of medium with 400,000 cells per well.

Production of RAW cells with a GFP transgene:

Dr. Sidney Morris of the University of Pittsburgh produced a reporter murine macrophage-like RAW cell line (RAW 246.7) for this project by transfecting the cells with a Green Fluorescence Protein (GFP) transgene containing a promotor for Arginase-1 cloned into the vector pZsGreen-1-DR. The vector also contains a neomycin-resistance cassette, which allows the cells to be selected using G418. With this cell line, any time that the Arginase-1 promotor is activated, GFP is also expressed. GFP, when struck by laser light, fluoresces and enables classification via flow cytometry. Once the cell line was received, the cells were stimulated and were sorted into GFP positive and negative cells and

then selected for individual cell clones by limiting dilution. Cells were grown in DMEM high glucose without glutamine from BioWhittaker, Inc (Walkersville, MD) supplemented with 10mL penicillin-streptomycin solution from GIBCO®, 10mL 200mM glutamine from BioWhittaker, Inc. (4mM final), 5mL 1M HEPES from GIBCO ®(15mM final), 5mL sodium pyruvate from GIBCO® and 50mL defined Fetal Calf Serum (FCS) from HyClone (Logan, Utah; 10% final). All amounts are based upon 500 mL of DMEM. Additionally G418 from A.G. Scientific, Inc. (San Diego, CA) at a concentration of 0.5mg/mL was consistently added to the cells to select for those containing the transgene. The cells were incubated at 37°C in a 5% CO_2 and humidified environment.

Cell staining in preparation for flow cytometry analysis:

The stimulated cells were incubated at 37°C for about one day. Supernatants were saved in a 96-well titer plate and kept frozen at -20°C until they were tested for the presence of Nitric Oxide or Urea. Cells were taken up in 1mL of chilled phosphate buffer solution (PBS) from Mediatech, Inc. (Herndon, VA) and were incubated at 4°C for 10 minutes. Cells were then mixed with the PBS and transferred to separate FACS tubes. The tubes were centrifuged at 1200rpm for 5 minutes., supernatants were discarded and 100μL of a 1/200 dilution of PE-labeled anti-CD40 from eBioscience, Inc. (San Diego, CA); final 0.02mg/mL) in FACS buffer consisting of PBS, 5mg/mL Bovine Serum Albumin (BSA) form Fischer Scientific (Pittsburgh, PA) and 10% sodium azide was added to each tube. CD40 is a surface protein, which functions as a co-stimulatory molecule for T- and B-cell activation. This protein is commonly used as a general marker for macrophage activation. Again the tubes were placed in 4°C to incubate for 15 minutes. 1mL of FACS buffer was added to each tube and the tubes were then

placed back in the centrifuge for another 5-minute spin. The supernatants were discarded and the cells were brought up in 300μL of FACS buffer and were analyzed by flow cytometry on a FACS machine, FACSCalibur , from BD (Franklin Lakes, NJ). The FACS machine was used to determine if there was an upregulation of Arginase-1/GFP in the stimulated cells,. Analysis was performed using FlowJo version 4.6.2 and dead cells were excluded from the analysis by staining with 1μL of 10μg/mL stock solution of Propidium Iodide (PI) form Sigma-Aldrich, which invades only the leaky membranes of dead cells.

Analysis of supernatants for the production of Nitric Oxide by the Griess Reaction:

Nitric oxide tests were performed using the supernatants that were removed from the activated cells and were then frozen. 50μL of each sample were plated into a new 96-well titer plate with duplicates of each sample. Two rows were allocated for standards. 75μL of the cell medium went into the first two wells and only 50μL into the remaining. 25μL of a 10mM stock solution of sodium nitrite from Mallinckrodt Baker, Inc. (Paris, KY) was added to the first two wells and a serial dilution was performed down the row, leaving the last two wells alone as blanks; the extra 50μL in the pipet was discarded. An equal amount of 'Solution A' consisting of sulfanilamide from Mallinckrodt Baker, Inc. at 1mg/mL in 2.5% H_3PO_4 and 'Solution B' consisting of naphthylethylenediamine from Sigma-Aldrich at 3μg/mL in 2.5% H_3PO_4 were mixed and 50μL of the mixture was added to each well. The plate was then read on a PowerWave XS Microplate Scanning Spectrophotometer by Bio-Tek® Instruments, Inc. (Winooski, VT) using a protocol measuring the presence of nitric oxide. The results were tabulated in Prism 4.0c by GraphPad Software, Inc. (San Diego, CA).

Analysis of supernatants for production of Urea:

Urea tests were performed using the supernatants that were removed from the activated cells and were then frozen. 50μL of each sample were transferred into 200μL eppendorf tubes. 50μL of 50mM $MnCl_2$-Tris solution - 5 mL of $MnCl_2$ (0.989g $MnCl_2$ in 50mL water) plus 2.5mL 1M Tris plus 42.5mL water - was added to each eppendorf tube. The tubes were heated for 10 minutes in a 55°C water bath. 50*mu*L of each eppendorf tube was transferred to a new 2mL eppendorf tube and placed on ice. 50μL of 0.5M arginine solution (0.871g in 10mL water) was quickly added to each tube. These tubes were incubated at 37°C for 1 hour. Urea standards were set up in 2mL eppendorf tubes. 1M Urea (0.6g Urea in 10mL water) was diluted into 50μL samples from 10mM to 0.078125 mM in serial dilutions. There was 1 50μL blank. 800μL of Stop Solution (10 mL 96% acid H_2SO_4 plus 30 mL 85% acid H_3PO_4 plus 70mL water) was added to each tube. 50μL of 9% ISPF (α-Isonitrosopropiophenone) was added to each tube. Tubes were vortexed for 10 seconds. Holes were punch in the lids. The tubes were heated for 30 minutes at 95°C. Tubes were cooled for 10 minutes on ice. 100μL of each sample were plated into a new 96-well titer plate with duplicates of each sample. Two rows were allocated for standards. 100μL of the standards and blanks went into the standard row. The plate was then read on a PowerWave XS Microplate Scanning Spectrophotometer by Bio-Tek® Instruments, Inc. (Winooski, VT) using a protocol measuring the presence of nitric oxide. The results were tabulated in Prism 4.0c by GraphPad Software, Inc. (San Diego, CA).

BIBLIOGRAPHY

[1] F. Porcheray, S. Viaud, A. C. Rimaniol, C. Leone, B. Samah, N. Dereuddre-Bosquet, D. Dormont, and G. Gras, (2005), Macrophage activation switching: an asset for the resolution of inflammation, Clinical and Experimental Immunology. 142, 481–489.

[2] R. D. Stout, and J. Suttles, (2004), Functional plasticity of macrophages: reversible adaptation to changing microenvironments, Journal of Leukocyte Biology. 76, 509–513.

[3] J. L. Reyes, and L. I. Terrazas, (2007), The divergent roles of alternatively activated macrophages in helminthic infections, Parasite Immunology. 29, 609–619.

[4] R. A. Goldsby, T. J. Kindt, and B. A. Osborne (2002) Kuby Immunology 4th ed, W. H. Freeman and Company, New York.

[5] C. A. Janeway, P. Travers, M. Walport, and M. Shlomichik (2001) Immunobiology 5, Garland Publishing, New York.

[6] W. C. Gause, J. F. Urban, Jr., and M. J. Stadecker, (2003), The immune response to parasitic helminths: insights from murine models, Trends in Immunology. 24, 269–277.

[7] R. M. Anthony, L. I. Rutitzky, J. F. Urban, Jr., M. J. Stadecker, and W. C. Gause, (2007), Protective immune mechanisms in helminth infection, Nature Reviews Immunology. 7, 975–987.

[8] M. Loehning, A. N. Hegazy, D. D. Pinschewer, D. Busse, K. S. Lang, T. Hofer, A. Radbruch, R. M. Sinkernagel, and H. Hengartner, (2008), Long-lived virus-reactive memory T cells generated from purified cytokine-secreting T helper type 1 and type 2 effectors, Journal of Experimental Medicine. 205(1), 53-61.

[9] C. N. Serhan, R. Yang, K. Martinod, K. Kasuga, P. S. Pillai, T. F. Porter, S. F. Oh and M. Spite, (2009), Maresins: novel macrophage mediators with potent anti-inflammatory and proresolving actions, Journal of Experimental Medicine. 206 (1), 15-23.

[10] S. Gordon, (2007), The macrophage: past, present and future, European Journal of Immunology. 37(1), S9-17.

[11] E. J. Pearce, and A. S. MacDonald, (2002), The immunobiology of schistosomiasis, Nature Reviews Immunology. 2(7), 499-511.

[12] M. Hesse, M. Modolell, A. C. La Flamme, M Schito, J. M. Fuentes, A. W. Cheever, E. J. Pearce, and T. A. Wynn, (2001), Differential regulation of nitric oxide synthase-2 and arginase-1 by type1/type2 cytokines in vivo: granulomatous pathology is shaped by the pattern of L-arginine metabolism, Journal of Immunology. 167, 6533–6544.

[13] P. G. Fallon, and N. E. Mangan, (2007), Suppression of TH2-type allergic reactions by helminth infection, Nature Review Immunology. 7, 220–230.

[14] D. R. Herbert, C. Holscher, M. Mohrs, B. Arendse, A. Schwegmann, M. Radwanska, M. Leeto, R. Kirsch, P. Hall, H. Mossmann, B. Claussen, I. Forster, and F. Brombacher, (2004), Alternative macrophage activation is essential for survival during schistosomiasis and down modulates T helper 1 responses and immunopathology, Immunity. 20, 623–635.

[15] S. Gordon, (2003), Alternative activation of macrophages, Nature Reviews Immunology. 3, 23–35.

[16] M. Modolell, I. M. Corraliza, F. Link , G. Soler, and K. Eichmann, (1995), Reciprocal regulation of the nitric oxide synthase/arginase balance in mouse bone marrow-derived macrophages by TH1 and TH2 cytokines, European Journal of Immunology. 25(4), 1101-1104.

[17] J. MacMicking, Q. W. Xie, and C. Nathan, (1997), Nitric oxide and macrophage function, Annual Review of Immunology. 15, 323-50.

[18] C. Nathan, (1994), Nitric oxide and biopterin: a study in Chairoscuro, Journal of Clinical Investigation. 93(5), 2236-43.

[19] D. M. Mosser, (2003), The many faces of macrophage activation, Journal of Leukocyte Biology. 73, 209–212.

[20] R. D. Schreiber, (1984), Identification of gamma-interferon as a murine macrophage-activating factor for tumor cytotoxicity, Contemporary Topics in Immunobiology. 13, 171–198.

[21] M. J. Stadecker, H. Asahi, E. Finger, H. J. Hernandez, L. I. Rutitzky, and J. Sun, (2004), The immunobiology of Th1 polarization in high-pathology schistosomiasis, Immunological Reviews. 201, 168–179.

[22] S. El-Gayar, H. Thuring-Nahler, J. Pfeilschifter, M. Rollinghoff, and C. Bogdan, (2003), Translational control of inducible nitric oxide synthase by IL-13 and arginine availability in inflammatory macrophages, Journal of Immunology. 171(9), 4561-8.

[23] A. Classen, J. Lloberas, and A. Celada, (2009), Macrophage activation: classical versus alternative, Methods in Molecular Biology. 531, 29-43.

[24] M. Hecker, H. Nematollahi, C. Hey, R. Busse, and K. Racké, (1995), Inhibition of arginase by N^G-hydroxy-L-arginine in alveolar macrophages: implications for the utilization of L-arginine for nitric oxide synthesis, FEBS Letters. 359, 251–254.

[25] C. F. Anderson, and D. M. Mosser, (2002), A novel phenotype for an activated macrophage: the type 2 activated macrophage, Journal of Leukocyte Biology. 72, 101–106.

[26] T. Kreider, R. M. Anthony, J. F. Urban, Jr., and W. C. Gause, (2007), Alternatively activated macrophages in helminth infections, Current Opinions in Immunology. 19, 448-453.

[27] C. Moali, J-L. Boucher, M-A. Sari, D. J. Stuehr, and D. Mansuy, (1998), Substrate Specificity of NO Synthases: Detailed Comparison of L-Arginine, Homo-L-Arginine, Their N^{ω}-Hydroxy Derivatives, and N^{ω}-Hydroxynor-L-arginine, Biochemistry. 37, 10453–10460.

[28] S. Gordon, I. Fraser, D. Nath, D. Hughes, and S. Clarke, (1992), Macrophages in tissues and in vitro, Current Opinions in Immunology. 4, 25–32.

[29] F. O. Martinez, A. Sica, A. Mantovani, and M. Locati, (2008), Macrophage activation and polarization, Frontiers in Bioscience. 13, 453-61.

[30] J. Pesce, M. Kaviratne, T. R. Ramalingam, R. W. Thompson, J. F. Urban, Jr., A. W. Cheever, D. A. Young, M. Collins, M. J. Grusby, and T. A. Wynn, (2006), The IL-21 receptor augments Th2 effector function and alternative macrophage activation, Journal of Clinical Investigation. 116(7), 2044-55.

[31] J-L. Boucher, J. Custot, S. Vadon, M. Delaforge, M. Lepoivre, J-P. Tenu, A. Yapo, and D. Mansuy, (1994), N^{ω}-hydroxy-L-arginine, an intermediate in the L-arginine to Nitric Oxide pathway, is a strong inhibitor of liver and macrophage Arginase, Biochemical and Biophysical Research Communities. 203, 1614–1621.

[32] F. Daghigh, J. M. Fukuto, and D. E. Ash, (1994), Inhibition of rat liver Arginase by an intermediate in NO biosynthesis, N^G-hydroxy-L-arginine: implications for the regulation of nitric oxide biosynthesis by arginase, Biochemical and Biophysical Research Communities. 202, 174–180.

[33] C. Moali, M. Brollo, J. Custot, M. Sari, J-L. Boucher, D. J. Stuehr, and D. Mansuy, (2000), Recognition of α-Amino Acids Bearing Various C=NOH Functions by Nitric Oxide Synthase Involves Very Different Structural Determinants, Biochemistry. 39, 8208–8218.

[34] J. L. Boucher, C. Moali, and J. P. Tenu, (1999), Nitric oxide biosynthesis, nitric oxide synthase inhibitors and arginase competition for L-arginine utilization, Cellular and Molecular Life Sciences. 55, 1015–1028.

[35] J. Sethna (2004, September 11) *The Sloppy Cell*. Retrieved January 11, 2005, from http://www.lassp.cornell.edu/sethna/GeneDynamics/.

[36] A. M. Krieg, (2000), Signal transduction induced by immunostimulatory CpG DNA, Springer Seminars in Immunopathology. 22(1-2), 97-105.

[37] R. Rutschman, R. Lang, M. Hesse, J. N. Ihle, T. A. Wynn, and P. J. Murray, (2001), Cutting Edge: Stat6-Dependent Substrate Depletion Regulates Nitric Oxide Production, Journal of Immunology. 166 (4), 2173–2177.

[38] T. Gotoh, and M. Mori, (1999), Arginase-1 II downregulates nitric oxide (NO) production and prevents NO-mediated apoptosis in murine macrophage-derived RAW 264.7 cells, Journal of Cellular Biology. 144, 427–434.

[39] D. M. Mosser and J. P. Edwards, (2008), Exploring the full spectrum of macrophage activation, Nature Reviews Immunology. 8(12), 958–969.

[40] J. Khallou-Laschet, A. Varthaman, G. Fornasa, C. Compain, A.-T. Gaston, M. Clement, M. Cussiot, O. Levillain, S. Graff-Dubois, A. Nicoletti, and G. Caligiuri, (2010), Macrophage plasticity in experimental Atherosclerosis, PLoS ONE. 5(1), e8852.

[41] Y. Kuramoto (1975) in H. Araki (Ed.) International Symposium on Mathematical Problems in Theoretical Physics, Lecture Notes in Physics Volume 39, Springer, New York, pp. 420–422.

[42] Y. Kuramoto (1984) Chemical Oscillations, Waves and Turbulence, Springer, Berlin.

[43] S. H. Strogatz, (2000), From Kuramoto to Crawford: exploring the onset of synchronization in populations of coupled oscillators, Physica D. 143, 1–20.

[44] J. A. Acebron, L. L. Bonilla, C. J. Perez Vicente, F. Ritort, R. Spigler, (2005), The Kuramoto model: a simple paradigm for synchronization phenomena, Reviews of Modern Physics. 77, 137–185.

[45] A. Pikovsky, M. Rosenblum, and J. Kurths (2001) Synchronization: A Universal Concept in Nonlinear Science, Cambridge University Press, Cambridge.

[46] S. Strogatz (2003) Sync, Hyperion, New York.

[47] I. Z. Kiss, Y. Zhai, J. L. Hudson, (2002), Emerging coherence in a population of chemical oscillators, Science. 296, 1676–1678.

[48] I. Z. Kiss, Y. Zhai, J. L. Hudson, (2008), Resonance clustering in globally coupled electrochemical oscillators with external forcing, Physical Review E. 77, 046204.

[49] K. Wiesenfeld, P. Colet, and S. H. Strogatz, (1996), Synchronization transitions in a disordered Josephson series array, Physical Review Letters. 76, 404–407.

[50] J. Pantaleone, (2002), Synchronization of metronomes, American Journal of Physics. 70, 992–1000.

[51] C. von Cube, S. Slama, D. Kruse, C. Zimmermann, Ph. W. Courteille, G. R. M. Robb, N. Piovella, and R. Bonifacio, (2004), Self-synchronization and dissipation-induced threshold in collective atomic recoil lasing, Physical Review Letters. 93, 083601.

[52] J. Pantaleone, (1998), Stability of incoherence in an isotropic gas of oscillating neutrinos, Physical Review D. 58, 073002.

[53] M. C. Moore-Ede, F. M. Sulzman, and C. A. Fuller (1982) The Clocks That Time Us, Harvard University Press, Cambridge.

[54] J. C. Dunlap, J. J. Loros, and P. J. Decoursey (2003) Chronobiology: Biological Timekeeping, Sinauer Associates, Sunderland, MA.

[55] R. G. Foster and L. Kreitzman (2005) Rhythms of Life: The Biological Clocks that Control the Daily Lives of Every Living Thing, Yale University Press, New Haven.

[56] D.K. Welsh, D.E. Logothetis, M. Meister, and S.M. Reppert, (1995), Individual neurons dissociated from rat suprachiasmatic nucleus express independently phased firing rhythms, Neuron. 14, 697–706.

[57] C. Liu, D. R. Weaver, S. H. Strogatz, and S. M. Reppert, (1997), Cellular construction of a circadian clock: Period determination in the suprachiasmatic nuclei. Cell. 91, 855–860.

[58] J. C. Dunlap, (1993), Genetic analysis of circadian clocks, Annual Review of Physiology. 55, 683–728.

[59] J. S. Takahashi, (1995,) Molecular neurobiology and genetics of circadian rhythms in mammals, Annual Review of Neuroscience. 18, 531–553.

[60] H. Sakaguchi, (1988), Cooperative phenomena in coupled oscillator systems under external fields, Progress of Theoretical Physics. 79, 39.

[61] T. M. Antonsen, R. T. Faghih, M. Girvan, E. Ott, and J. Platig, (2008), External periodic driving of large systems of globally coupled phase oscillators, Chaos. 18, 037112.

[62] E. Ott and T. M. Antonsen, (2008), Low dimensional behavior of large systems of globally coupled oscillators, Chaos. 18, 037113.

[63] J. Guckenheimer, (1986), Multiple bifurcation problems for chemical reactors, Physica D. 20, 1–20.

[64] E. M. Izhikevich, (2000), Neural excitability, spiking and bursting, International Journal of Bifurcation and Chaos. 10, 1171–1266.

[65] R. Adler, (1946), A study of locking phenomena in oscillators, Proceedings of the I.R.E. 34, 351–357.

[66] A. E. Siegman (1986) Lasers, University Science Books, Mill Valley, CA.

[67] M. K. S. Yeung and S. H. Strogatz, (1998), Nonlinear dynamics of a solid-state laser with injection, Physical Review E. 58, 4421–4434.

[68] G. B. Ermentrout and J. Rinzel, (1984), Beyond a pacemaker's entrainment limit: phase walk-through, American Journal of Physiology. 246, R102–R106.

[69] J. Guckenheimer and P. Holmes (1983) Nonlinear Oscillations, Dynamical Systems and Bifurcation of Vector Fields, Springer, New York.

[70] E. A. Martens, E. Barreto, S. H. Strogatz, E. Ott, P. So, and T. M. Antonsen, (2008), Exact results for the Kuramoto model with a bimodal frequency distribution, ArXiv: 0809:2129.

[71] H. Daido, (1994), Generic scaling at the onset of macroscopic mutual entrainment in limit-cycle oscillators with uniform all-to-all coupling, Physical Review Letters. 73, 760–763.

[72] J. D. Crawford, (1995), Scaling and singularities in the entrainment of globally coupled oscillators, Physical Review Letters. 74, 4341–4344.

[73] R. Beckers, J. L. Deneubourg, and S. Goss, (1992), Trails and U-turns in the selection of a path by the ant LasiusNiger, Journal of Theoretical Biology. 159, 397-415.

[74] R. Beckers, J. L. Deneubourg, and S. Goss, (1993), Modulation of trail laying in the ant LasiusNiger (hymenoptera, formicidae) and its role in the collective selection of a food source, Journal of Insect Behavior. 6, 751-759.

[75] D. J. T. Sumpter, (2006), The principles of collective animal behaviour. Philosophical Transactions of the Royal Society of London Series B-Biological Sciences. 361, 5–22.

[76] J. K. Parrish and L. Edelstein-Keshet, (1999), Complexity, pattern, and evolutionary trade-offs in animal aggregation, Science. 284, 99-101.

[77] B. L. J. Partridge, (1982), The structure and function of fish schools, Scientific American. 246.

[78] D. J. Hoare, I. D. Couzin, J. G. J. Godin and J. Krause, (2004), Context-dependent group size choice in fish, Animal Behavior. 67, 155-164.

[79] C. M. Topaz, A. L. Bertozzi, and M. A. Lewis, (2006), A nonlocal continuum model for biological aggregation, Bulletin of Mathematical Biology. 68, 1601-1623.

[80] A. Mogilner and L. Edelstein-Keshet, (1999), A non-local model for a swarm, Journal of Mathematical Biology. 38, 534-570.

[81] A. Mogilner, L. Edelstein-Keshet, L. Bent, and A. Spiros, (2003), Mutual interactions, potentials, and individual distance in a social aggregation, Journal of Mathematical Biology. 47, 353-389.

[82] A. J. Leverentz, C. M. Topaz and A. J. Bernoff, (2009), Asymptotic Dynamics of Attractive-Repulsive Swarms, SIAM Journal of Applied Dynamical Systems. 8(3), 880–908.

[83] I. D. Couzin and J. Krause, (2003), Self-organization and collective behavior of vertebrate, Advances in the Study of Behavior. 32, 1-75.

[84] I. D. Couzin, (2009), Collective cognition in animal groups, Trends in Cognitive Sciences. 13(1), 36-43.

[85] T. Deisboeck and I. D. Couzin, (2009), Collective behavior in cancer cell populations. BioEssays. 31(2), 190-197.

[86] A. Czirok and T. Vicsek, (2000) Collective behavior of interacting self-propelled particles, Physica A. 281, 17-29.

[87] J. K. Parrish, S. V. Viscido, and D. Grunbaum, (2002), Self organized fish schools: An examination of emergent properties, Biology Bulletin. 202, 296-305.

[88] C. W. Reynolds, (1987), Flocks, herds and schools: a distributed behavioural model, Computer Graphics. 21, 25-33.

[89] S. J. Moon, B. Nabet, N. E. Leonard, S. A. Levin, and I. G. Kevrekidis, (2007), Heterogeneous animal group models and their group-level alignment dynamics: An equation-free approach, Journal of Theoretical Biology. 246, 100-112.

[90] I. D. Couzin, J. Krause, N. R. Franks, and S. A. Levin, (2005) Effective leadership and decision making in animal groups on the move, Nature. 433,513-516.

[91] I. D. Couzin, J. Krause, R. James, G. D. Ruxton, and N. R. Franks, (2002), Collective memory and spatial sorting in animal groups, Journal of Theoretical Biology. 218, 111.

[92] H. Li, A. Kolpas, L. Petzold, and J. Moehlis, (2009), Parallel simulation of a fish schooling model on a general-purpose graphics processing unit, Concurrency and Computation. 21, 725-737.

[93] D. J. T. Sumpter, J. Krause, R. James, I. D. Couzin, and A. Ward, (2008), Consensus decision-making by fish, Current Biology. 18, 1773-1777.

[94] A. J. Ward, D. J. T. Sumpter, I. D. Couzin, P. J. B. Hart, and J. Krause, (2008), Quorum decision making facilitates information transfer in fish shoals, Proceedings of the National Academy of Science. 105, 6948-6953.

[95] I. D. Couzin, (2009), Personal communication.

[96] B. Nabet, N. E. Leonard, I. D. Couzin, and S. A. Levin, (2009), Dynamics of decision-making in animal group motion, Journal of Nonlinear Science. DOI 10.1007/s00332-008-9038-6.

[97] M. di Bernardo, C. J. Budd, A. R. Champneys and P. Kowalczyk (2009) Piecewise-smooth Dynamical Systems, Springer, New York.